PACIFIC EARTHQUAKE ENGINEERING
RESEARCH CENTER

Hyperbolic Hydro-mechanical Model for Seismic Compression Prediction of Unsaturated Soils in the Funicular Regime

Dellena Kinikles
John S. McCartney

Department of Structural Engineering
University of California, San Diego

PEER Report No. 2022/05

Pacific Earthquake Engineering Research Center
Headquarters at the University of California, Berkeley
December 2022

PEER 2022/05
December 2022

Disclaimer

The opinions, findings, and conclusions or recommendations expressed in this publication are those of the author(s) and do not necessarily reflect the views of the study sponsor(s), the Pacific Earthquake Engineering Research Center, or the Regents of the University of California.

Hyperbolic Hydro-mechanical Model for Seismic Compression Prediction of Unsaturated Soils in the Funicular Regime

Dellena Kinikles, M.S.

John S. McCartney, Ph.D., P.E., F.ASCE

Department of Structural Engineering
University of California San Diego, La Jolla, California

PEER Report 2022/05

Pacific Earthquake Engineering Research Center
Headquarters at the University of California,
Berkeley, December 2022

ABSTRACT

A semi-empirical elasto-plastic constitutive model with a hyperbolic stress-strain curve was developed with the goal of predicting the seismic compression of unsaturated sands in the funicular regime of the soil-water retention curve (SWRC) during undrained cyclic shearing. Using a flow rule derived from energy considerations, the evolution in plastic volumetric strain (seismic compression) was predicted from the plastic shear strains of the hysteretic hyperbolic stress-strain curve. The plastic volumetric strains are used to predict the changes in degree of saturation from phase relationships and changes in pore air pressure from Boyle's and Henry's laws. The degree of saturation was used to estimate changes in matric suction from the transient scanning paths of the SWRC. Changes in small-strain shear modulus estimated from changes in mean effective stress computed from the constant total stress and changes in pore air pressure, degree of saturation and matric suction, in turn affect the hyperbolic stress-strain curve's shape and the evolution in plastic volumetric strain. The model was calibrated using experimental shear stress-strain backbone curves from drained cyclic simple shear tests and transient SWRC scanning path measurements from undrained cyclic simple shear tests. Then the model predictions were validated using experimental data from undrained cyclic simple shear tests on unsaturated sand specimens with different initial degrees of saturation in the funicular regime. While the model captured the coupled evolution in hydro-mechanical variables (pore air pressure, pore water pressure, matric suction, degree of saturation, volumetric strain, effective stress, shear modulus) well over the first 15 cycles of shearing, the predictions were less accurate after continued cyclic shearing up to 200 cycles. After large numbers of cycles of undrained shearing, a linear decreasing trend between seismic compression and initial degree of saturation was predicted from the model while a nonlinear increasing-decreasing trend was observed in the cyclic simple shear experiments. This discrepancy may be due to not considering post shearing reconsolidation in the model, calibration of model parameters, or experimental issues including a drift in the position of the hysteretic shear-stress strain curve. Nonetheless, the trend from the model is consistent with predictions from previously-developed empirical models in the funicular regime of the SWRC. The developments of the new mechanistic model developed in this study will play a key role in the future development of a holistic model for predicting the seismic compression across all regimes of the SWRC.

Keywords: Seismic Compression; Unsaturated Soils; Coupled Processes, Cyclic Simple Shear; Constitutive Modeling

ACKNOWLEDGMENTS AND DISCLAIMER

This research study was funded by the Pacific Earthquake Engineering Research (PEER) Center, under Contract No. 1169-NCT-JSM The opinions, findings, conclusions, and recommendations expressed in this publication are those of the authors and do not necessarily reflect the view of Pacific Earthquake Engineering Research (PEER) Center or the Regents of the University of California.

CONTENTS

ABSTRACT ..... **IV**

ACKNOWLEDGMENTS AND DISCLAIMER ..... **VI**

CONTENTS ..... **VIII**

LIST OF TABLES ..... **XI**

LIST OF FIGURES ..... **XIII**

1 INTRODUCTION **1**

1.1 Seismic Compression of Unsaturated Soils **1**

1.2 Research Objectives **2**

1.3 Research Approach **3**

1.4 Report Organization **3**

2 BACKGROUND AND LITERATURE REVIEW **5**

2.1 Unsaturated Soils **5**

2.2 Effective Stress in Unsaturated Soils **6**

2.3 Cyclic Response of Soils **9**

2.4 Seismic Compression of Unsaturated Soils in Literature **11**

3 SEISMIC COMPRESSION MODEL FOR THE FUNICULAR REGIME **19**

3.1 Definition of Stresses and Strains during Cyclic Simple Shear Testing **19**

3.2 Prediction of Volumetric Strain during Cyclic Shearing **21**

3.3 Estimation of Changes in Pore Air Pressure During Undrained Shearing **23**

3.4 Changes in Degree of Saturation during Undrained Shearing **24**

3.5 Estimation of Changes in Pore Water Pressure During Undrained Shearing **24**

3.6 Calculation of Effective Stress Changes during Cyclic Shearing **25**

3.7 Predicting the Evolution in Hydro-Mechanical Variables during Undrained Shearing **26**

4 DATA **31**

4.1 Sand Specimens in Cyclic Simple Shear Database 31
4.2 Drained Monotonic Simple Shear Data 32
4.3 Undrained Cyclic Simple Shear Data 32

5 MODEL CALIBRATION 49
5.1 Calibration of Backbone Curve from Drained Shearing of Unsaturated Sand 49
5.2 Calibration of Pore Water Pressure Generation Model 50

6 ANALYSIS 59
6.1 Evolution in Hydro-Mechanical Variables during Undrained Cyclic Shearing 59
6.2 Evaluation of the Effects of Initial Degree of Saturation on Seismic Compression 59
6.3 Evaluation of Reasons behind Discrepancy between Model and Experiments 61
6.3.1 Pore Air Pressure Generation 61
6.3.2 Pore Water Pressure Generation 62
6.4 Implementation of the New Constitutive Model into Site-Specific Seismic Response Analyses 63

7 CONCLUSIONS AND FUTURE RESEARCH NEEDS 71

REFERENCES 73

APPENDIX A 81
A.1 Hyperbolic fitting for cyclic shearing 81
A.2 Volume Compression Equations 82
A.3 Pore Air Pressure Derivation 83
A.4 Relationship between Degree of Saturation and Volumetric Strain 89
A.5 Transient Scanning Curve Equation 90
A.6 Additional Comparisons between Experimental Results and Model Predictions 91

LIST OF TABLES

TABLE 4.1 SUMMARY OF INITIAL TESTING CONDITIONS AND FINAL SHEAR STRAIN FOR DRAINED TESTS.....33

TABLE 4.2 SUMMARY OF INITIAL TESTING CONDITIONS AND FINAL SHEAR STRAIN FOR THE UNDRAINED CYCLIC SIMPLE SHEAR EXPERIMENTS (AFTER RONG AND MCCARTNEY 2020B WITH NEW DATA). 33

TABLE 4.3 SUMMARY OF INITIAL CONDITIONS OF UNDRAINED CYCLIC SIMPLE SHEAR EXPERIMENTS OF RONG AND MCCARTNEY (2020) THAT WERE MODELED IN THIS STUDY.....33

TABLE 5.1 CALIBRATED HYPERBOLIC MODEL PARAMETERS FOR DRAINED TESTS AT A CONSTANT SUCTION OF 4 KPA PERFORMED TO 1% AND 3% SHEAR STRAIN.....53

TABLE 5.2 AVERAGED TRANSIENT SWRC SLOPES OVER ENTIRE 200 CYCLES FROM UNDRAINED CYCLIC SIMPLE SHEAR TESTS (DATA SET 01) FOR INITIAL DEGREES OF SATURATION IN THE FUNICULAR REGIME. 53

TABLE 5.3 PREDICTED TRANSIENT SWRC SLOPES FROM THE EMPIRICAL EQUATION FOR INITIAL DEGREES OF SATURATION IN THE FUNICULAR REGIME. 53

LIST OF FIGURES

FIGURE 2.1 TYPICAL NEAR-SURFACE UNSATURATED SOIL PROFILE WITH HYDROSTATIC CONDITIONS. 14

FIGURE 2.2 TYPICAL SHAPE OF THE SOIL-WATER RETENTION CURVE (SWRC) PARTITIONED INTO THE CAPILLARY, FUNICULAR AND PENDULAR REGIMES DEFINED BY LU AND LIKOS (2004). 14

FIGURE 2.3 SCHEMATIC OF A HYSTERETIC SWRC SHOWING TYPICAL SHAPES OF THE PRIMARY DRYING AND WETTING PATHS IN BLUE AND ORANGE, RESPECTIVELY. 15

FIGURE 2.4 SSCCS REPRESENTATIVE OF SANDS AND CLAYS. 15

FIGURE 2.5 SCHEMATIC EXAMPLE OF A HYPERBOLIC SHEAR STRESS-SHEAR STRAIN CURVE WITH A DEFINITION OF THE SMALL STRAIN SHEAR MODULUS G_I. 16

FIGURE 2.6 SCHEMATIC EXAMPLE OF A SHEAR MODULUS REDUCTION CURVE. 16

FIGURE 2.7 SCHEMATIC EXAMPLE OF SHEAR STRESS-STRAIN HYSTERESIS OF SOILS DURING LOADING, UNLOADING AND RELOADING. 16

FIGURE 2.8 TRENDS IN SEISMIC COMPRESSION MEASUREMENTS FROM UNSATURATED SANDS REPORTED IN THE LITERATURE ALONG WITH TRENDS EXPECTED FROM THE EMPIRICAL MODEL OF GHAYOOMI ET AL. (2013) AND THE TRENDLINE FROM RONG AND MCCARTNEY (2020B). 17

FIGURE 3.1 KEY VARIABLES IN A CYCLIC SIMPLE SHEAR TEST ON A SOIL SPECIMEN AFTER VERTICAL LOADING AND DURING BI-DIRECTIONAL CYCLIC SIMPLE SHEARING. 27

FIGURE 3.2 SCHEMATIC OF THE CHANGES IN STRESS STATE DURING CYCLIC SIMPLE SHEAR TESTING OF A SOIL SPECIMEN SHOWING THE DIRECTIONS OF THE STRESSES DURING APPLIED SHEAR STRAIN TESTING. 27

FIGURE 3.3 BACKBONE CURVE SHAPE FROM THE HYPERBOLIC MODEL: (A) SHEAR STRESS-STRAIN CURVE; (B) SHEAR STRESS RATIO-SHEAR STRAIN CURVE. 28

FIGURE 3.4 HYSTERETIC LOOP SHOWING THE HYPERBOLIC SHEAR STRESS STRAIN REVERSALS ALONG WITH THE HYPERBOLIC BACKBONE CURVE. 28

FIGURE 3.5 SCHEMATIC OF SOIL PARTICLE REARRANGEMENT BEFORE AND AFTER CYCLIC SHEARING SHOWING INITIAL AND FINAL HEIGHTS OF SPECIMEN AND CHANGES IN DEGREE OF SATURATION. 28

FIGURE 3.6 SCHEMATIC OF THE HYPERBOLIC STRESS-STRAIN RELATIONSHIP USED IN UBCSAND 29

FIGURE 3.7 HYSTERETIC SHEAR STRESS-SHEAR STRAIN SHOWING PLASTIC LOAD/RELOAD AND ELASTIC UNLOAD, WITH THE CORRESPONDING PLASTIC/ELASTIC CYCLIC SHEAR STRAIN AND CUMULATIVE PLASTIC VOLUMETRIC STRAIN. 29

FIGURE 3.8 SCHEMATIC OF THE TRANSIENT SCANNING PATH OF THE SWRC FOR A SAND SPECIMEN INITIALLY ON THE PRIMARY DRYING PATH. 29

FIGURE 3.9 FLOW CHART FOR THE SEMI-EMPIRICAL HYPERBOLIC MODEL WITH HYDRO-MECHANICAL COUPLING FOR SEISMIC COMPRESSION IN THE FUNICULAR REGIME. 30

FIGURE 4.1 PARTICLE SIZE DISTRIBUTION CURVE FOR THE SW SAND. 34

FIGURE 4.2 WETTING AND DRYING PATH SWRCS FOR THE SAND SPECIMEN AT D_R = 0.45 WITH TRANSIENT SCANNING PATHS 34

FIGURE 4.3 SCHEMATIC VIEW OF THE SPECIMEN HOUSING IN THE MODIFIED CYCLIC SIMPLE SHEAR DEVICE USED FOR DRAINED AND UNDRAINED EXPERIMENTS ON UNSATURATED SOILS (DIMENSIONS IN MM). 35

FIGURE 4.4 BACKBONE CURVES FOR DRAINED SAND (D_R = 0.45) AT VARIOUS CONSTANT SUCTIONS (4 KPA, 6 KPA, 10 KPA) AND DIFFERENT SHEAR STRAIN AMPLITUDES (1%, 3%). 35

FIGURE 4.5 DATA SET 1 S_0=0.56: (A) SHEAR STRAIN TIME SERIES; (B) SHEAR STRESS TIME SERIES (C) DEGREE OF SATURATION TIME SERIES; (D) VOLUME CHANGE TIME SERIES; (E) PORE AIR PRESSURE CHANGE TIME SERIES; (F) PORE WATER PRESSURE CHANGE TIME SERIES; (G) MATRIC SUCTION CHANGE TIME SERIES; (H) MEAN EFFECTIVE STRESS CHANGE TIME SERIES; (I) CYCLIC SHEAR STRESS AND CYCLIC SHEAR STRAIN LOOPS. 36

FIGURE 4.6 DATA SET 2 S_0=0.56: (A) SHEAR STRAIN TIME SERIES; (B) SHEAR STRESS TIME SERIES (C) DEGREE OF SATURATION TIME SERIES; (D) VOLUME CHANGE TIME SERIES; (E) PORE AIR PRESSURE CHANGE TIME SERIES; (F) PORE WATER PRESSURE CHANGE TIME SERIES; (G) MATRIC SUCTION CHANGE TIME SERIES; (H) MEAN EFFECTIVE STRESS CHANGE TIME SERIES; (I) CYCLIC SHEAR STRESS AND CYCLIC SHEAR STRAIN LOOPS. 37

FIGURE 4.7 DATA SET 1 S_0=0.4: (A) SHEAR STRAIN TIME SERIES; (B) SHEAR STRESS TIME SERIES (C) DEGREE OF SATURATION TIME SERIES; (D) VOLUME CHANGE TIME SERIES; (E) PORE AIR PRESSURE CHANGE TIME SERIES; (F) PORE WATER PRESSURE CHANGE TIME SERIES; (G) MATRIC SUCTION CHANGE TIME SERIES; (H) MEAN EFFECTIVE STRESS CHANGE TIME SERIES; (I) CYCLIC SHEAR STRESS AND CYCLIC SHEAR STRAIN LOOPS. 38

FIGURE 4.8 DATA SET 2 S_0=0.4: (A) SHEAR STRAIN TIME SERIES; (B) SHEAR STRESS TIME SERIES (C) DEGREE OF SATURATION TIME SERIES; (D) VOLUME CHANGE TIME SERIES; (E) PORE AIR PRESSURE CHANGE TIME SERIES; (F) PORE WATER PRESSURE CHANGE TIME SERIES; (G) MATRIC SUCTION CHANGE TIME SERIES; (H) MEAN EFFECTIVE STRESS CHANGE TIME SERIES; (I) CYCLIC SHEAR STRESS AND CYCLIC SHEAR STRAIN LOOPS. 39

FIGURE 4.9 DATA SET 1 S_0=0.3: (A) SHEAR STRAIN TIME SERIES; (B) SHEAR STRESS TIME SERIES (C) DEGREE OF SATURATION TIME SERIES; (D) VOLUME CHANGE TIME SERIES; (E) PORE AIR PRESSURE CHANGE TIME SERIES; (F) PORE WATER PRESSURE CHANGE TIME SERIES; (G) MATRIC SUCTION CHANGE TIME SERIES; (H) MEAN EFFECTIVE STRESS CHANGE TIME SERIES; (I) CYCLIC SHEAR STRESS AND CYCLIC SHEAR STRAIN LOOPS. 40

FIGURE 4.10 DATA SET 2 S_0=0.3: (A) SHEAR STRAIN TIME SERIES; (B) SHEAR STRESS TIME SERIES (C) DEGREE OF SATURATION TIME SERIES; (D) VOLUME CHANGE TIME SERIES; (E) PORE AIR PRESSURE CHANGE TIME SERIES; (F) PORE WATER PRESSURE CHANGE TIME SERIES; (G) MATRIC SUCTION CHANGE TIME SERIES; (H) MEAN EFFECTIVE STRESS

CHANGE TIME SERIES; (I) CYCLIC SHEAR STRESS AND CYCLIC SHEAR STRAIN LOOPS. 41

FIGURE 4.11 DATA SET 1* S_0=0.206: (A) SHEAR STRAIN TIME SERIES; (B) SHEAR STRESS TIME SERIES (C) DEGREE OF SATURATION TIME SERIES; (D) VOLUME CHANGE TIME SERIES; (E) PORE AIR PRESSURE CHANGE TIME SERIES; (F) PORE WATER PRESSURE CHANGE TIME SERIES; (G) MATRIC SUCTION CHANGE TIME SERIES; (H) MEAN EFFECTIVE STRESS CHANGE TIME SERIES; (I) CYCLIC SHEAR STRESS AND CYCLIC SHEAR STRAIN LOOPS. 42

FIGURE 4.12 DATA SET 2 S_0=0.2: (A) SHEAR STRAIN TIME SERIES; (B) SHEAR STRESS TIME SERIES (C) DEGREE OF SATURATION TIME SERIES; (D) VOLUME CHANGE TIME SERIES; (E) PORE AIR PRESSURE CHANGE TIME SERIES; (F) PORE WATER PRESSURE CHANGE TIME SERIES; (G) MATRIC SUCTION CHANGE TIME SERIES; (H) MEAN EFFECTIVE STRESS CHANGE TIME SERIES; (I) CYCLIC SHEAR STRESS AND CYCLIC SHEAR STRAIN LOOPS. 43

FIGURE 4.13 DATA SET 1 S_0=0.118: (A) SHEAR STRAIN TIME SERIES; (B) SHEAR STRESS TIME SERIES (C) DEGREE OF SATURATION TIME SERIES; (D) VOLUME CHANGE TIME SERIES; (E) PORE AIR PRESSURE CHANGE TIME SERIES; (F) PORE WATER PRESSURE CHANGE TIME SERIES; (G) MATRIC SUCTION CHANGE TIME SERIES; (H) MEAN EFFECTIVE STRESS CHANGE TIME SERIES; (I) CYCLIC SHEAR STRESS AND CYCLIC SHEAR STRAIN LOOPS. 44

FIGURE 4.14 DATA SET 2 S_0=0.117: (A) SHEAR STRAIN TIME SERIES; (B) SHEAR STRESS TIME SERIES (C) DEGREE OF SATURATION TIME SERIES; (D) VOLUME CHANGE TIME SERIES; (E) PORE AIR PRESSURE CHANGE TIME SERIES; (F) PORE WATER PRESSURE CHANGE TIME SERIES; (G) MATRIC SUCTION CHANGE TIME SERIES; (H) MEAN EFFECTIVE STRESS CHANGE TIME SERIES; (I) CYCLIC SHEAR STRESS AND CYCLIC SHEAR STRAIN LOOPS. 45

FIGURE 4.15 DATA SET 1* S_0=0 (DRY): (A) SHEAR STRAIN TIME SERIES; (B) SHEAR STRESS TIME SERIES; (C) VOLUME CHANGE TIME SERIES; (D) PORE AIR PRESSURE CHANGE TIME SERIES; (E) MEAN EFFECTIVE STRESS CHANGE TIME SERIES; (F) CYCLIC SHEAR STRESS AND CYCLIC SHEAR STRAIN LOOPS. 46

FIGURE 4.16 DATA SET 2* S_0=0 (DRY): (A) SHEAR STRAIN TIME SERIES; (B) SHEAR STRESS TIME SERIES; (C) VOLUME CHANGE TIME SERIES; (D) PORE AIR PRESSURE CHANGE TIME SERIES; (E) MEAN EFFECTIVE

STRESS CHANGE TIME SERIES; (F) CYCLIC SHEAR STRESS AND CYCLIC SHEAR STRAIN LOOPS. 47

FIGURE 5.1: LINEAR TRANSFORMATION OF HYPERBOLIC SHEAR STRESS-STRAIN RELATIONSHIP. 54

FIGURE 5.2 HYPERBOLIC FITTING PROCESS FOR THE FIRST 0.25 CYCLES OF THE DRAINED CYCLIC SIMPLE SHEAR TEST TO 1% SHEAR STRAIN: (A) MONOTONIC LOADING TO 1% SHEAR STRAIN; (B) LINEARIZATION OF CURVE TO FIND HYPERBOLIC PARAMETERS. 54

FIGURE 5.3 HYPERBOLIC FITTING PROCESS FOR THE FIRST 0.25 CYCLES OF THE DRAINED CYCLIC SIMPLE SHEAR TEST TO 3% SHEAR STRAIN: (A) MONOTONIC LOADING AT 3% SHEAR STRAIN; (B) LINEARIZATION OF CURVE TO FIND HYPERBOLIC PARAMETERS. 55

FIGURE 5.4 COMPARISON OF THE CALIBRATED BACKBONE AND HYSTERETIC SHEAR STRESS-STRAIN CURVES WITH THE EXPERIMENTAL DATA FOR $S_0 = 0.3$ AND $\sigma_V = 50$ KPA FROM DRAINED CYCLIC SIMPLE SHEAR TESTS PERFORMED BY RONG AND MCCARTNEY (2020A). 55

FIGURE 5.5 TRANSIENT SWRC WETTING PATHS OF UNDRAINED CYCLIC SHEAR DATA SET 1 AFTER 200 CYCLES. 56

FIGURE 5.6 SLOPES OF TRANSIENT SWRC WETTING PATHS OF DATA AFTER 1.25 CYCLES OF UNDRAINED CYCLIC SIMPLE SHEAR. 56

FIGURE 5.7 (A) SLOPES OF THE TRANSIENT SWRC SCANNING CURVE WITH AVERAGES AT 1.25 CYCLES AND 200 CYCLES; (B) EMPIRICAL PREDICTION OF THE SLOPE OF THE TRANSIENT SWRC SCANNING CURVE WITH DEGREE OF SATURATION IN THE FUNICULAR REGIME FOR 200 CYCLES. 56

FIGURE 6.1 COMPARISON BETWEEN CYCLIC SIMPLE SHEAR RESULTS FOR A SPECIMEN WITH $S_0 = 0.3$ AND MODEL RESULTS: (A) VOLUME COMPRESSION AFTER 200 CYCLES; (B) MEAN EFFECTIVE STRESS CHANGES AFTER 200 CYCLES; (C) PORE AIR PRESSURE AFTER 200 CYCLES; (D) PORE WATER PRESSURE AFTER 200 CYCLES; (E) SUCTION STRESS AFTER 200 CYCLES; (F) TRANSIENT SCANNING PATH AFTER 200 CYCLES. 64

FIGURE 6.2. DATA SET 1 VS. MODEL PREDICTIONS: (A) VOLUMETRIC STRAIN VS. CYCLES; (B) MODEL: VOLUMETRIC STRAIN VS. CYCLES; (C) MATRIC

SUCTION VS. CYCLES; (D) SATURATION VS. CYCLES; (E) DATA: MEAN STRESS VS. CYCLES; (F) MODEL: MEAN STRESS VS. CYCLES.....65

FIGURE 6.3 COMPARISON OF TRENDS BETWEEN CUMULATIVE CHANGES IN KEY HYDRO-MECHANICAL VARIABLES AFTER 15 CYCLES OF UNDRAINED CYCLIC SHEARING AND THE INITIAL DEGREE OF SATURATION OBTAINED FROM THE EXPERIMENTS OF RONG AND MCCARTNEY (2020B) AND THE MODEL: (A) $\Delta\Psi$ VS. S_0; (B) ΔU_A VS. S_0; (C) ΔU_W VS. S_0; (D) ΔV VS. S_0; (E) $\Delta\Sigma'_M$ VS. S_0.....66

FIGURE 6.4 COMPARISON BETWEEN MODEL PREDICTIONS AND EXPERIMENTAL RESULTS OF CUMULATIVE CHANGES IN DIFFERENT VARIABLES AFTER 200 CYCLES OF UNDRAINED SHEARING: (A) $\Delta\Psi$ VS. S_0; (B) ΔU_A VS. S_0; (C) ΔU_W VS. S_0; (D) ΔV VS. S_0; (E) $\Delta\Sigma'_M$ VS. S_0. 67

FIGURE 6.5 TRANSIENT SWRC SCANNING PATHS AND PREDICTED TRANSIENT SWRC PATHS FOR DATA SET 1. 68

FIGURE 6.6 MODEL PREDICTIONS OF PORE AIR PRESSURE GENERATION BY INITIAL SATURATION AFTER: (A) 15 CYCLES; (B) 200 CYCLES. 69

FIGURE 6.7 VARIATION IN RESULTS BETWEEN DATA SET 1 TRANSIENT SWRC: (A) S_0=0.3, Ψ_0=4 KPA MODEL CALIBRATED TO 1.25 CYCLES; (B) S=0.3 Ψ=4 KPA MODEL CALIBRATED TO 200 CYCLES.....70

FIGURE 6.8 VARIATION IN RESULTS BETWEEN DATA SET 1 MATRIC SUCTION VS. N CYCLES: (A) S_0=0.3, Ψ_0=4 KPA MODEL CALIBRATED TO 1.25 CYCLES; (B) S_0=0.3, Ψ_0=4 KPA MODEL CALIBRATED TO 200 CYCLES. 70

FIGURE A.1: DEPICTION OF BACKBONE CURVE WITH A HYSTERETIC LOOP DEPICTING SHEAR STRAIN RANGE OF 1% REPRESENTING 1.25 CYCLES OF SHEAR STRAIN.....92

FIGURE A.2: LINEAR TRANSFORMATION OF HYPERBOLIC SHEAR STRESS-STRAIN RELATIONSHIP. 92

FIGURE A.3: VARIATION OF INITIAL SHEAR MODULUS WITH CHANGING MEAN STRESS. 93

FIGURE A.4. NORMALIZED SHEAR STRESS-SHEAR STRAIN CURVE.....93

FIGURE A.5: (A) BEFORE CYCLING AIR PRESSURE AND VOLUME (B) AFTER CYCLING AIR PRESSURE AND VOLUME. 94

FIGURE A.6: THREE PHASE SYSTEM OF AIR (WHITE), WATER (BLUE), AND SOLIDS (BROWN) IN THE FUNICULAR REGION OF SWRC.....94

FIGURE A.7. IDEALIZED IMAGE OF VOLUMES OF A 3-PHASE SYSTEM.....95

FIGURE A.8. THREE-PHASE SYSTEM NEW RELATIONSHIP. 95

FIGURE A.9. THREE-PHASE SYSTEM DEFINED IN TERMS OF SATURATION AND VOID RATIO.....95

FIGURE A.10 COMPARISON BETWEEN EXPERIMENTAL RESULTS AND MODEL PREDICTIONS FOR A SAND SPECIMEN WITH S_O=0.117, ψo=10 KPA: (A) VOLUME CHANGE; (B) DEGREE OF SATURATION; (C) PORE AIR PRESSURE; (D) MATRIC SUCTION; (E) PORE WATER PRESSURE; (F) MEAN EFFECTIVE STRESS; (G) DEGREE OF SATURATION VS. MATRIC SUCTION. 96

FIGURE A.11 COMPARISON BETWEEN EXPERIMENTAL RESULTS AND MODEL PREDICTIONS FOR A SAND SPECIMEN WITH S_O=0.2, ψo=6 KPA FOR SWRC FIT TO LOW CYCLES: (A) VOLUME CHANGE; (B) DEGREE OF SATURATION; (C) PORE AIR PRESSURE; (D) MATRIC SUCTION; (E) PORE WATER PRESSURE; (F) MEAN EFFECTIVE STRESS; (G) DEGREE OF SATURATION VS. MATRIC SUCTION. 97

FIGURE A.12 COMPARISON BETWEEN EXPERIMENTAL RESULTS AND MODEL PREDICTIONS FOR A SAND SPECIMEN WITH S_O=0.3, ψo=4 KPA FOR SWRC FIT TO LOW CYCLES: (A) VOLUME CHANGE; (B) DEGREE OF SATURATION; (C) PORE AIR PRESSURE; (D) MATRIC SUCTION; (E) PORE WATER PRESSURE; (F) MEAN EFFECTIVE STRESS; (G) DEGREE OF SATURATION VS. MATRIC SUCTION. 98

FIGURE A.13 COMPARISON BETWEEN EXPERIMENTAL RESULTS AND MODEL PREDICTIONS FOR A SAND SPECIMEN WITH S_O=0.4, ψo=3 KPA FOR SWRC FIT TO LOW CYCLES: (A) VOLUME CHANGE; (B) DEGREE OF SATURATION; (C) PORE AIR PRESSURE; (D) MATRIC SUCTION; (E) PORE WATER PRESSURE; (F) MEAN EFFECTIVE STRESS; (G) DEGREE OF SATURATION VS. MATRIC SUCTION. 99

FIGURE A.14 COMPARISON BETWEEN EXPERIMENTAL RESULTS AND MODEL PREDICTIONS FOR A SAND SPECIMEN WITH S_O=0.56, ψo=2 KPA FOR SWRC FIT TO LOW CYCLES: (A) VOLUME CHANGE; (B) DEGREE OF SATURATION; (C) PORE AIR PRESSURE; (D) MATRIC SUCTION; (E) PORE WATER PRESSURE; (F) MEAN EFFECTIVE STRESS; (G) DEGREE OF SATURATION VS. MATRIC SUCTION. 100

1 INTRODUCTION

1.1 SEISMIC COMPRESSION OF UNSATURATED SOILS

This study is focused on predicting the volume change response of unsaturated soils during cyclic or seismic shearing, a phenomenon referred to as seismic compression (Stewart et al. 2004). Unsaturated soil profiles are encountered near the earth's surface in both natural and engineered settings. Natural unsaturated soil profiles are encountered when the water table is below the ground surface. The depth of the water table may vary with time due to infiltration, evaporation or groundwater flow. In addition to founding structures in natural unsaturated soil profiles, natural unsaturated soil profiles are encountered when making cuts into the subsurface to form excavations or changes in grade. Engineered unsaturated soil profiles are encountered in fill-type geostructures like embankments and retaining walls constructed above the ground surface and the water table. Although they may be affected by infiltration and evaporation, drainage systems are typically included in fill-type geostructures to help ensure that they remain in unsaturated conditions. Embankments and retaining walls are employed in transportation infrastructure to ensure that pavements, railways, and bridge abutments remain above the water table.

Unsaturated soils contain air, water, and solids. The amount of water in unsaturated soils can be represented by the degree of saturation (volume of water per volume of voids), the volumetric water content (volume of water per total volume), or the gravimetric water content (mass of water per mass of solids). These variables can be used interchangeably and are related through phase relationships. The energy state in the pore water of unsaturated soils with respect to free water is typically represented by the matric suction, which is equal to the difference between the pore water and air pressures in the soil. A difference between the pore water and air pressures forms due to the curvature of the air-water interface (referred to as a meniscus) associated with the surface tension of water and the water-solid contact angle. The degree of saturation, matric suction, and pore air pressure are important variables that can have effects on the effective stress in the unsaturated soil profile. The shear strength and stiffness of the unsaturated soil are both closely tied with the effective stress, indicating that the mechanical response of the unsaturated soil profile is coupled with the hydraulic conditions in the soil.

During cyclic or seismic shearing of unsaturated soils, a reduction in total volume of the soil may occur as the particles rearrange into a tighter configuration and the void space is decreased (Youd 1972; Tatsuoka and Ishihara 1974; Chong and Santamarina 2016; Le and Ghayoomi 2017; Rong and McCartney 2020a, 2020b). Although it is well known that loose soils contract and dense soils dilate during monotonic shearing, both loose and dense sands are expected to experience seismic compression during cyclic or seismic shearing (Youd 1972). Drainage conditions for the pore fluids in a soil is known to have a major effect on the seismic shearing response. The pore air and water pressures may change during this process during undrained shearing, which may occur in a soil layer with no drainage boundaries or when the rate of shearing is faster than the rate of pore

fluid drainage (Okamura and Soga 2006; Unno et al. 2008; Okamura and Noguchi 2009; Oka et al. 2010; Rong and McCartney 2020b). Regardless of the drainage conditions, the degree of saturation is expected to increase as the volume of voids decreases (Rong and McCartney 2020a, 2020b). The changes in pore fluid pressures and degree of saturation will lead to changes in the effective stress state in the soil, which controls the shear strength and stiffness of the soil. In engineered unsaturated soil profiles, it is imperative to understand the changes in volume for soils having different initial degrees of saturation because changes in volume and associated changes in hydro-mechanical variables will result in settlements of the soil layer and a reduction in effective stress. Settlements and changes in effective stress may have significant impacts on the performance of overlying structures supported by the unsaturated soil layer.

Seismic compression is defined as the accrual of permanent contractive volumetric strains in soils during earthquakes and has been recognized as a major cause of seismically-induced damage in earth structures (Stewart et al. 2001, 2004; Konagai et al. 2013). A report on the effects of the Northridge earthquake by Stewart et al. (1995) found that seismic compression of fills caused damages on the order of $50,000 to $100,000 per lot over 2,000 sites. Konagai et al. (2013) reported surface settlement of fill soils along the northeastern shorelines of Tokyo Bay during the 2011 Tohoku earthquake. Surface settlements measured at locations 12-20 m away from the pile were 300-400 mm and gradually increased to approximately 870 mm alongside the base wall. It was verified that the backfill, which primarily experienced seismic compression, was in unsaturated state as the ground water level was found to be at a depth of 25 m. Although backfill soils in fill-type geostructures are typically in an initially dense state and are expected to have minimal settlement under static or traffic loading, they may still experience volumetric contraction during earthquakes. Even small backfill settlements can have a negative impact on the functionality of transportation systems and can lead to high repair costs. Accordingly, it is critical to have a constitutive model that can be used to predict the seismic compression of unsaturated soils and consider the hydro-mechanical coupling mentioned in the previous paragraph.

1.2 RESEARCH OBJECTIVES

The current state of the practice in prediction of seismic compression during earthquakes is to empirically relate vertical strain profiles with depth to the shear strain induced in a soil layer as part of a site response analysis (Yee and Stewart 2011; Yee et al. 2011). This is a practical approach as it builds upon analyses performed for the earthquake site response but does not necessarily consider hydro-mechanical coupling observed in laboratory experiments. While complex elasto-plastic models have been developed to simulate the cyclic response of unsaturated soils, many do not consider hydro-mechanical coupling (e.g., Khalili et al. 2005). Other elasto-plastic models have been developed to consider hydro-mechanical coupling (e.g., Wheeler et al. 2003; Sheng and Zhou 2011) but have not been applied to study seismic compression under cyclic shearing. Alternatively, empirical models have been developed to predict the seismic compression of unsaturated soils by separately considering collapse of air voids and post-shaking reconsolidation (e.g., Ghayoomi et al. 2013; Ghayoomi and McCartney 2016). These empirical models were developed by extending models for saturated soils or dry soils (e.g., Seed and Idriss 1971; Seed

and Silver 1972; Lee and Albaisa 1974; Finn and Byrne 1976; Wu and Seed 1984; Tokimatsu and Seed 1987; Pradel 1998) to unsaturated soils using a limited amount of data (Ishihara and Yoshimine 1992; Ishihara 2001), which can lead to uncertainty. Further, it can be difficult to objectively define the parameters for these empirical models. Accordingly, based on this gap in the literature, the objective of this study is to develop a constitutive model that can represent the hydro-mechanical coupling expected in unsaturated soils undergoing seismic compression during cyclic or seismic shearing, with particular focus on the funicular regime of the soil-water retention curve (SWRC) where experimental data is available for calibration. The greatest amount of seismic compression is expected in the funicular regime due to the presence of both air and water. This constitutive model is intended to be simple so that properties can be calibrated with non-specialized laboratory tests and to facilitate implementation into software packages typically used to perform geotechnical earthquake engineering simulations (OpenSees, FLAC, etc.).

1.3 RESEARCH APPROACH

The research approach in this study is to develop a semi-empirical constitutive model that links the plastic volume changes during undrained cyclic shearing of an unsaturated soil to the changes in degree of saturation and pore fluid pressures, then use these to update the effective stress and shear modulus that control the further evolution in plastic volume changes. Specifically, an elasto-plastic model with a hyperbolic stress-strain curve is used to capture the hysteretic response of the soil to cyclic shearing, and a flow rule derived from energy considerations is used to predict the evolution in plastic volumetric strain. The plastic volumetric strains are then used to estimate changes in pore air pressure from Boyle's Law, the Ideal Gas Law and Henry's Law during undrained cyclic simple shear. Assuming undrained conditions, the degree of saturation calculated from the plastic volumetric strain is also used to estimate changes in matric suction using the transient scanning curves of the soil-water retention curve for the soil. Changes in the small-strain shear modulus of the soil are then estimated using the mean effective stress computed from the constant total stress and the varying pore air pressure, degree of saturation and matric suction. The parameters of the elasto-plastic model were calibrated from triaxial tests on dry sand and the backbone curve from a drained cyclic simple shear test. The model was then validated using experimental data from a series of undrained cyclic simple shear tests on unsaturated sand specimens having a relative density of 45%, a constant vertical normal stress of 50 kPa, and different initial degrees of saturation in the funicular regime.

1.4 REPORT ORGANIZATION

Following this introduction, Chapter 2 presents an introductory section to the mechanics of unsaturated sands. A literature review is presented to illustrate the historical understanding of unsaturated soil mechanics from inception to present day design practices. The model and results illustrate the difficulties in developing predictive earthquake designs for unsaturated sands due to the complexities in soil skeleton pore network relationships. Chapter 2 also presents the different static mathematical derivations for the effective stress equation of unsaturated sands. In addition,

Chapter 2 includes the dynamic analysis of unsaturated sands during seismic compression in literature and derivation of a sand specimen's backbone curve. Chapter 3 presents a model to predict the cyclic shearing of undrained unsaturated sand due to multiple cycles of applied shear strain using semi-empirical equations derived from initial cycling data. Chapter 4 provides a brief description of the drained and undrained cyclic simple shear data collected from experiments performed by Rong and McCartney (2020b). Chapter 5 focuses on the calibration of the model, including the hyperbolic stress-strain curve model parameters, the failure model parameters, and the pore water pressure generation model parameters. While the pore air pressure generation model does not require soil-specific calibration, because it is based solely on the predicted plastic volumetric strain and initial soil conditions, the pore water pressure generation model calibration requires the definition of a slope of the transient SWRC scanning curve paths that depends on the initial degree of saturation of the sand.

A comparison between the model prediction and a set of experimental data from Rong and McCartney (2020b) is presented in Chapter 6. Specifically, this includes a comparison of the evolution of the key hydro-mechanical variables during cyclic shearing for sands having the same initial relative density of 45% with different initial degrees of saturation under a cyclic shear strain amplitude of 1% and a frequency of 1 Hz for 200 cycles. Chapter 6 also includes comparisons of the trends in the hydro-mechanical variables as a function of the initial degrees of saturation obtained after 15 and 200 cycles to demonstrate how the trends evolve with cycles. The conclusions from the model development and the observations from the comparison between the model and experiments are summarized in Chapter 7. Chapter 7 also includes a summary of developments which may help improve the model predictions and recommendations to guide future experiments. This report also includes several appendices that include detailed derivations of key equations used in the model along with the full time series for all model results compared against the undrained cyclic simple shear data on sand specimens initially in the funicular regime of the SWRC performed by Rong and McCartney (2020b).

2 BACKGROUND AND LITERATURE REVIEW

2.1 UNSATURATED SOILS

In most settlement methods used in soil mechanics designs, soils are typically assumed to be in either dry or saturated conditions. This assumption is partly due to simplicity, and partly due to the belief that these two extremes in the degree of saturation (0 for dry soils and 1 for saturated soils) will yield worst-case scenarios for design as the air-water menisci in unsaturated soils will provide increased interparticle connections. A saturated soil is a two-phase system composed of soil solids with void spaces totally occupied by fluid water. A dry soil is also a two-phase system composing of a soil solid with all void spaces occupied by fluid air. Although fully saturated soils are encountered below the water table or in soils beneath lakes or oceans, it is rare to encounter fully dry soils because soil layers usually are continuously interacting with the atmosphere. In general, soils above the capillary fringe overlying the water table can be characterized as a three-phase system consisting of soil solids and two fluids: air and water.

In nature, the hydrologic cycle of water on earth will have various movements in and out of the superficial ground soil through precipitation, infiltration, and evaporation processes. Since the movement of water will continue throughout seasonal periods, the ground soil can anticipate degrees of saturation (S) ranging from $0<S<1$. The zone above the water table is referred to as the vadose zone. An illustration of the vadose zone is shown in Figure 2.1 along with typical profiles of degree of saturation, pore water pressure (u_w), total stress (σ), and effective and horizontal vertical stresses representative of hydrostatic conditions (i.e., no infiltration or evaporation). It is possible for soils to be saturated above the water table within the capillary fringe designated by the dashed red line in Figure 2.1.

The vadose zone can be subdivided into three zones: the capillary fringe, the funicular zone, and the pendular zone. The capillary fringe is the zone located immediately above the water table source and is saturated or nearly saturated with water. If air is present in the capillary regime, it is in the form of occluded bubbles that may have become trapped during fluctuations in the water table depth. The height of the capillary fringe is related to the air entry suction for the soil, which will be introduced later. The funicular zone occurs where the void spaces between the soil particles are filled with both air and water. As the air enters the pores, desaturation commences, and menisci form between the air and water, with the water wetting to the hydrophilic soil particles. The air and water phases in the soil are typically continuous in the funicular regime. In the pendular zone at heights well above the water table, the pore water is discontinuous and is only present in thin films around the soil particles while the air phase is continuous throughout the void space.

The depth of the water table is defined as the location where the pore water pressure is zero (when the pressure is defined in terms of gage pressure with reference to the atmospheric pressure). Below

the water table, the water is continuous (no curvature or interfacial tension due to the lack of air) throughout the soil skeleton and is under positive pore water pressures. Above the water table, the pore water is under negative pore water pressures. Negative water pressures arise from capillary forces at the curved air-water interface. Although it is common to assume that pore air pressures are equal to zero (in gage pressure) or equal to the atmospheric pressure (in absolute pressure), the air pressure may not be zero if the air is occluded within the water phase or if void collapse causes compression of air-filled voids. Regardless, because of the negative pore water pressures, positive matric suction is exhibited in the soil above the water table as the matric suction is equal to the difference between the pore air pressure and pore water pressure. Different soils such as clays and sands will have different distributions of degree of saturation above the water table, which are governed by the SWRC as shown in Figure 2.2. The shape of the SWRC is related to the pore size distribution and soil particle mineralogy, which will lead to different interactions between the pore water and the soil solids that can be referred to as adsorption. For granular soils like sands and gravel, the SWRC is mainly related to the pore size distribution and capillarity caused by air-water menisci at the particle contacts. The SWRC is path dependent and will have different shapes depending on whether the soil is being wetted or dried, a phenomenon referred to as hydraulic hysteresis, an example of which is shown in Figure 2.3.

Seasonal water movement either due to infiltration or evaporation from the ground surface or due to water table fluctuations will not only change the distribution in water within the soil layer and the pore air and water pressures, but the presence of water in the soil may change the total unit weight of the soil. Water movement or fluctuating ground water tables could present issues with slope instability due to increases in pore fluid pressures or deformation changes related to effective stress changes, which are described in the next section. As water is superficially evaporated due to earthen heating cycles, this change in degree of saturation could lead to shrinkage of the soil skeleton due to the changes to the effective stress state. This study assumes that there is no water movement in an unsaturated soil layer due to infiltration or evaporation or water table fluctuations, and that changes in pore air and water pressures or degree of saturation are only caused by cyclic or seismic shearing of the soil layer.

2.2 EFFECTIVE STRESS IN UNSATURATED SOILS

Terzaghi (1936) defined the effective stress in a fully saturated soil as the total stress state in a three-dimensional cartesian coordinate minus the neutral orthogonal pressures (also called the pore water pressures). For example, the vertical effective stress σ'_v can be defined as follows:

$$\sigma_v' = (\sigma_v - u_w) \tag{2.2.1}$$

where σ_v is the total stress and u_w is the pore water pressure. In a free-field condition with hydrostatic conditions, the total stress is equal to the depth below the ground surface multiplied by the total unit weight of the soil, and the pore water pressure is equal to the depth of a point of interest below the water table multiplied by the unit weight of water. Use of Terzaghi's effective stress implies that the water pressure acts in every direction with equal intensity and the difference

between the total stress and pore water describes the stress state of the soil structure (Fredlund 2016). Terzaghi's effective stress equation is still continuously used in design practices to describe the stress state change for a soil beneath the ground water table (i.e., fully saturated soil).

Bishop (1959) and Bishop and Blight (1963) proposed a definition for the effective stress state of an unsaturated soil, given as follows:

$$\sigma_v' = (\sigma_v - u_a) + \chi(u_a - u_w) \tag{2.2.2}$$

where the term $\psi = (u_a - u_w)$ is the matric suction and describes the air-capillary water interface and adsorptive forces within the pores, $\sigma_n = (\sigma_v - u_a)$ is the net vertical stress, and χ is an effective stress parameter that is a property of the soil and must be defined experimentally. In wet sands, adsorptive forces are negligible and negative pore water stresses contribute an apparent cohesive strength through capillarity arising from air-water surface tension (Lu and Likos 2004). For clays, adsorptive forces associated with particle-water interaction associated with clay mineralogy play a more important role in water retention (Lu et al. 2016). χ is equal to 1 when the soil is fully saturated, and the equation reduces to Terzaghi's effective stress given in Equation 2.2.1. χ is equal to zero when the soil is dry with air filling all the voids, and the effective stress is equal to the net stress:

$$\sigma_v' = (\sigma_v - u_a) = \sigma_n \tag{2.2.3}$$

Many definitions have been proposed for χ, but most researchers have assumed that it is linked with the degree of saturation or matric suction in the soil. For example, Lu et al. (2010) assumed that χ is equal to the effective saturation (S_e), which can be defined as follows:

$$S_e = (S - S_{res})/(1 - S_{res}) \tag{2.2.4}$$

where S_{res} is the residual saturation. An advantage of using this definition is that the effective saturation is linked to the suction through the SWRC. When setting χ equal to the effective saturation in Equation 2.2.2, Lu et al. (2010) proposed the definition of a new variable referred to as the suction stress, given as follows:

$$\sigma_s = S_e\,(u_a - u_w) \tag{2.2.5}$$

In this manner, the vertical effective stress in an unsaturated soil can now be defined from Equation 2.2.2 as follows:

$$\sigma_v' = (\sigma_v - u_a) + \sigma_s \tag{2.2.6}$$

This equation indicates that unsaturated conditions will lead to an increase in the effective stress of the soil. However, the effect of matric suction on the effective stress will depend on the amount of water in the soil through the effective saturation. For example, the matric suction will increase linearly with height above the water table for the hydrostatic profiles shown in Figure 2.1, but the effective saturation will decrease with height above the water table according to the shape of the SWRC. Accordingly, the SWRC provides the link between the state variables of matric suction

and water content which can be used to describe the amount of energy in the pore water voids for a given amount of saturation (Lu et al. 2010). The SWRC is also linked to the definition of the effective stress state of a soil if the density and pore void skeleton remain unchanged. The SWRC is the constitutive relationship at hydraulic equilibrium (no flow) between total suction and volumetric water content, gravimetric content, degree of saturation or effective saturation. Since hydraulic hysteresis occurs during the entry and/or exit of air and water in the pore voids of the soil skeleton, there will be two different curves corresponding to either the wetting or drying path of the soil (Khalili et al. 2008).

The water content, shape, radius, and packing arrangement of the solid particles will influence the shape of the SWRC and the range of effective stresses possible during wetting and drying (Lu et al. 2004). For sands, capillarity is the dominating suction mechanism, and the slope of the SWRC is controlled by the arrangement of the pore water menisci connecting the soil skeleton (Lu and Likos 2004).

A way to characterize the potential capillarity stresses in a soil profile is to have extensive knowledge about the soil's water retention properties during drying or wetting. Brooks and Corey (1966) derived a discontinuous function to characterize the permeability of air and water in terms of the air entry value or "bubbling pressure" which was used to help understand the hydraulic retention properties of soil. The air entry value is the quantity of suction at which the surface tension between air and water is overcome and air can begin entering the pore void spaces of a fully saturated soil transitioning to an unsaturated soil (i.e., drying curve). Air expulsion suction corresponds to the rewetting curve path and represents the suction at which water enters the air-filled voids during wetting (Khalili et al. 2008). While the SWRC model of Brooks and Corey (1966) best represents the mechanisms of air entry and water entry during drying and wetting, respectively, the SWRC model proposed by van Genuchten (1980) represents these processes using a smoother function that resolves issues with continuity in numerical modeling of water flow. The van Genuchten (1980) SWRC model is given as follows:

$$S_e = \left\{ \frac{1}{1+[\alpha_{vG}\,(u_a - u_w)]^{N_{vG}}} \right\}^{1-\frac{1}{N_{vG}}} \tag{2.2.7}$$

where α_{vG} and N_{vG} are empirical fitting parameters that are related to the inverse air entry pressure and the pore size distribution, respectively. Using the van Genuchten (1980) SWRC model, Lu et al. (2010) derived an equation the suction stress of the soil at a given density, given as follows:

$$\sigma_s = \left[\frac{u_a - u_w}{\left(1+[\alpha_{vG}(u_a - u_w)]^{N_{vG}}\right)^{1-\frac{1}{N_{vG}}}} \right] \tag{2.2.8}$$

The relationship between $(u_a - u_w)$ shown in Equation 2.2.8 (which can also be written in terms of S_e) is referred to as the suction stress characteristic curve (SSCC). Schematic examples of SSCCs for sand and clay are shown in Figure 2.4. Lu et al. (2010) found that if the pore size distribution parameter N_{vG} is larger than 2.0 (most common in sands and silts), the SSCC increases

and then decreases as the suction increases. When the pore size distribution parameter N_{vG} is less than 2.0 (most common in clays), the SSCC increases monotonically with suction.

The relationship between effective vertical stress (σ_v') and matric suction in an unsaturated soil can be calculated by combining the suction stress and net normal stress as follows (Lu et al. 2010):

$$\sigma_v' = (\sigma_n - u_a) + \left[\frac{u_a - u_w}{(1+[\alpha_{vg}(u_a-u_w)]^{N_{vg}})^{1-\frac{1}{N_{vg}}}}\right] \quad (2.2.9)$$

The effective stress obtained from the SWRC fitting parameters (α_{vG}, N_{vG}) only applies to the conditions where the pore size distribution is not changed, and the values of α_{vG}, N_{vG} should represent either the wetting or drying paths of the water retention curve. This implies that Equation 2.2.9 should be used with caution when studying seismic compression of unsaturated soils as the pore size distribution may change, and changes in water retention typically follow a wetting path.

2.3 CYCLIC RESPONSE OF SOILS

The dynamic response of soils is dependent upon the shear strain magnitude. Ground vibrations induce strain in the soil and can occur during heavy construction, factory machine vibrations or earthquakes. Earthquakes impose a range of wave types on soil layers, but it is well known that seismic shear waves have the greatest effect on permanent ground deformations (Hardin and Drnevich 1972). Various models have been developed from empirical data to predict the dynamic response of shear stress and strain in soils during dynamic loading or ground action (Hardin and Black 1968, 1969; Hardin and Drnevich 1972). The shear stress-strain behavior of soils can be idealized as a hyperbola using the small-strain shear modulus (G_i) and the ultimate shear stress, (τ_{ult}) to depict the initial stage of shear loading of a soil as shown in Figure 2.5 (Hardin and Drnevich 1972).

At small strains (10^{-4} to 10^{-3} %), soils typically behave in a linear elastic manner with a constant shear modulus equal to G_i. During cyclic shearing, interparticle connections remain intact without permanent particle rearrangement. At a certain threshold level of shear strain, cyclic shearing causes individual soil particle contacts to redistribute into denser arrangements resulting in distortion of the soil skeleton. Hardin and Drnevich (1972) idealized that the response of soil degradation to induced shearing can be captured by the ratio of the shear modulus at a given shear strain to the small strain shear modulus (G/G_i) as a function of the logarithm of the shear strain called the shear modulus reduction curve (Figure 2.6). Degradation of the shear modulus occurs at shear strains induced by earthquake or repeated dynamic loading greater than those in the elastic regime and result in irreversible deformations of the soil fabric. The decreasing trend in the reduction modulus curve as shear strain increases exemplifies the plastic evolutions occurring in the soil during cyclic shearing. Seismic compression is only expected when the cyclic shear strain amplitude is greater than the cyclic threshold shear strain.

Early studies observed that the small strain shear modulus of sands is governed by the void ratio and effective stress (Hardin and Drnevich 1972; Hardin 1978) but later studies revealed that it is also a function of the degree of saturation (e.g., Khosravi and McCartney 2009, 2012; Khosravi et al. 2010; Ng and Xu 2012; Hoyos et al. 2015; Dong et al. 2016, 2017). Hardin (1978) proposed the following empirical power law relationship to describe the relationship between the small strain shear modulus of a dry or saturated soil with the void ratio (e), overconsolidation ratio (OCR) and mean effective stress (σ_m'):

$$G_i = AF_e(OCR)^k P_a^{1-n}(\sigma_m')^n \quad (2.3.1)$$

where P_a is the atmospheric pressure and F_e is a void ratio factor given by:

$$F(e) = \frac{1}{0.3+0.7e^2} \quad (2.3.2)$$

Studies conducted on the shear modulus of unsaturated soils indicate that the small strain shear modulus will increase during drying of soils, with the results for several soils reinterpreted in terms of effective stress according to Equation 2.2.2 summarized by Khosravi and McCartney (2009). Khosravi and McCartney (2012) proposed an equation for the small strain shear modulus (G_i) of unsaturated soils using a double-hardening model extended from Equation 2.3.1:

$$G_i = AP_a \left[\frac{\sigma'_{mc0}}{(\sigma_m - u_a)} exp\left(\frac{\Delta e^p}{\lambda-\kappa}\right)\right]^K \left[\frac{(\sigma_m - u_a)}{\sigma'_m} exp(b[S_{e0} - S_e])\right]^{K'} \left(\frac{\sigma'_m}{P_a}\right)^n \quad (2.3.3)$$

where σ'_{mc0} is the initial mean effective preconsolidation stress and b, K, and K' are hardening parameters defined based upon the double-hardening model of Wheeler et al. (2003) to consider the effects of changes in void ratio or changes in degree of saturation on the shear modulus of unsaturated soils. Equation 2.3.3 can be used to capture hysteretic changes in the small-strain shear modulus during hydraulic hysteresis (drying and wetting). Khosravi and McCartney (2012) used this model to show that during drying at constant mean net stress, the shear modulus will increase but that during subsequent rewetting, the shear modulus will decrease upon a different path. This implies that drying and wetting of soils can lead to permanent changes in the shear modulus due to plastic hardening. One issue with the use of Equation 2.3.3 is that it is very difficult to apply in practice due to the number of parameters. Alternatively, Dong et al. (2016) proposed a simplified model for the small strain shear modulus of an unsaturated soil based on measurements of the small strain shear modulus using bender elements:

$$G_i^{unsat} = G_i^{sat}\left(\frac{1}{S_e}\right)^\beta \left(\frac{\sigma'_m}{P_a} + 1\right)^{\gamma_o} \quad (2.3.4)$$

where γ_o and β are empirical fitting parameters. This model was found to represent the small strain shear modulus of unsaturated soils well when hydraulic hysteresis is not present and has a consistent definition to that of Hardin (1978).

During cyclic shearing of a soil specimen, the sign of the shear strain will reverse, and the soil will be loaded and unloaded in a hysteretic manner. If the strain level is greater than the cyclic threshold shear strain, plastic deformations will occur and the hysteretic stress-strain curve will form a closed

loop, as shown in Figure 2.7. As the shear strain amplitude increases, a decrease in shear modulus is expected according to the shear modulus reduction curve shown in Figure 2.6, which has been represented by the following equation (Darendeli 2001):

$$\frac{G}{G_i} = \left[\frac{1}{1+\left(\frac{\gamma}{\gamma_r}\right)^a}\right] \tag{2.3.5}$$

where γ_r is a reference strain and a is an empirical fitting parameter. Menq (2003) developed a database of shear modulus data to estimate the empirical fitting parameters for sands. The seismic compression model developed in this study will use a form of Equation 2.3.5 that is related to the derivative of a hyperbolic stress-strain curve and will be introduced in Chapter 3.

The reversal shear stress is expected to follow the small strain shear modulus slope until reaching the threshold shear strain in the other direction at which point a nonlinear response. Shearing of the soil in the reverse direction is expected to follow the same trend as the initial direction shearing and the closed loop formed by the stress-strain curves in both directions of shearing is referred to as the shear stress-strain hysteresis loop. The area within the shear stress-strain hysteresis loop in Figure 2.7 can be used to calculate the damping ratio of the soil D, which is another key soil dynamic property (e.g., Vucetic et al. 1998). The seismic compression obtained from the semi-empirical model developed in this study depends only on the shear modulus G, so the damping ratio is not discussed further in this study even though it can be derived from the hysteretic stress-strain curve and is a necessary component of soil dynamics analyses in software like OpenSees and FLAC.

2.4 SEISMIC COMPRESSION OF UNSATURATED SOILS IN LITERATURE

Compression of soils is expected during cyclic or seismic shearing and may occur in either drained or undrained conditions depending on the rate of shearing (Youd 1972, Silver and Seed 1971; Rong and McCartney 2020a, 2020b). Historically in soil mechanics design, it has been considered conservative to assume the soil to be fully saturated or dry in settlement predictions as these are considered extreme cases of the soil's stress state (Tokimatsu and Seed 1987, Silver and Seed 1971). For saturated soils, seismic compression is not possible because the pore water is incompressible. Instead, cyclic or seismic shearing of saturated soils will lead to an increase in pore water pressure, which may result in liquefaction (Ishihara et al. 1975; Martin et al. 1975; Finn et al. 1975). It is possible that after liquefaction occurs, dissipation of the pore water pressures may lead to reconsolidation and corresponding settlements after the end of earthquake shaking (Bray and Olaya 2022). It is interesting to note that even a slight reduction of degree of saturation can increase the soil's resistance to liquefaction (Yoshimi et al. 1989; Tsukamoto et al. 2002; Okamura et al. 2006; Mele et al. 2019). For unsaturated soils, soil interparticle stresses will increase due to capillary effects, and occluded air bubbles can mitigate the generation of pore water pressures during seismic shearing. However, there are cases where unsaturated soils with relatively high

initial degrees of saturation can still liquefy under seismic excitation (Yoshimi et al. 1989; Unno et al. 2008; Sawada et al. 2006; Mele et al. 2019).

Ghayoomi et al. (2013) developed an empirical model that combined estimates of the post-liquefaction reconsolidation of unsaturated soils with estimates of the collapse of air-filled voids to predict the seismic compression of unsaturated soils in all three water retention regimes. Their model was able to capture trends in seismic compression of sand specimens with different initial degrees of saturation observed from centrifuge modeling shake table tests with partially drained conditions. However, the model includes many parameters that are not easy to determine which could have major effects on the trends in seismic compression as a function of the initial degree of saturation. The model being developed in this study focuses on predicting the seismic compression of unsaturated soils during earthquake shaking using hydro-mechanical coupling, and reconsolidation settlements due to dissipation of excess pore water pressures are not included.

In unsaturated soils with lower initial degrees of saturation, seismic compression is expected during strong shaking by earthquakes with shear strain amplitudes greater than the cyclic threshold shear strain (Stewart et al. 2004, Rong and McCartney 2020a, 2020b). Earthquakes and aftershocks often have rapid shearing with short durations that can lead to undrained conditions even for sands. Unsaturated soils have lower hydraulic conductivity than saturated soils, so it is expected that undrained conditions will be present in unsaturated soils during earthquake shaking. In undrained conditions, pore air and water pressures increase during shaking and compression of the air voids may occur which coincides with an increase in the saturation of the overall soil system. Several studies have performed cyclic triaxial tests (Unno et al. 2008; Kimoto et al. 2011) and cyclic simple shear tests (Whang et al. 2000, 2004, 2005; Duku et al. 2008, Craciun and Lo 2010; Yee et al. 2014; Milatz and Grabe 2015; Cuomo et al. 2017; Rong and McCartney 2020a, 2020b) to characterize the cyclic response of unsaturated soils. Early cyclic simple shear tests involved compaction of soils to different initial degrees of saturation followed by undrained shearing without measurement of changes in pore air or water pressures (Whang et al. 2000, 2004, 2005; Duku et al. 2008; Yee et al. 2014). It was not possible to separate the effects of hydro-mechanical coupling from the effects of soil structures induced by the compaction process. Other studies characterized the changes in pore air and water pressures and stress-strain responses during cyclic shearing (Unno et al. 2008; Kimoto et al. 2011; Craciun and Lo 2010; Milatz and Grabe 2015; Rong and McCartney 2020a, 2020b). Results from these studies indicate that it is critical to measure the pore air and water pressures in specimens with the same initial preparation conditions to effectively interpret the results from seismic shearing tests. In the funicular regime, Rong and McCartney (2020b) found that different changes in pore air and water pressures may occur during cyclic shearing, which is a focus of the model development in this study. In most of the studies on seismic compression, the soil skeleton compresses in response to the redistribution of the pore void spaces and the SWRC shifts in different ways depending on the drainage conditions (Rong and McCartney 2020a, 2020b).

A comparison of normalized seismic compression measurements from cyclic simple shear and centrifuge shake table testing with different drainage conditions is shown in Figure 2.8, along with trends in undrained cyclic simple shear results from Rong and McCartney (2020b) and with the

model prediction from Ghayoomi et al. (2013). The results in this figure indicate that there is not only considerable scatter in the data from different studies, but also inconsistency in the expected trends in seismic compression with the initial degree of saturation. It is important to note that the cyclic simple shear tests of Rong and McCartney (2020b, 2021b) are fully undrained where changes in pore air pressure can have an important role, while the centrifuge shake table tests of Ghayoomi et al. (2011) used to calibrate the model of Ghayoomi et al. (2013) are partially drained. Accordingly, one of the goals of this model is to provide a mechanistic framework to confirm the trends in seismic compression in the funicular regime of the SWRC for fully undrained conditions.

CHAPTER 2: FIGURES

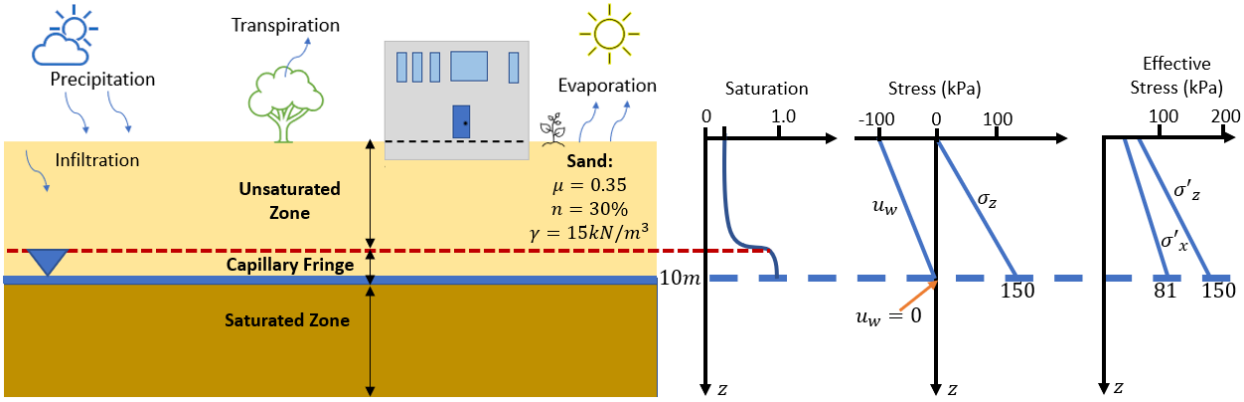

Figure 2.1 Typical near-surface unsaturated soil profile with hydrostatic conditions.

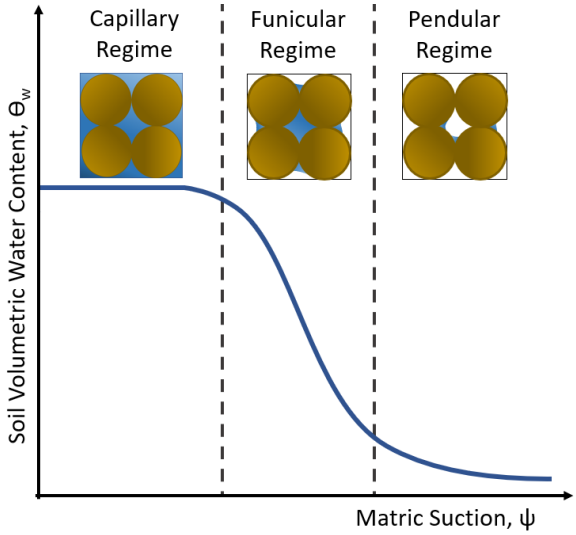

Figure 2.2 Typical shape of the soil-water retention curve (SWRC) partitioned into the capillary, funicular and pendular regimes defined by Lu and Likos (2004).

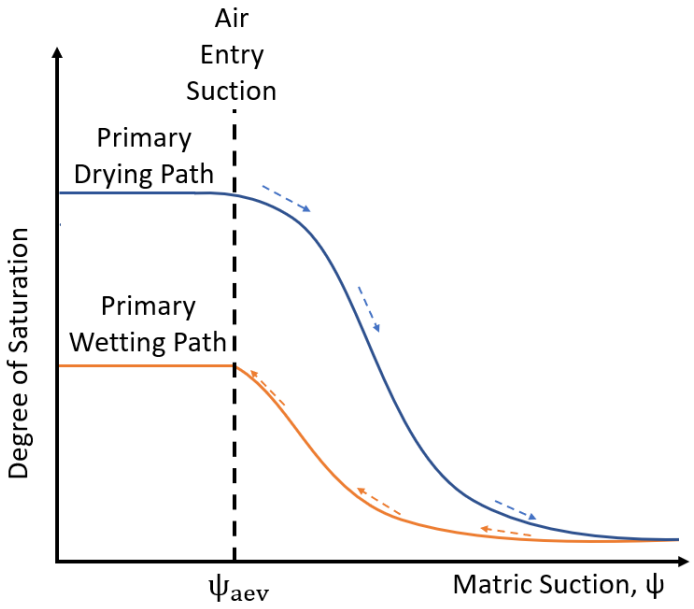

Figure 2.3 Schematic of a hysteretic SWRC showing typical shapes of the primary drying and wetting paths in blue and orange, respectively.

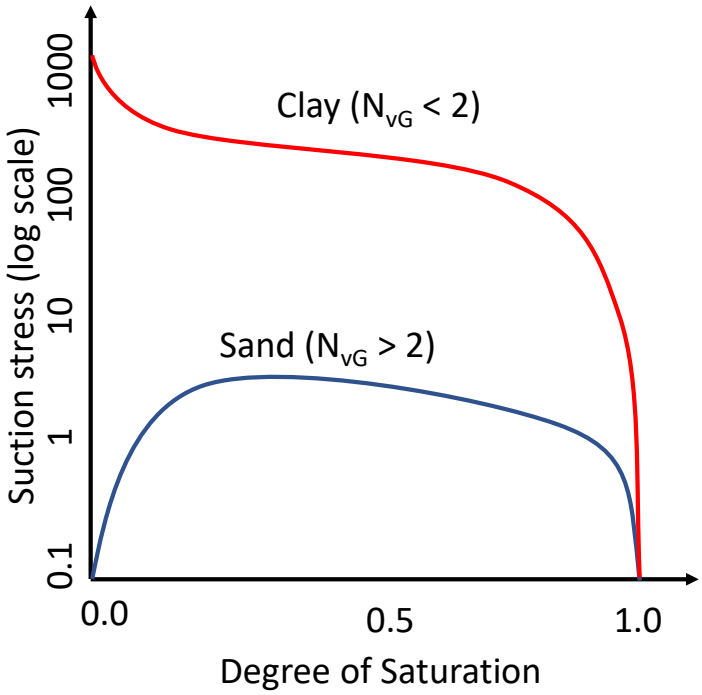

Figure 2.4 SSCCs representative of sands and clays.

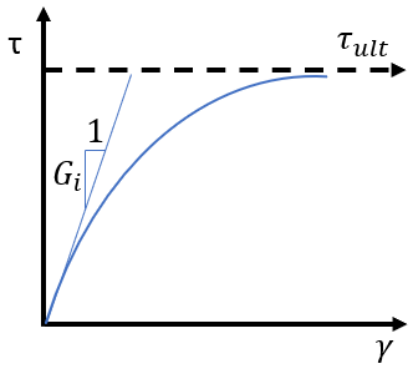

Figure 2.5 Schematic example of a hyperbolic shear stress-shear strain curve with a definition of the small strain shear modulus G_i.

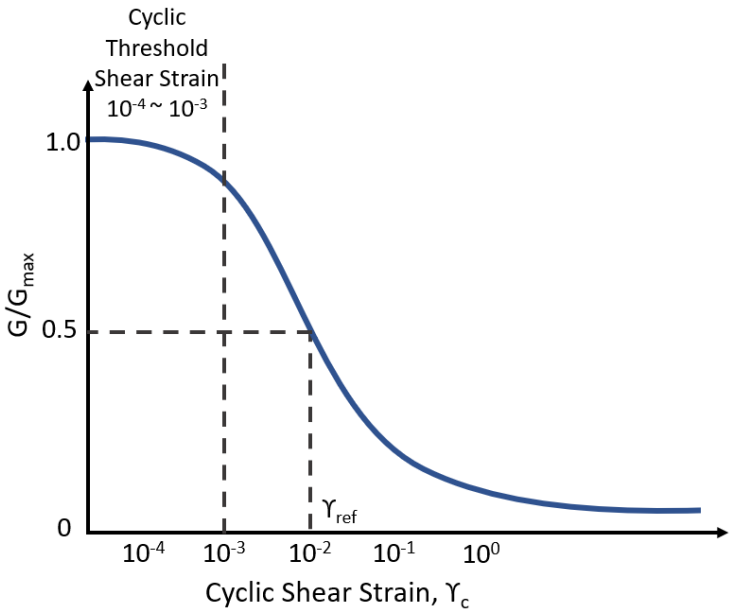

Figure 2.6 Schematic example of a shear modulus reduction curve.

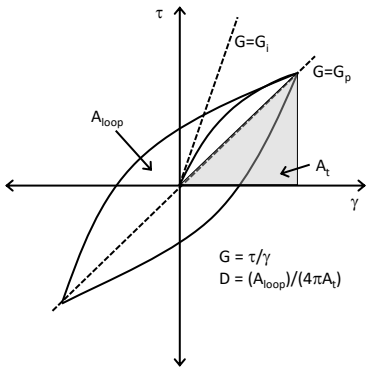

Figure 2.7 Schematic example of shear stress-strain hysteresis of soils during loading, unloading and reloading.

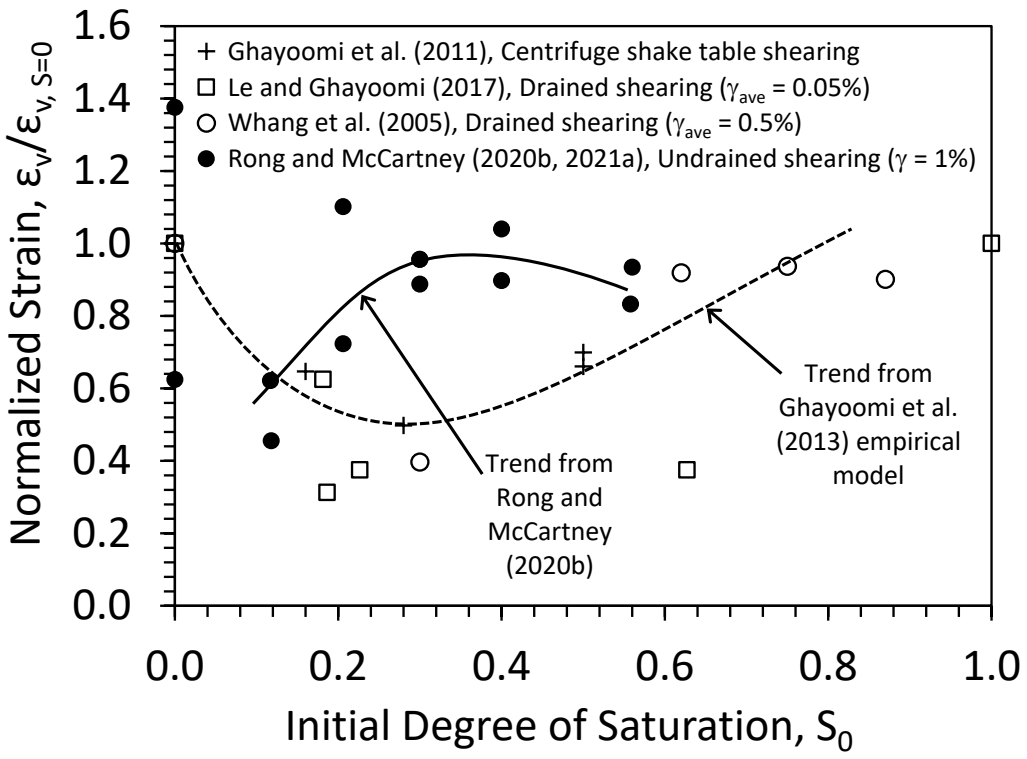

Figure 2.8 Trends in seismic compression measurements from unsaturated sands reported in the literature along with trends expected from the empirical model of Ghayoomi et al. (2013) and the trendline from Rong and McCartney (2020b).

3 SEISMIC COMPRESSION MODEL FOR THE FUNICULAR REGIME

3.1 DEFINITION OF STRESSES AND STRAINS DURING CYCLIC SIMPLE SHEAR TESTING

This study involves the development of a semi-empirical model for the seismic compression of unsaturated soils that is calibrated based on the results from undrained cyclic simple shear tests performed by Rong and McCartney (2020b). Cyclic simple shear tests first involve application of a vertical stress to a specimen confined with a housing that prevents lateral expansion, resulting in an at-rest initial stress state, as shown in the central figure of Figure 3.1. The horizontal stress is typically estimated using a coefficient of lateral earth pressure at rest, K_0, which can be defined using Jaky's equation and the friction angle or Hooke's law and elastic parameters. Then shear stresses are imposed to the specimen without changing the mean stress. In a cyclic simple shear test, the specimen is typically sheared in one direction until reaching the target cyclic shear strain amplitude, then the direction of shearing is reversed until reaching the cyclic shear strain amplitude in the other direction. The shear stresses required to reach the shear strain amplitude are recorded during the test and may decrease or increase depending on the changes in soil properties during shearing.

Mohr circles for a cyclic simple shear test are shown in Figure 3.2. The initial stress state is shown as a black circle, with $\sigma_h = K_0\sigma_v$. This initial anisotropic stress state implies that there are initially shear stresses in the specimen. A cyclic simple shear tests involves increasing the shear stresses applied to an element of soil, which leads to expansion of the circle about the same mean stress until reaching the blue circle. It is critical in a cyclic simple shear test that the blue circle does not reach the failure envelope. Reversal of the shear stresses makes the circle return to the at-rest state, after which shearing in the opposite direction causes the circle to expand back to the blue circle. The reversal of signs of the shear stresses during cyclic shearing is represented by the black and blue vertical lines on the Mohr circle. Because the mean effective stresses do not change during the cyclic simple shear test, a simplified constitutive model can be developed to represent seismic compression process that only focuses on the stress paths shown in Figure 3.2.

The first step in developing the semi-empirical constitutive model for seismic compression was to define a backbone curve. The backbone curve represents the shear stress-strain curve if the soil were sheared monotonically to failure (in either direction of shearing as shown in Figure 3.2). A major assumption of this study is that the backbone curve has the shape of a hyperbola. Hyperbolic models have been used most frequently to represent the stress-strain curves obtained from triaxial tests (e.g., Duncan et al. 1980) so several modifications are necessary to apply a hyperbolic model to cyclic simple shear tests. The equation for a hyperbolic shear stress strain curve, which provides the shear stress for any applied shear strain $\gamma_{applied}$, is given as follows:

$$\tau = \left(\frac{\gamma_{applied}}{\frac{1}{G_i} + \frac{\gamma_{applied} * R_f}{\tau_{ult}}} \right) \tag{3.1.1}$$

where G_i is the initial shear modulus (or small-strain shear modulus), τ_{ult} is the ultimate shear stress from the shape of the hyperbola, and R_f is a reduction factor that is used to adjust the curve to the actual shear stress at failure τ_f observed in an experiment. An example of a hyperbolic shear stress-strain curve in as shown in Figure 3.3. This figure also shows that as the shear strain increases, the shear modulus decreases from G_i to a lower value of plastic shear modulus G_p, which will be defined in the next section. A normalized version of the shear stress-strain curve is shown in Figure 3.3 in terms of the shear stress ratio $\eta = \tau/\sigma_m'$, $\eta_{ult} = \tau_{ult}/\sigma_m'$, and $\eta_f = \tau_f/\sigma_m'$.

Additional modifications are necessary to the hyperbolic model when simulating a cyclic simple shear test (Naesgaard 2011). Specifically, the backbone curve only represents the shape of the shear stress-strain curve for the first N = 0.25 cycles of shearing. When the applied shear strain is reversed, a hysteresis loop can be formed that has a different shape from the backbone curve but has the same parameters. The first step in defining the equations for this hysteresis loop is to define the cyclic shear stress τ_c that will occur during application of a certain cyclic shear strain amplitude γ_c is defined as follows:

$$\tau_c = \left(\frac{\gamma_c}{\frac{1}{G_i} + \frac{\gamma_c * R_f}{\tau_{ult}}} \right) \tag{3.1.2}$$

After reaching τ_c in a cyclic simple shear test after the number of cycles N = 0.25, the direction of shearing will be reversed until reaching τ_c in the opposite direction of shearing when N = 0.75. The equations for the hysteretic shear stress strain curves can be derived from the equation for the backbone curve. Specifically, the equation for the shear stress strain curve for increasing applied strain (shearing to the right in Figures 3.1 and 3.2) is given as follows:

$$\tau = \left(\frac{\gamma_c + \gamma_{applied}}{\frac{1}{G_i} + \frac{(\gamma_c + \gamma_{applied}) * R_f}{2 * \tau_{ult}}} \right) - \tau_c \tag{3.1.3}$$

Similarly, the equation for the shear stress strain curve for decreasing applied strain (shearing to the left in Figures 3.1 and 3.2) is given as follows:

$$\tau = \left(\frac{\gamma_c - \gamma_{applied}}{\frac{1}{G_i} + \frac{(\gamma_c - \gamma_{applied}) * R_f}{2 * \tau_{ult}}} \right) + \tau_c \tag{3.1.4}$$

In this sense, Equations 3.1.3 and 3.1.4 can be used to form a hysteretic shear stress-strain loop as shown in Figure 3.4. The backbone curve intersects the hysteresis loop at $\pm(\gamma_c,\tau_c)$.

3.2 PREDICTION OF VOLUMETRIC STRAIN DURING CYCLIC SHEARING

As the unsaturated specimen is cyclically sheared in undrained conditions, particles will move into denser arrangements causing volumetric contraction of the soil skeleton. A simplified schematic depicting the volumetric changes during undrained cyclic simple shearing of spherical particles is seen in Figure 3.5. Although the water in the unsaturated specimen will likely be distributed throughout the specimen height, water will take up more of the space after the specimen rearranges into a tighter packing, causing an increase in degree of saturation.

Due to the nonlinear shape of the hyperbolic stress-strain curve in Figure 3.4, it is assumed that each cycle of shearing will cause plastic shear strains. The experimental study of Youd (1971) suggests that plastic volumetric strains will thus occur during each cycle of shearing and will accumulate over multiple cycles. Accordingly, a flow rule is needed to relate the plastic shear strains with the plastic volumetric strains. The flow rule developed in the UBCSAND model was used to capture the indirect plastic volumetric strains caused by the shear stress-shear strain response of the soil. UBCSAND is a semi-empirical model described by Beaty and Byrne (2011) that combines a normalized semi-empirical hyperbolic shear stress-strain curve shown in Figure 3.6 with the elasto-plastic framework developed by Byrne et al. (1995). UBCSAND was originally developed to study the liquefaction behavior of sands and silty sands having relative densities less than 80% during monotonic shearing (Puebla et al. 1997) but was later extended to study liquefaction during earthquakes (Byrne and Park 2003; Byrne et al. 2004; Naesgaard 2011). This model has been adapted to study the liquefaction of unsaturated soils during earthquake shaking by assuming a combined bulk stiffness for the air and water pressures (Seid-Karbasi and Byrne 2006), but it has not been used to investigate the seismic compression of unsaturated soils.

In the UBCSAND model, the initial small strain shear modulus is dependent on the changes in the mean effective stress through the following relationship:

$$G_i = k_G^e P_a \left(\frac{\sigma'_m}{P_a}\right)^{n_e} \tag{3.2.1}$$

where n_e is the elastic shear modulus exponent that governs the effect of mean effective stress on the shear modulus and k^e_G is the elastic shear modulus number. The first quarter cycle of shear stress – shear strain response from a drained cyclic simple shear test (i.e., the backbone curve) is typically used to calibrate the best fit values of k^e_G and n_e. Chapter 5 includes a summary of the model calibration, and Appendix A.1 includes the procedure for defining the hyperbolic model parameters.

As mentioned, the shear stress-strain curve in the UBCSAND model is normalized. The normalized shear stress is defined as $\eta = \tau/\sigma_m'$. The plastic shear modulus is the ratio of the plastic

shear stress and the plastic shear strain. To avoid having to carry the mean effective stress through all calculations, the UBCSAND model defines the plastic shear modulus in a normalized manner. For example, the initial plastic shear modulus (G_i^P) at small strains is defined by dividing the small-strain shear modulus from Equation 3.2.1 by the mean effective stress, as follows:

$$G_i^P = k_G^e \times \left(\frac{\sigma'_m}{P_a}\right)^{n_e - 1} \tag{3.2.2}$$

Accordingly, G_i has the same units as the shear stress while G_i^p is dimensionless. When shear stresses increase, the normalized tangent slope of the plastic response can be predicted the derivative of the hyperbolic curve, as follows:

$$G_p = G_i^P \times \left[1 - \frac{\tau}{\tau_f} R_f\right]^{0.5} \tag{3.2.3}$$

This equation indicates that the normalized plastic shear modulus is a function of the mean stress, the shear stress at failure (τ_f), and the failure ratio (R_f).

The incremental change in the developed stress ratio can be computed as the derivative of the hyperbolic stress-strain curve shown in Figure 3.6 as follows:

$$\eta_d = \frac{\tau}{\sigma'_m} = sin\phi_d \tag{3.2.4}$$

$$\Delta\eta_d = \left[\frac{\Delta\tau}{\sigma'_m} - \left(\frac{\tau}{(\sigma'_m)^2}\right)\Delta\sigma'_m\right] \tag{3.2.5}$$

where ϕ_d is the developed friction angle.

In general, due to the nonlinear shape of the hyperbolic stress strain curve, any shear strains generated during loading or reloading are be considered plastic shear strains. The plastic shear response is captured assuming a hyperbolic relationship between the incremental changes in the plastic shear strains ($\Delta\gamma^p$) and the developed stress ratio ($\Delta\eta_d = \Delta\tau/\sigma'_m$). The plastic shear strains can be computed using the change in the developed stress ratio and the plastic shear modulus.

$$\Delta\gamma^p = \Delta\eta_d \left(\frac{1}{G^p}\right) \tag{3.2.6}$$

UBCSAND uses a flow rule developed from energy considerations to compute the coupling between the plastic shear strain and the plastic volumetric strain response, as follows:

$$\Delta\varepsilon_v{}^p = \Delta\gamma^p(\sin\phi_{cv} - \eta_d) \tag{3.2.7}$$

where (ϕ_{cv}) is the constant volume friction angle (Puebla et al. 1997). Additional derivations related to the flow rule are presented in Appendix A.2. Plastic volumetric strains in loose sands are contractive and are influenced by the evolution of the developed stress ratio. In dense sands, the plastic volumetric strains are dilative (Puebla et al. 1997). Lateral constraint during the applied shear strain in a cyclic simple shear test indicates that the plastic volumetric strain will be due solely to vertical axial strains (e.g., no radial strains).

An important aspect of this model is that the cumulative volumetric strain only accrues during loading/reloading and not during unloading because loading/reloading is a plastic response causing permanent deformations whereas unloading is assumed to be elastic leading to no permanent deformation of the soil structure. Unloading is defined as the case when the shear stress is reduced from a value of $\tau = \tau_c$ until $\tau = 0$. The schematic in Figure 3.7 shows the development of plastic shear and volumetric strains during loading/reloading (labeled in red) and elastic unloading (labeled in green). Elastic changes in volumetric strain are only expected if there are changes in mean effective stress, so during elastic unloading (labeled in green), no volumetric strains will occur. To calculate the cumulative plastic volumetric strain (ε_v^P), the increment of plastic volumetric strain during each cycle ($\Delta\varepsilon_v^p$) is added to the plastic volumetric strain from the previous cycle (ε_{vo}^p):

$$\varepsilon_v^P = \Delta\varepsilon_v^p + \varepsilon_{vo}^p \tag{3.2.8}$$

The cumulative plastic volumetric strain in percent is:

$$\varepsilon_v^P(\%) = \varepsilon_v^p(100\%) \tag{3.2.9}$$

The total volumetric strain ε_v^T is equal to the sum of the plastic volumetric strain and the elastic volumetric strain, where the elastic volumetric strain is directly proportional to the mean effective stress through the bulk modulus of the soil (which can be estimated from the shear modulus and Poisson's ratio). However, it can be assumed that the elastic volumetric strain in a cyclic simple shear test on an unsaturated sand in the funicular regime is approximately equal to zero as the changes in mean effective stress are not expected to be significant. While Rong and McCartney (2020b) did observe changes in mean effective stress, these changes were within 10% of the mean total stress applied in the experiments.

3.3 ESTIMATION OF CHANGES IN PORE AIR PRESSURE DURING UNDRAINED SHEARING

A major difference in the presented model compared to UBCSAND is that the air and water pressures are assumed to increase at different rates (surface tension not ignored) whereas UBCSAND assumes the pressures are increasing at constant rates by implementing a bulk stiffness to account for both pressures simultaneously (Seid-Karbasi and Byrne 2006). To account for surface tension, separate equations are derived for air and water pressure generation. The instantaneous bulk modulus of air is assumed to be initially at atmospheric conditions and increase incrementally during undrained cyclic simple shearing. The degrees of saturations considered in this study are in the funicular regime and the pore air voids are assumed to be continuous and connected. Some voids may be water filled, air filled or have partial air and water menisci. To extend the hyperbolic model to include a poromechanical approach, it is assumed that all volumetric strains correspond to a reduction in air volume and particle due to the incompressibility of undrained water and the assumption that no particle crushing occurs to the soil. Air is assumed to be an ideal gas and the temperature of the air-water-soil system is at ambient temperature

conditions (T = 294 K) with no fluctuation. Incorporating volumetric definitions of the soil's 3-phase diagram into the equations of the Ideal Gas Law, and Henry's Law, allows for a derivation to find the pore air pressure change corresponding to a volume change during undrained cyclic simple shearing (derivation in Appendix A.3). The relationship between pore air pressure and volumetric strain for a given initial degree of saturation and initial void ratio can be defined as follows:

$$u_a = \frac{\left(P_{atm}\varepsilon_v^p\,(1+e_o)\right)}{\left(hS_o e_o RT + e_o(1-S_o) - \varepsilon_v^p\,(1+e_o)\right)} \tag{3.3.1}$$

This pore air pressure equation is an isothermal equation that is comprised of constant values (initial void ratio, initial degree of saturation, Henry's constant, and temperature) and the plastic volumetric strain that will evolve during cyclic shearing. The study of Youd (1971) indicates that all soils are expected to have compressive plastic volumetric strains occurring during cyclic simple shearing, which implies that that air pressure calculated from Equation 3.3.1 will increase during a cyclic simple shear test. Further, the pressurization of the pore air during cyclic simple shearing is expected to affect the seismic compression in unsaturated sands during earthquakes by leading to a decrease in the mean effective stress according to Equation 2.2.2.

3.4 CHANGES IN DEGREE OF SATURATION DURING UNDRAINED SHEARING

It is assumed that there will be no change between the initial and final volume of water in an undrained specimen during cyclic simple shearing due to the high bulk modulus of water. Saturation is the ratio between water volume and void volume (i.e., void volume is comprised of the total water volume and air volume), therefore the change in saturation due to plastic volumetric strain (seismic compression) is linked to the volume change of the pore air voids. By incorporating the pore air volume change in terms of the plastic volumetric strain and initial void ratio, the following relationship for saturation change during cyclic simple shearing can be defined where the volume of solids V_s is assumed to equal 1 (derivation in Appendix A.4):

$$S = \frac{V_s e_o S_o}{e_o - (V_s + e_o)\varepsilon_v^p} \tag{3.4.1}$$

As the volume of solids, the initial void ratio, and initial degree of saturation are constants, the form of Equation 3.4.1 indicates that the degree of saturation is inversely related to changes in the plastic volumetric strain.

3.5 ESTIMATION OF CHANGES IN PORE WATER PRESSURE DURING UNDRAINED SHEARING

The application of the UBCSAND model to unsaturated soils by Seid-Karbasi and Byrne (2006, 2007) and Byrne et al. (2006) assumed that the changes in pore water pressure are equal to the

changes in pore air pressure during undrained cyclic shearing of unsaturated soil for simplicity. However, several experimental studies (Unno et al. 2009; Rong and McCartney 2020b) found that the pore air and water pressures evolved in different manners during undrained cyclic shearing. The approach followed in this study was to estimate the changes in matric suction from the changes in degree of saturation predicted from Equation 3.4.1, then to use the definition of the matric suction to calculate the pore water pressure from the pore air pressure calculated in Equation 3.2.9. Specifically, the pore water pressure can be calculated from the pore air pressure and matric suction as follows:

$$u_w = u_a - \psi \tag{3.5.1}$$

Use of this equation implies that the water retention in the soil is due primarily to capillarity (Lu and Likos 2004). It is assumed that the thermodynamic state of the soil is constant throughout the duration of cyclic simple shearing as surface tension and capillarity are affected by temperature.

During undrained cyclic shearing, Rong and McCartney (2020b) found that unsaturated sand specimens initially on the primary drying path of the SWRC followed a wetting transient SWRC scanning path having a slope that depended on the initial degree of saturation of the specimens. Using the relationship between degree of saturation and matric suction, a semi-empirical equation is derived from the soil's SWRC. To predict the changes in the model's matric suction, a log-linear relationship between the saturation and matric suction was defined empirically as follows (derivation in Appendix A.5):

$$\psi = 10^{\frac{S-(S_0+m\log_{10}\psi_0)}{-m}} \tag{3.5.2}$$

This equation is only valid for initial degrees of saturation in the funicular regime as shown in Figure 3.8. For greater degrees of saturation, a reconsolidation analysis using pore water pressures predicted using the model of Seid-Karbasi and Byrne (2004) is necessary. This is a topic for a future study. Using the model's prediction of matric suction from Equation (3.5.1) and the pore air pressure from Equation 3.2.9, the pore water pressure can be computed.

3.6 CALCULATION OF EFFECTIVE STRESS CHANGES DURING CYCLIC SHEARING

Once the air pressure, saturation and matric suction changes are predicted, the incremental effective stress can now be computed using Lu et al. (2010) equation for effective stress, given as follows using the effective saturation as the effective stress parameter:

$$\sigma'_v = (\sigma_v - u_a) + S_e\psi \tag{3.6.1}$$

where, the values of u_a, S_e, and ψ are calculated during the process of seismic compression using Equations 3.3.1, 3.4.1, and 3.5.2. Since the cyclic simple shear test is confined to a cylindrical specimen that does not deform radially (no bulging sides) during shearing, K_o conditions are valid, and the K_o coefficient can be calculated using elasticity, as follow:

$$K_o = \frac{\upsilon}{1-\upsilon} \tag{3.6.2}$$

where ν is the Poisson's ratio. The applied vertical effective stress in the cyclic simple shear test can then be converted to mean effective stress using K_o, as follows:

$$\sigma'_m = \left(\frac{1+2K_o}{3}\right)\sigma'_v \tag{3.6.3}$$

3.7 PREDICTING THE EVOLUTION IN HYDRO-MECHANICAL VARIABLES DURING UNDRAINED SHEARING

The prediction of the volumetric strain during undrained cyclic shearing is closely related to the plastic shear modulus, which is sensitive to the mean effective stress as described in Section 3.2. Accordingly, the values of σ_m' calculated during application of the cyclic shear strains in the hysteretic stress-strain curve equations are used to calculate the shear modulus that affect the evolution in cyclic shear stress. A flow chart of the sequence of the model is shown in Figure 3.9.

CHAPTER 3: FIGURES

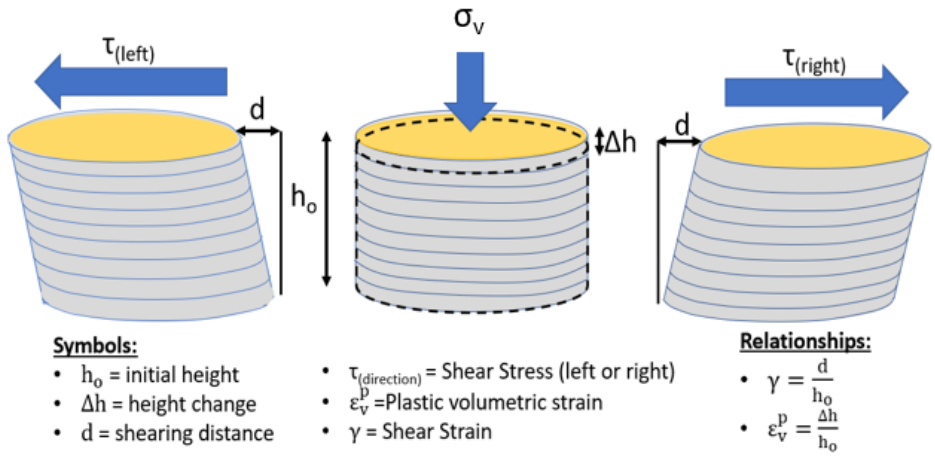

Figure 3.1 Key variables in a cyclic simple shear test on a soil specimen after vertical loading and during bi-directional cyclic simple shearing.

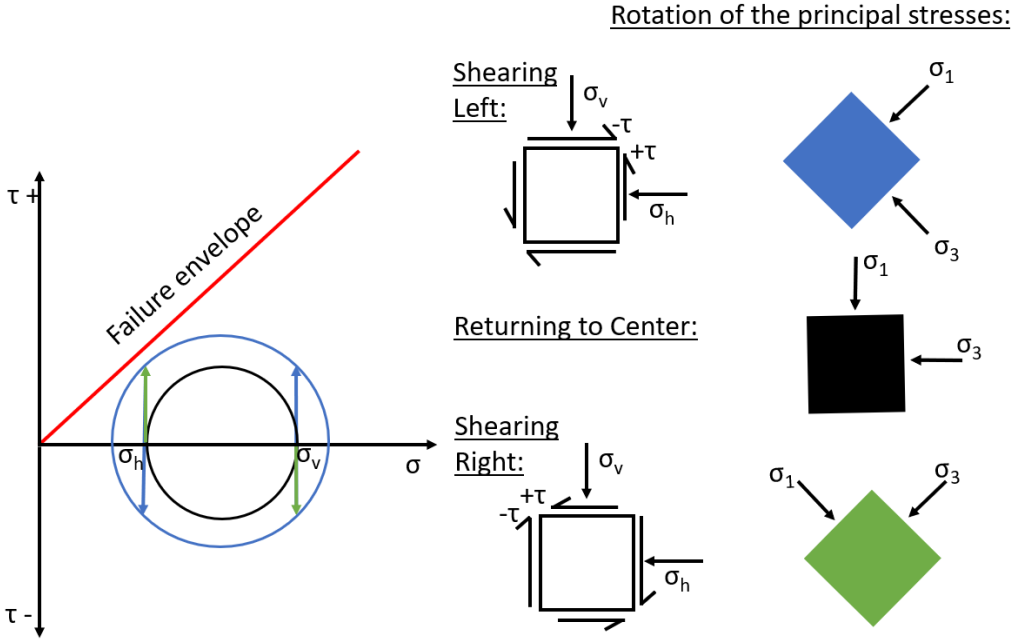

Figure 3.2 Schematic of the changes in stress state during cyclic simple shear testing of a soil specimen showing the directions of the stresses during applied shear strain testing.

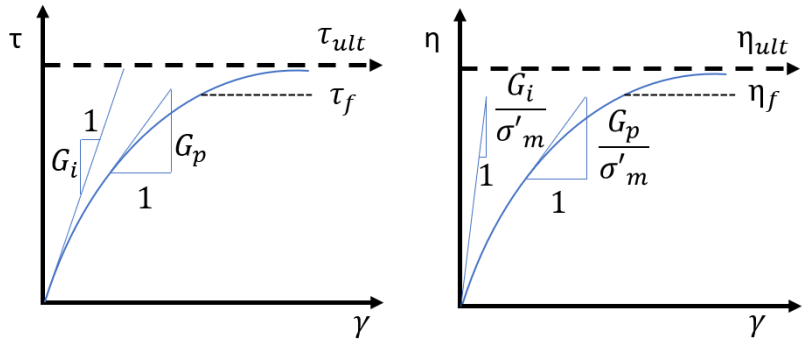

Figure 3.3 Backbone curve shape from the hyperbolic model: (a) Shear stress-strain curve; (b) Shear stress ratio-shear strain curve.

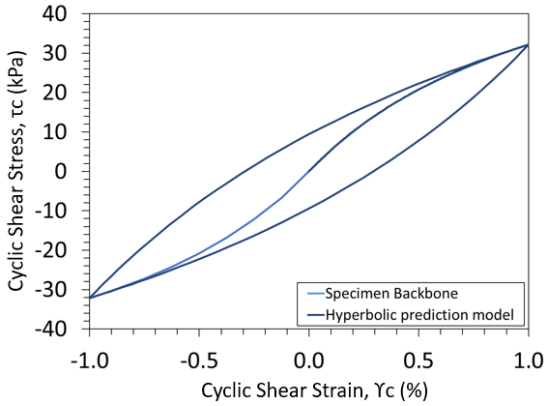

Figure 3.4 Hysteretic loop showing the hyperbolic shear stress strain reversals along with the hyperbolic backbone curve.

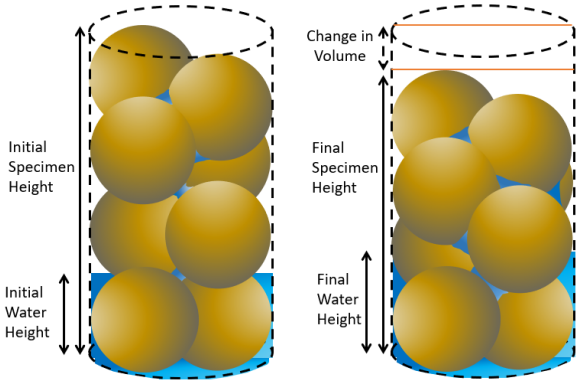

Figure 3.5 Schematic of soil particle rearrangement before and after cyclic shearing showing initial and final heights of specimen and changes in degree of saturation.

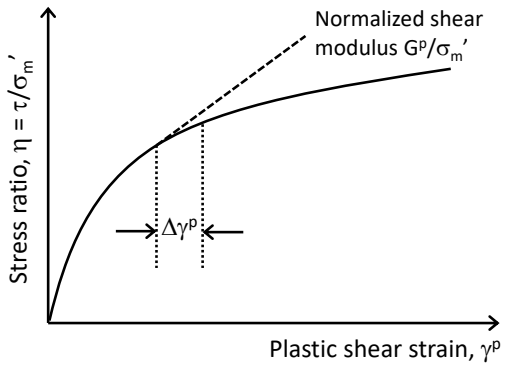

Figure 3.6 Schematic of the hyperbolic stress-strain relationship used in UBCSAND

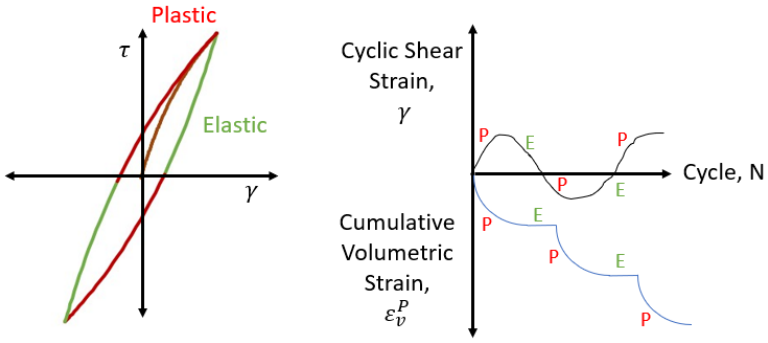

Figure 3.7 Hysteretic shear stress-shear strain showing plastic load/reload and elastic unload, with the corresponding plastic/elastic cyclic shear strain and cumulative plastic volumetric strain.

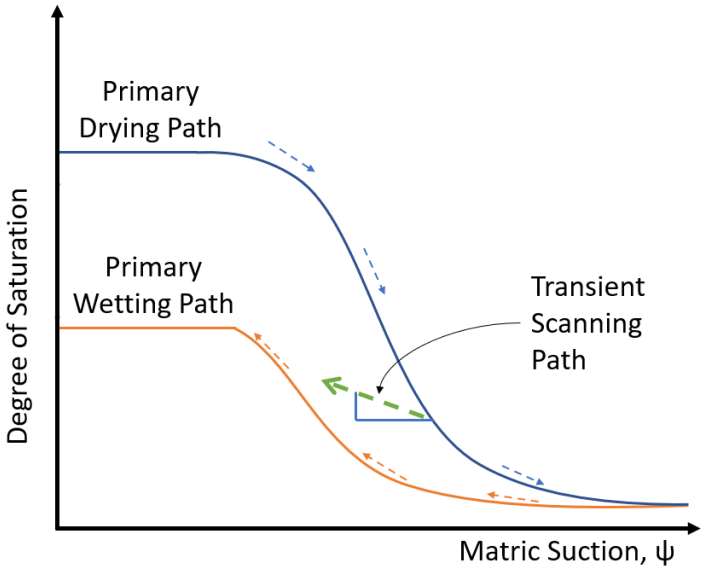

Figure 3.8 Schematic of the transient scanning path of the SWRC for a sand specimen initially on the primary drying path.

*Establish model relationships:

- $G_i = k_G^e * P_a * \left(\frac{\sigma'_m}{P_a}\right)^{n_e}$
- $G_i^P = k_G^e * \left(\frac{\sigma'_m}{P_a}\right)^{n_e - 1}$
- $G^P = G_i^P * \left[1 - \frac{\tau}{\tau_f} R_f\right]^{.5}$

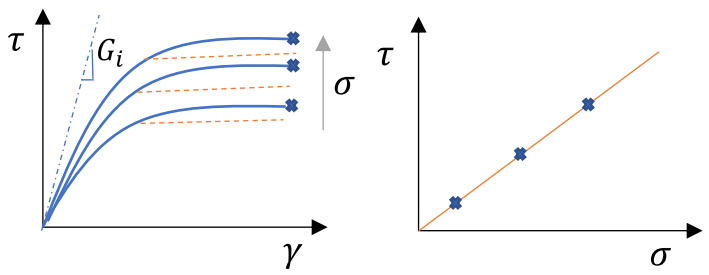

*Use Hysteretic Shear Stress-Strain Equations to establish τ from input strain history:

- γ_c at $f = 1\text{Hz}$ For N cycles
- As $\gamma_e << \gamma_p$ neglect, $\gamma = \gamma_p$
- During simple shear: $\Delta\sigma'_m \approx 0$, $\varepsilon_{ve} \approx 0$

Hysteretic Equations:

$$\tau_+ = \left(\frac{\gamma_c + \gamma_{applied}}{\frac{1}{G_i} + \frac{(\gamma_c + \gamma_{applied}) * R_f}{2 * \tau_{ult}}}\right) - \tau_c$$

$$\tau_- = \left(\frac{\gamma_c - \gamma_{applied}}{\frac{1}{G_i} + \frac{(\gamma_c - \gamma_{applied}) * R_f}{2 * \tau_{ult}}}\right) + \tau_c$$

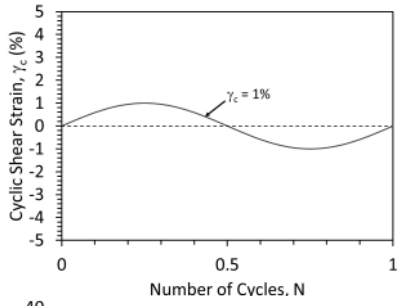

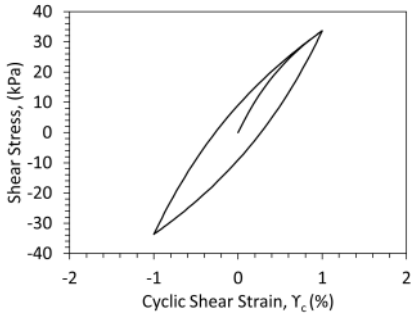

*Use τ to calculate G_p

*Use G_p to calculate γ_p (only on load/reload)

* Use γ_p to calculate ε_v^p

* Use ε_v^p to calculate u_a and S

* Use S and SWRC transient curve to calculate ψ

* Use S, ψ, u_a to calculate σ_m' for next cycle

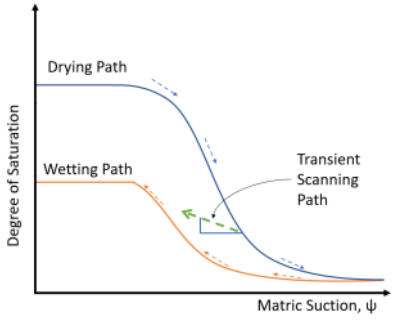

Figure 3.9 Flow chart for the semi-empirical hyperbolic model with hydro-mechanical coupling for seismic compression in the funicular regime.

4 DATA

4.1 SAND SPECIMENS IN CYCLIC SIMPLE SHEAR DATABASE

A single sand was used to form the experimental database of cyclic simple shear test results developed by Rong and McCartney (2019, 2020a, 2020b, 2020c, 2021a, 2021b). The sand is classified as a well-graded sand (SW) according to the Unified Soil Classification System (USCS). The sand has a mean particle diameter (D_{50}) and an effective particle diameter (D_{10}) of 0.8 and 0.2 mm, respectively. The sand is reported to have a coefficient of uniformity (C_u) and curvature (C_c) of 6.1 and 1.0, respectively. The maximum and minimum void ratios are 0.853 and 0.371, respectively. The particle size distribution curve for the SW sand is shown in Figure 4.1.

To prepare the specimens for cyclic simple shear tests, the sand was funneled into the specimen housing to reach a target relative density of 0.45 without tamping. The initial relative density was used in all of the tests of the database, except for those performed by Rong and McCartney (2021b), who investigated the effect of initial relative density in drained cyclic simple shear tests. The primary wetting and drying path of the SWRC of the sand having an initial relative density of 0.45 were obtained using the hanging column approach, and the data points fitted with the van Genuchten (1980) SWRC model as shown in Figure 4.2 (Rong and McCartney 2020b).

The experimental approach used to perform the cyclic simple shear test was reported by Rong and McCartney (2021b). Rong and McCartney (2021a) used the hanging column technique similar to the approach used by Tatsuoka et al. (1979) to desaturate initially saturated sand specimens in the cyclic simple shear device to reach different initial degrees of saturation in the funicular regime of the SWRC. During initial application of a target suction, the water outflow was tracked using the hanging column and the pore water pressure was monitored using a tensiometer until the target matric suction was reached and held for approximately 30 minutes, at which point the specimen is assumed to be at hydraulic equilibrium and ready for cyclic simple shearing. The cyclic simple shear tests reported by Rong and McCartney (2019, 2020a, 2020b, 2020c, 2021a, 2021b) were performed in a cyclic simple shear apparatus that has a wire-reinforced membrane that does not permit radial expansion and therefore the volumetric strain during shearing can be measured by the changes in the height of the cylindrical specimen. A schematic of the specimen housing used in the cyclic simple shear device is shown in Figure 4.3. Rong and McCartney (2021a) developed this cyclic simple shear device by modifying an NGI simple shear device to perform cyclic tests, and by incorporating a special bottom platen which transmits water from a hanging column for initial suction application and to maintain the suction during drained tests. The bottom platen also has a port to accommodate a tensiometer for measurement of the pore water pressure. They also included a pressure sensor to measure the pore air pressure at the top of the specimen during undrained tests. The cylindrical sand specimens tested by Rong and McCartney (2020a, 2020b, 2020c, 2021a, 2021b) had a height of approximately 20 mm and a diameter of 66.7 mm. The resulting height to diameter ratio was 0.3 which was less than the maximum value of 0.4 defined

by ASTM D6528. All specimens regardless of drainage conditions were subjected to an applied vertical stress of 50 kPa to recreate loading conditions of a transportation design backfill during seismic shaking.

Rong and McCartney (2019, 2020a, 2021a, 2021b) reported the results from drained cyclic shearing tests having a range of different applied shear strain amplitudes (0.3, 1.0, 5, 10) for 200 to 1000 cycles. Rong and McCartney (2020b, 2020c, 2021a) reported the results from undrained cyclic shearing tests applied shear strain of 1% at a strain rate of 0.83 %/min for a duration of 200 cycles. The drained tests were useful to define the backbone curve as they were performed to higher shear strain amplitudes, but this study is primarily focused on the seismic compression during undrained shearing. Accordingly, this report only presents selected drained tests from Rong and McCartney (2020a) are reported while several undrained tests from Rong and McCartney (2020b, 2021a) are reported along with additional unreported tests.

4.2 DRAINED MONOTONIC SIMPLE SHEAR DATA

The testing protocol for the fully drained experimental data was kept at a constant matric suction, valves on top/bottom of housing were left open and the ventilation permitted air flow thereby reflecting the pore air pressures at atmospheric conditions. As cyclic shearing was applied to the specimen, volumetric contraction commenced which induced the outflow of water. Shearing during the experiment was reported by Rong and McCartney (2020b) to be considered slow enough to allow for the dissipation of any generated excess pore water pressure. Several drained data sets were collected at constant matric suctions: 4 kPa, 6 kPa and 10 kPa. Drained shearing tests with a constant suction of 4 kPa with cyclic shear strain amplitudes of 1% and 3% strain were used in the calibration of the backbone curve parameters, and the results shown in Figure 4.4 indicate that the shear-stress strain curves from the other tests were generally in good agreement. It should be noted that even when extrapolating this curve to 5% shear strain, the specimen had still not reached failure, which is expected to occur at a shear stress of approximately 63-65 kPa for these unsaturated conditions based on the shear strength parameters reported by Zheng et al. (2019). The initial conditions for the drained specimens are summarized in Table 4.1.

4.3 UNDRAINED CYCLIC SIMPLE SHEAR DATA

The testing protocol for the undrained experimental data had a gauge air pressure transducer attached to the top of the housing platen which blocked air ventilation and allowed for the pore air pressure to be measured during shearing. Once the sand specimen reached its target matric suction, the bottom housing valve was closed to water flow which caused excess pore water pressures to increase during shearing. The initial conditions for the undrained experimental data sets are summarized in Table 4.2, and the measurements from the experiments presented as a function of the cycles of shearing are shown in Figures 4.5 to 4.16. Two tests were performed at each of the initial conditions. A summary of the initial conditions within the funicular regime of the SWRC that were modeled in this study is shown in Table 4.3.

CHAPTER 4: TABLES

Table 4.1 Summary of initial testing conditions and final shear strain for drained tests.

Specimen No.	Initial Matric Suction ψ_o (kPa)	Initial Saturation S_o	Target Shear Strain Range γ_n (%)	Initial Achieved Shear Strain Range γ_o(%)	Final Achieved Shear Strain Range γ_f (%)
C-3	3.96	0.31	3.00 : (-3.00)	2.75 : (-2.86)	2.71 : (-3.01)
C-2	3.87	0.31	1.00 : (-1.00)	0.98 : (-1.06)	0.91 : (-1.13)
D-3	5.95	0.20	3.00 : (-3.00)	3.01 : (-2.64)	2.99 : (-2.83)
D-2	5.93	0.20	1.00 : (-1.00)	0.94 : (-0.95)	1.58 : (-0.22)
E-3	10.03	0.12	3.00 : (-3.00)	2.89 : (-2.76)	3.24 : (-2.34)
E-2	10.15	0.11	1.00 : (-1.00)	0.74 : (-1.20)	0.77 : (-1.10)

Table 4.2 Summary of initial testing conditions and final shear strain for the undrained cyclic simple shear experiments (after Rong and McCartney 2020b with new data).

Specimen No.	Initial Matric Suction ψ_o (kPa)	Initial Saturation S_o	Target Strain Range γ_{rn} (%)	Initial Achieved Strain Range γ_{ro} (%)	Final Achieved Strain Range γ_{rf} (%)
Set 1	1.99	0.560	1.00 : (-1.00)	0.98 : (-1.00)	0.86 : (-0.95)
Set 2	1.99	0.560	1.00 : (-1.00)	0.94 : (-0.82)	1.19 : (-0.69)
Set 1	2.99	0.400	1.00 : (-1.00)	0.80 : (-0.89)	0.61 : (-1.22)
Set 2	2.99	0.400	1.00 : (-1.00)	0.88 : (-0.81)	0.51 : (-1.16)
Set 1	3.99	0.300	1.00 : (-1.00)	0.85 : (-0.94)	0.68 : (-1.04)
Set 2	3.99	0.300	1.00 : (-1.00)	0.88 : (-0.81)	0.51 : (-1.16)
Set 1*	6.00	0.206	1.00 : (-1.00)	0.89 : (-1.08)	0.83 : (-1.03)
Set 2	5.99	0.206	1.00 : (-1.00)	0.91: (-0.72)	0.87: (-0.82)
Set 1	9.99	0.118	1.00 : (-1.00)	1.10 : (-0.81)	1.03 : (-0.94)
Set 2	10.00	0.117	1.00 : (-1.00)	0.89 : (-1.04)	0.78 : (-1.18)
Set 1*	100.00	0	1.00 : (-1.00)	0.92 : (-1.03)	1.00 : (-0.88)
Set 2*	100.00	0	1.00 : (-1.00)	0.92 : (-0.94)	0.78 : (-1.06)

*Previously unreported data sets

Table 4.3 Summary of initial conditions of undrained cyclic simple shear experiments of Rong and McCartney (2020) that were modeled in this study.

S_o	(unitless)	0.117	0.200	0.300	0.400	0.558
ψ_o	(kPa)	10	6	4	3	2

CHAPTER 4: FIGURES

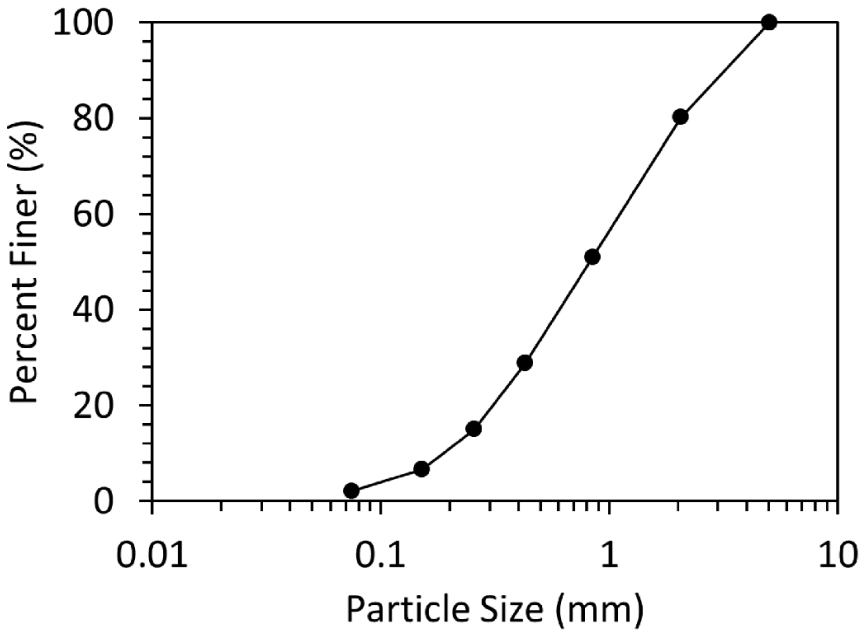

Figure 4.1 Particle size distribution curve for the SW sand.

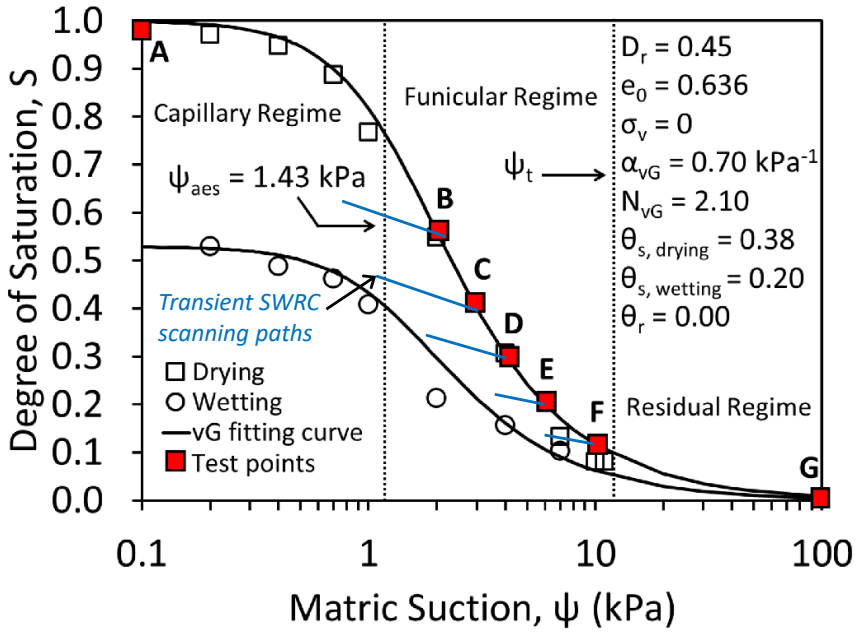

Figure 4.2 Wetting and drying path SWRCs for the sand specimen at D_r = 0.45 with transient scanning paths

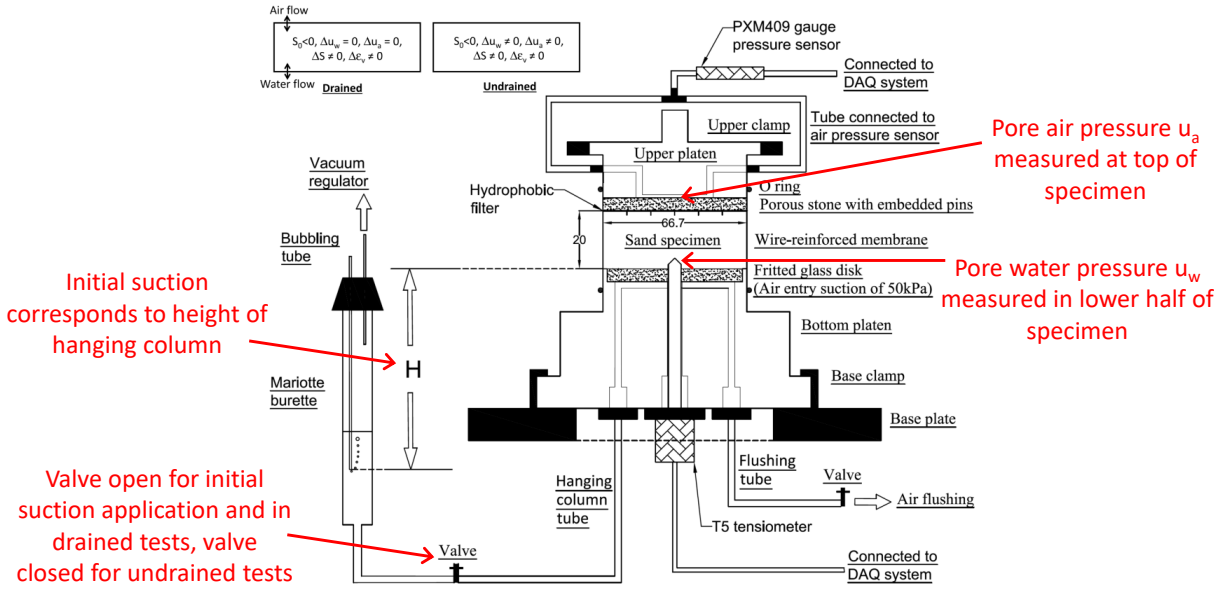

Figure 4.3 Schematic view of the specimen housing in the modified cyclic simple shear device used for drained and undrained experiments on unsaturated soils (dimensions in mm).

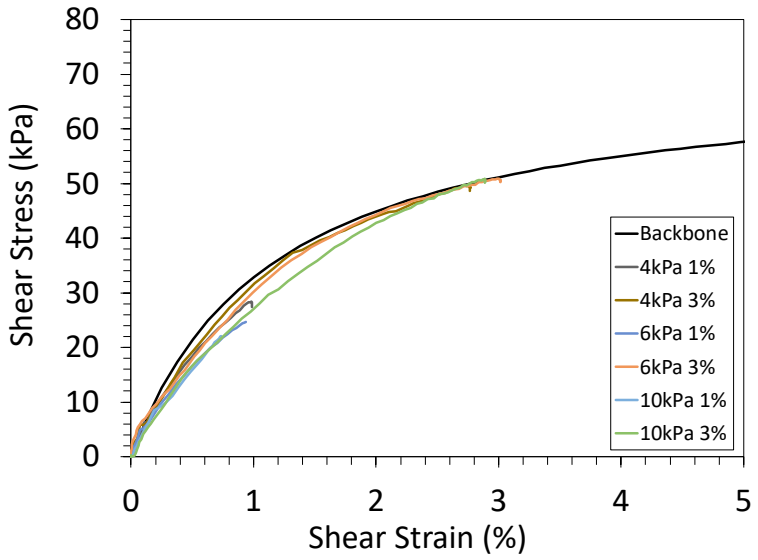

Figure 4.4 Backbone curves for drained sand (D_r = 0.45) at various constant suctions (4 kPa, 6 kPa, 10 kPa) and different shear strain amplitudes (1%, 3%).

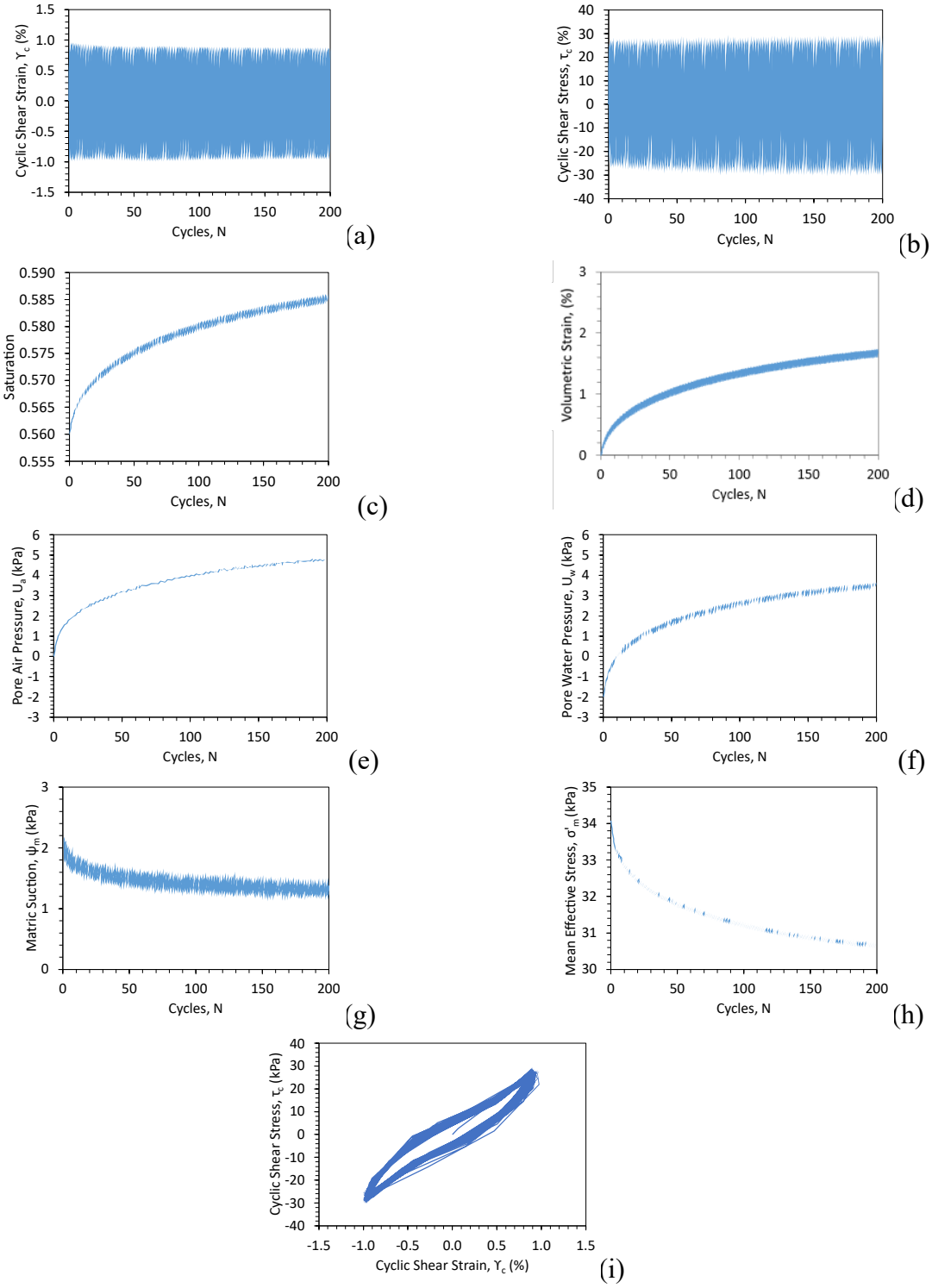

Figure 4.5 Data Set 1 S_0=0.56: (a) Shear strain time series; (b) Shear stress time series (c) Degree of saturation time series; (d) Volume change time series; (e) Pore air pressure change time series; (f) Pore water pressure change time series; (g) Matric suction change time series; (h) Mean effective stress change time series; (i) Cyclic shear stress and cyclic shear strain loops.

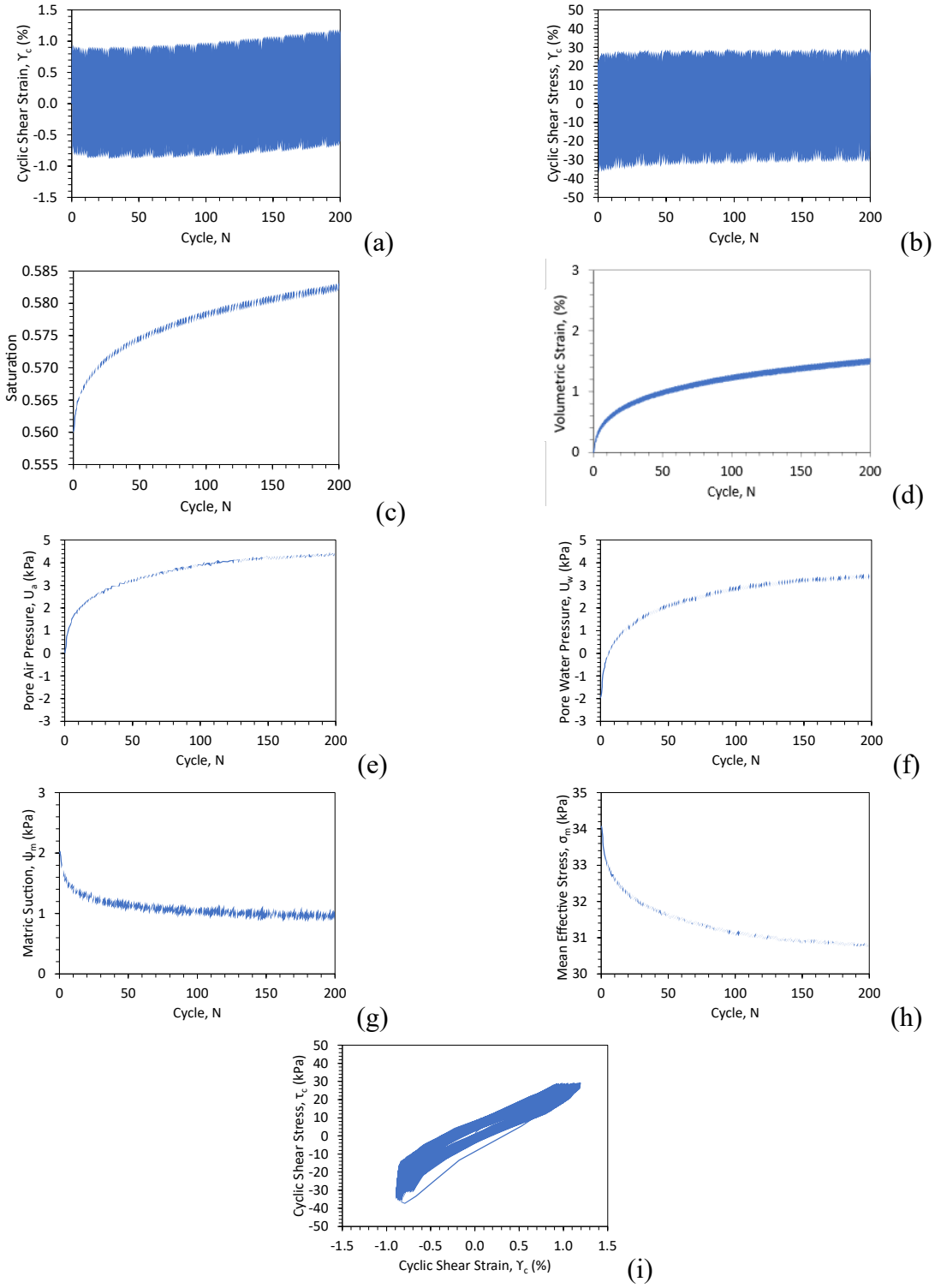

Figure 4.6 Data Set 2 S_0=0.56: (a) Shear strain time series; (b) Shear stress time series (c) Degree of saturation time series; (d) Volume change time series; (e) Pore air pressure change time series; (f) Pore water pressure change time series; (g) Matric suction change time series; (h) Mean effective stress change time series; (i) Cyclic shear stress and cyclic shear strain loops.

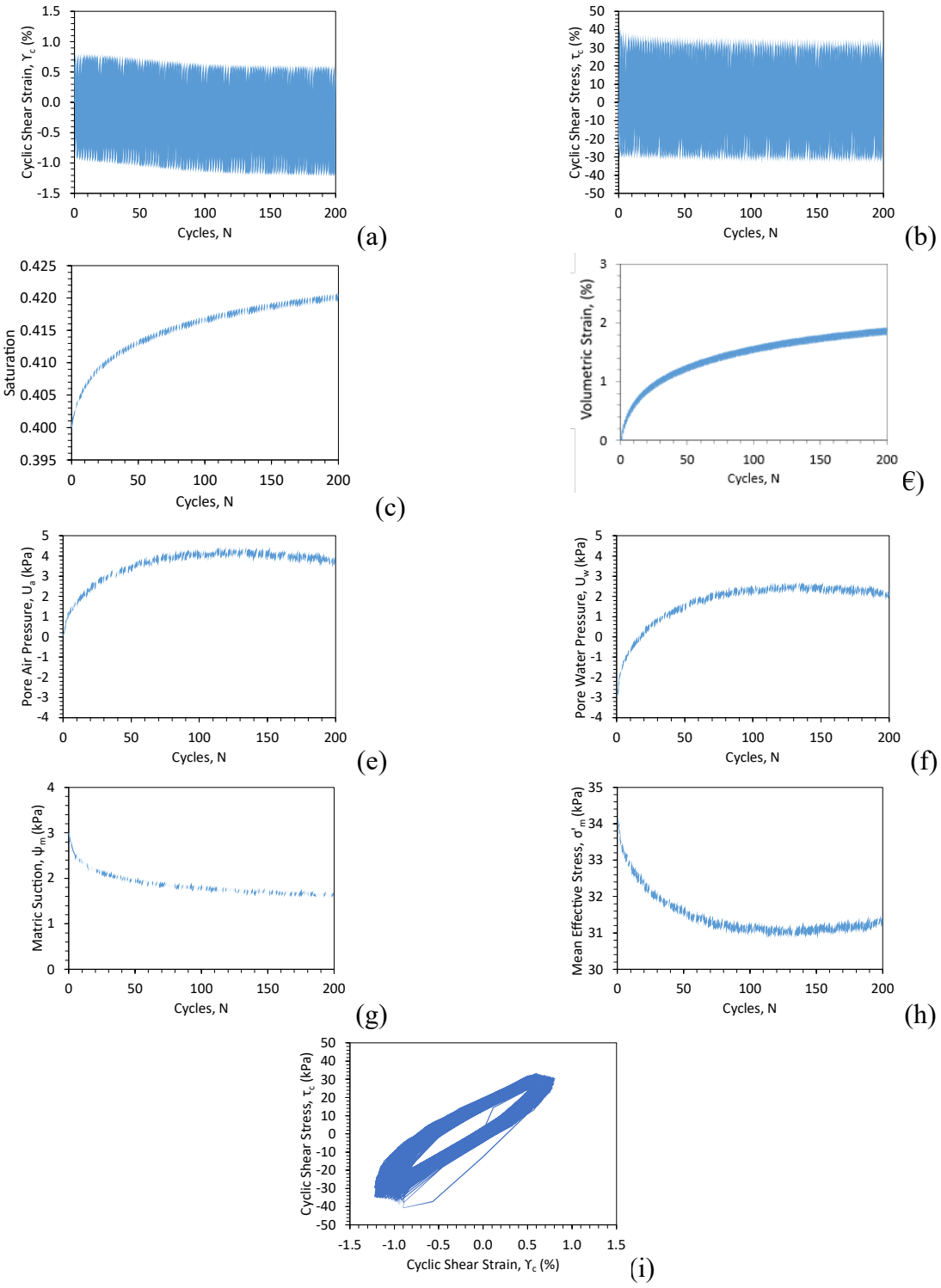

Figure 4.7 Data Set 1 S_0=0.4: (a) Shear strain time series; (b) Shear stress time series (c) Degree of saturation time series; (d) Volume change time series; (e) Pore air pressure change time series; (f) Pore water pressure change time series; (g) Matric suction change time series; (h) Mean effective stress change time series; (i) Cyclic shear stress and cyclic shear strain loops.

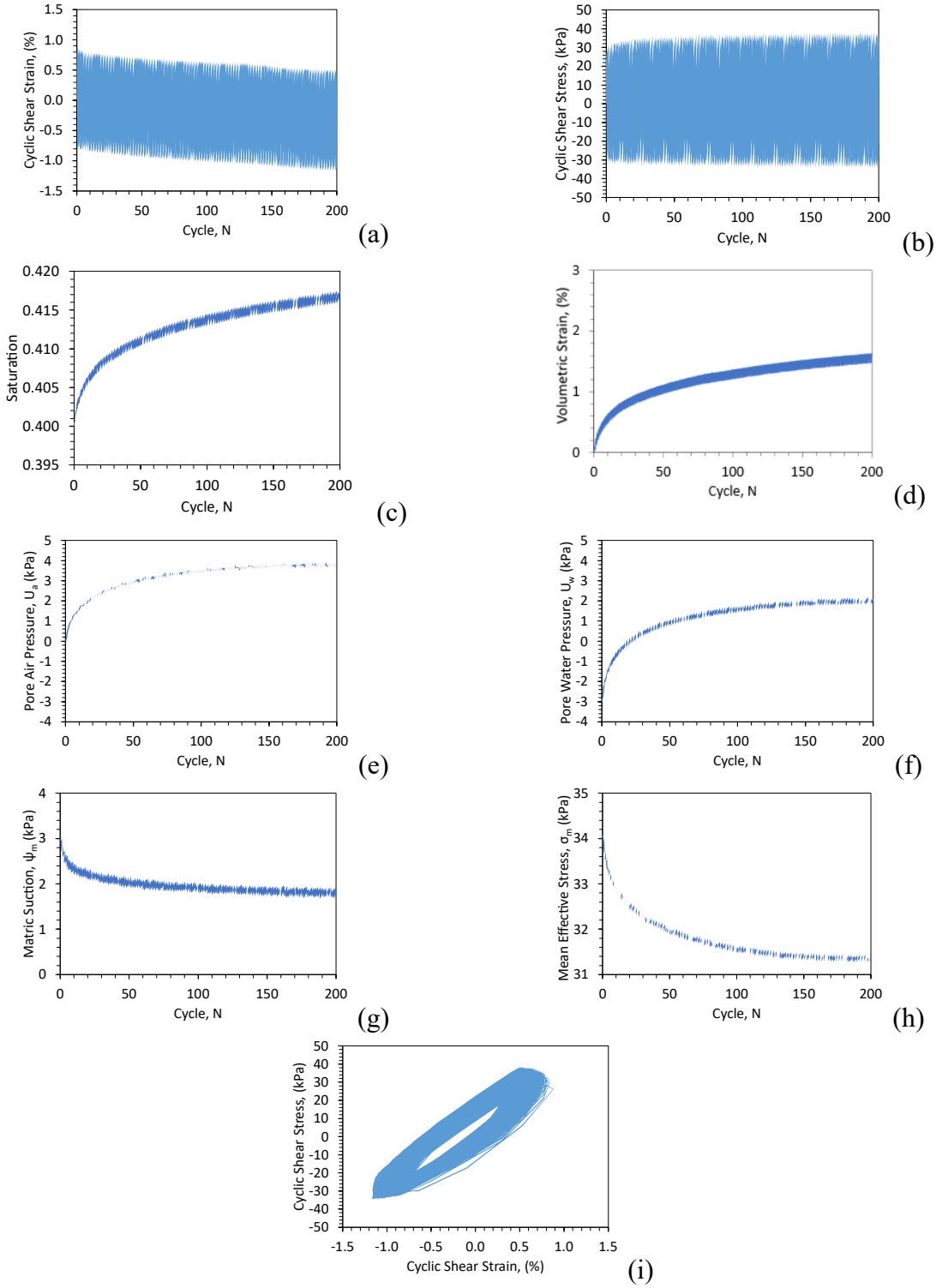

Figure 4.8 Data Set 2 S_0=0.4: (a) Shear strain time series; (b) Shear stress time series (c) Degree of saturation time series; (d) Volume change time series; (e) Pore air pressure change time series; (f) Pore water pressure change time series; (g) Matric suction change time series; (h) Mean effective stress change time series; (i) Cyclic shear stress and cyclic shear strain loops.

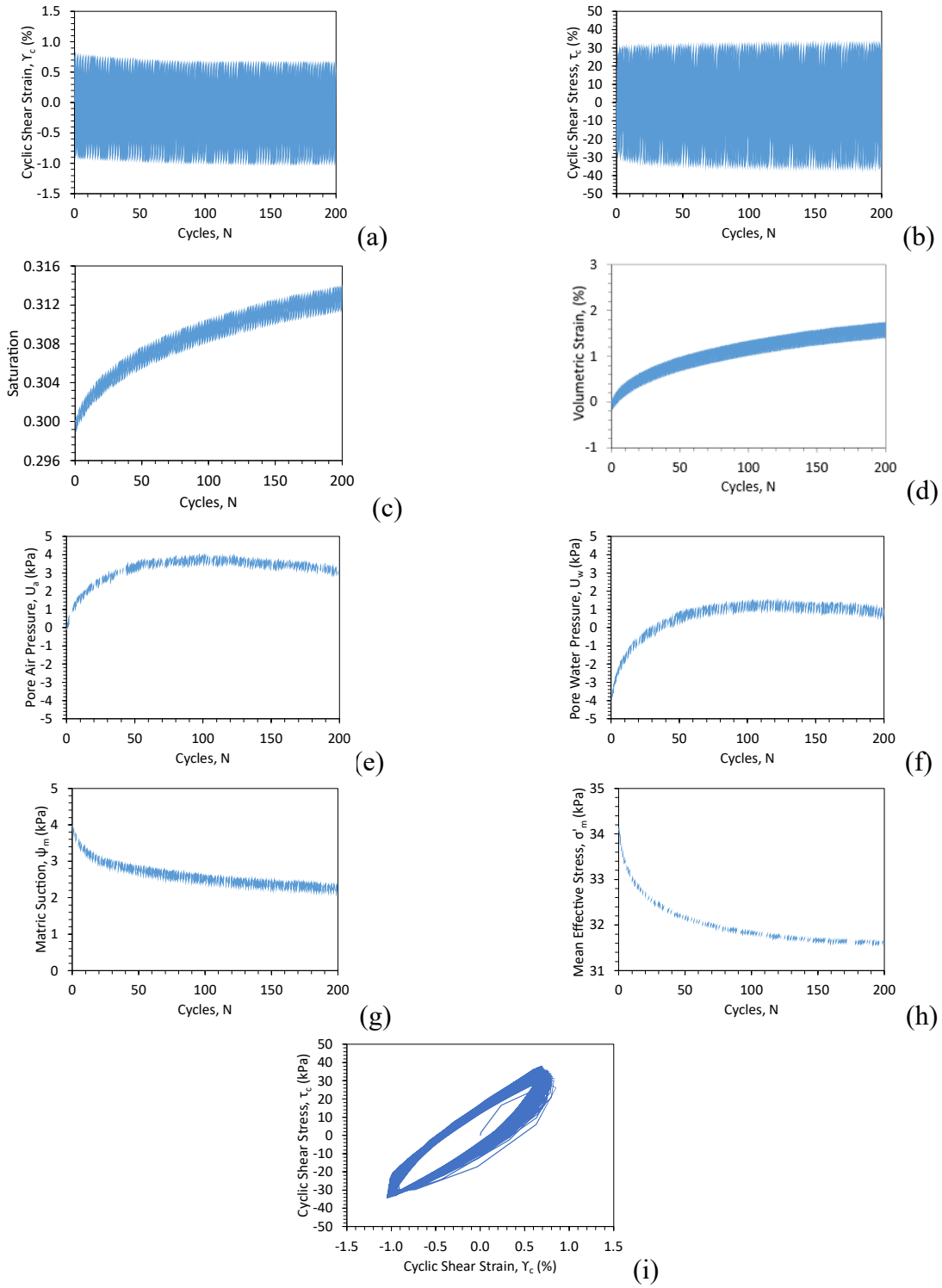

Figure 4.9 Data Set 1 S_0=0.3: (a) Shear strain time series; (b) Shear stress time series (c) Degree of saturation time series; (d) Volume change time series; (e) Pore air pressure change time series; (f) Pore water pressure change time series; (g) Matric suction change time series; (h) Mean effective stress change time series; (i) Cyclic shear stress and cyclic shear strain loops.

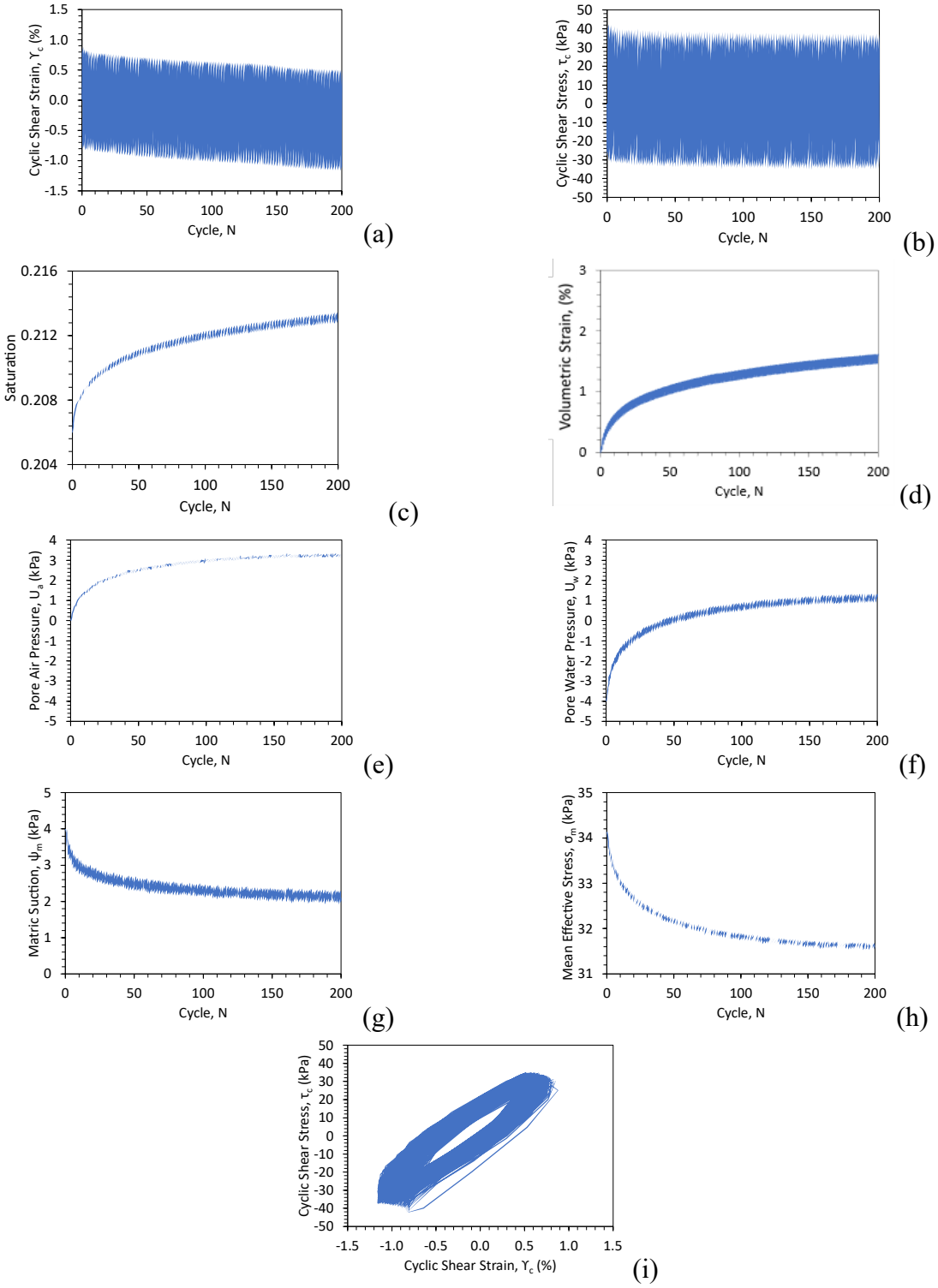

Figure 4.10 Data Set 2 S_0=0.3: (a) Shear strain time series; (b) Shear stress time series (c) Degree of saturation time series; (d) Volume change time series; (e) Pore air pressure change time series; (f) Pore water pressure change time series; (g) Matric suction change time series; (h) Mean effective stress change time series; (i) Cyclic shear stress and cyclic shear strain loops.

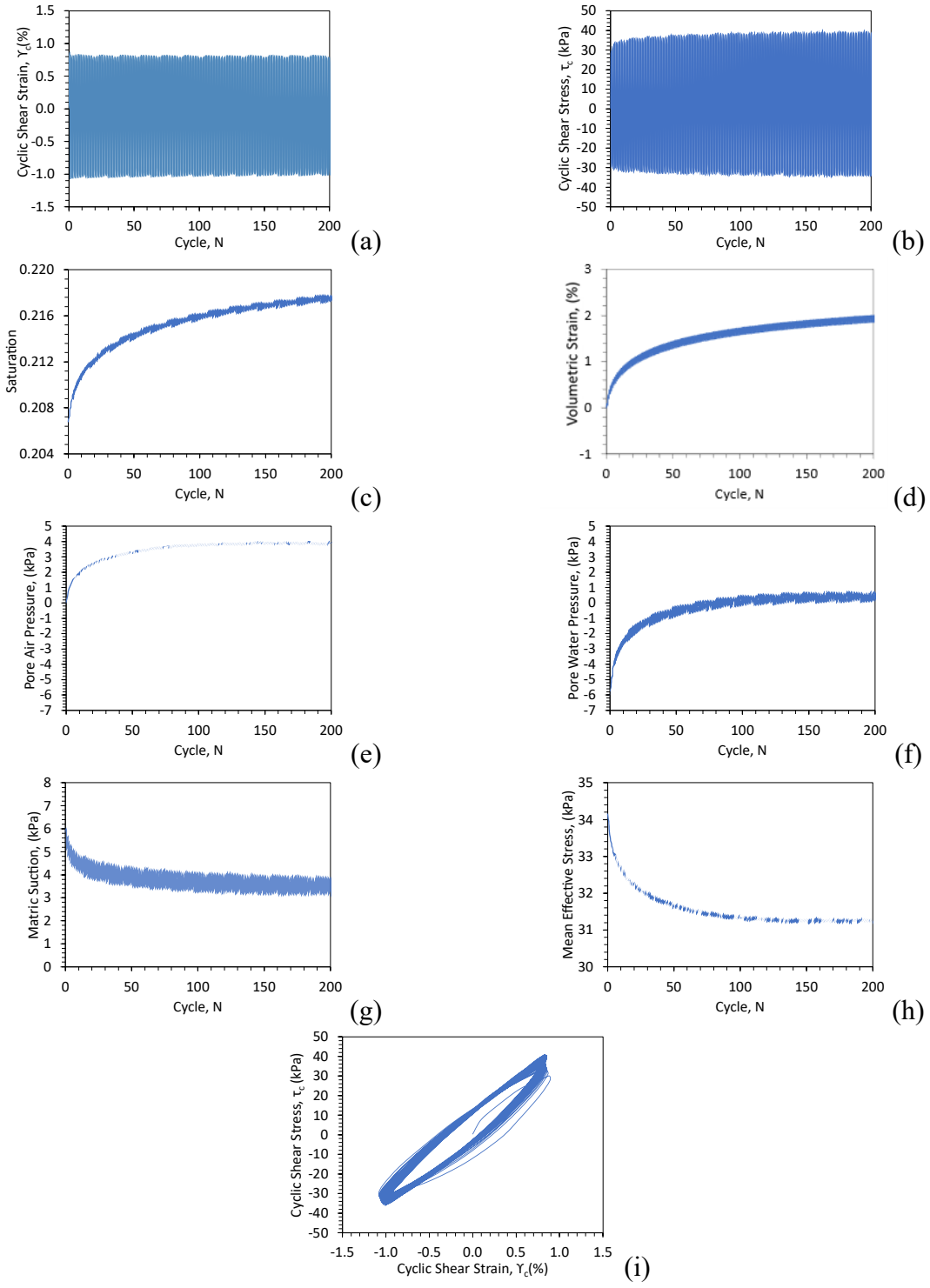

Figure 4.11 Data Set 1* S_0=0.206: (a) Shear strain time series; (b) Shear stress time series (c) Degree of saturation time series; (d) Volume change time series; (e) Pore air pressure change time series; (f) Pore water pressure change time series; (g) Matric suction change time series; (h) Mean effective stress change time series; (i) Cyclic shear stress and cyclic shear strain loops.

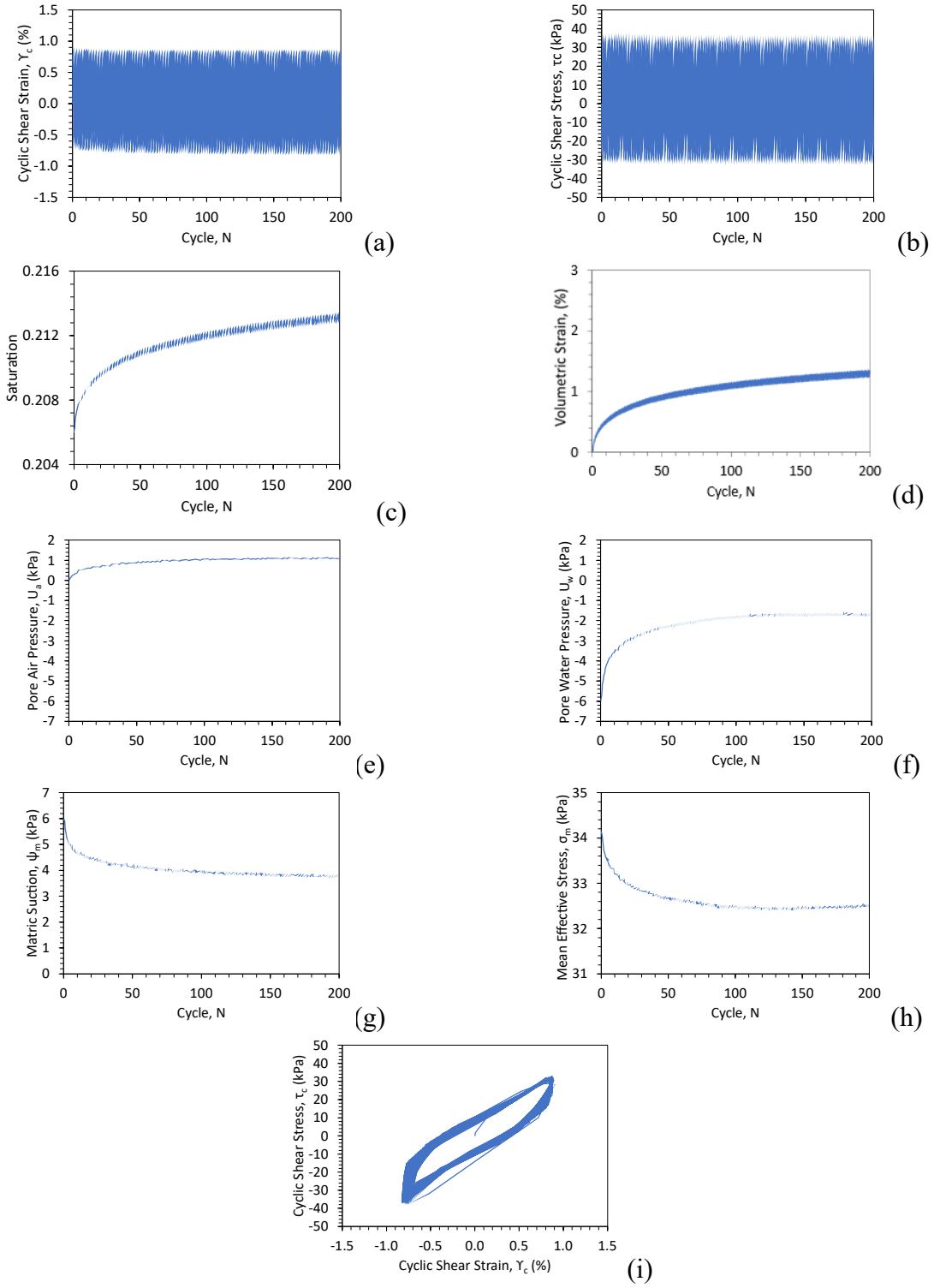

Figure 4.12 Data Set 2 S_0=0.2: (a) Shear strain time series; (b) Shear stress time series (c) Degree of saturation time series; (d) Volume change time series; (e) Pore air pressure change time series; (f) Pore water pressure change time series; (g) Matric suction change time series; (h) Mean effective stress change time series; (i) Cyclic shear stress and cyclic shear strain loops.

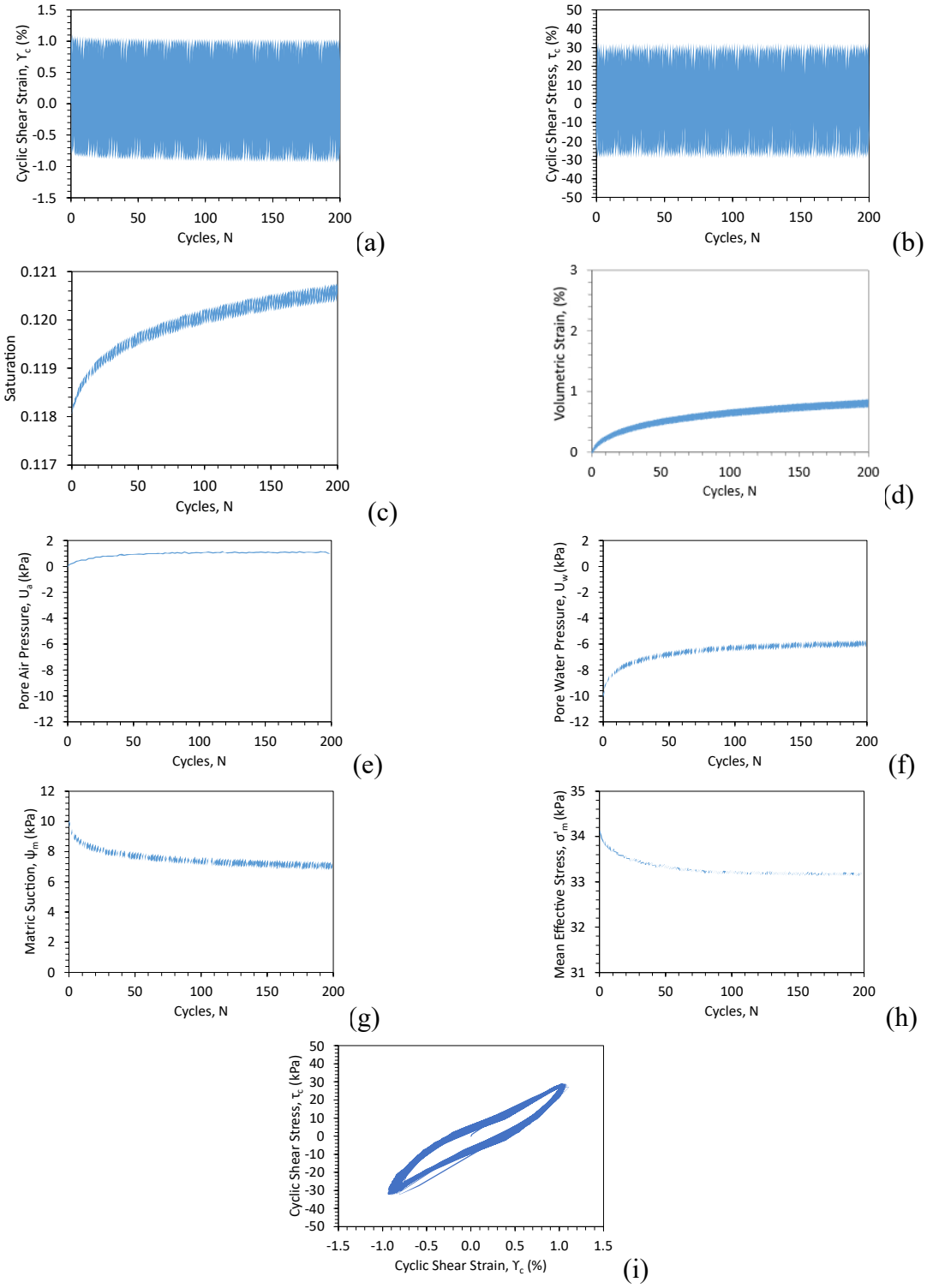

Figure 4.13 Data Set 1 S_0=0.118: (a) Shear strain time series; (b) Shear stress time series (c) Degree of saturation time series; (d) Volume change time series; (e) Pore air pressure change time series; (f) Pore water pressure change time series; (g) Matric suction change time series; (h) Mean effective stress change time series; (i) Cyclic shear stress and cyclic shear strain loops.

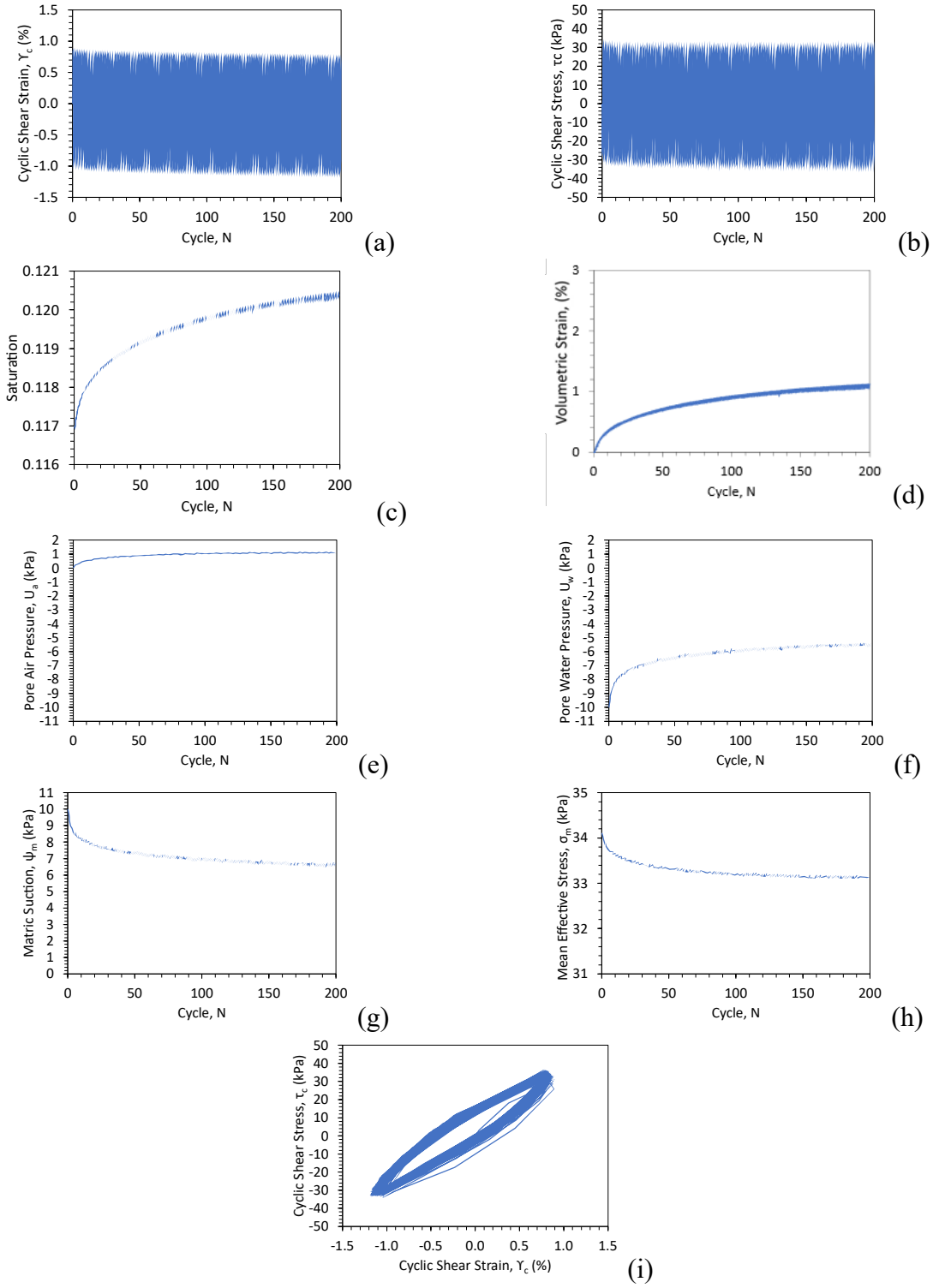

Figure 4.14 Data Set 2 S_0=0.117: (a) Shear strain time series; (b) Shear stress time series (c) Degree of saturation time series; (d) Volume change time series; (e) Pore air pressure change time series; (f) Pore water pressure change time series; (g) Matric suction change time series; (h) Mean effective stress change time series; (i) Cyclic shear stress and cyclic shear strain loops.

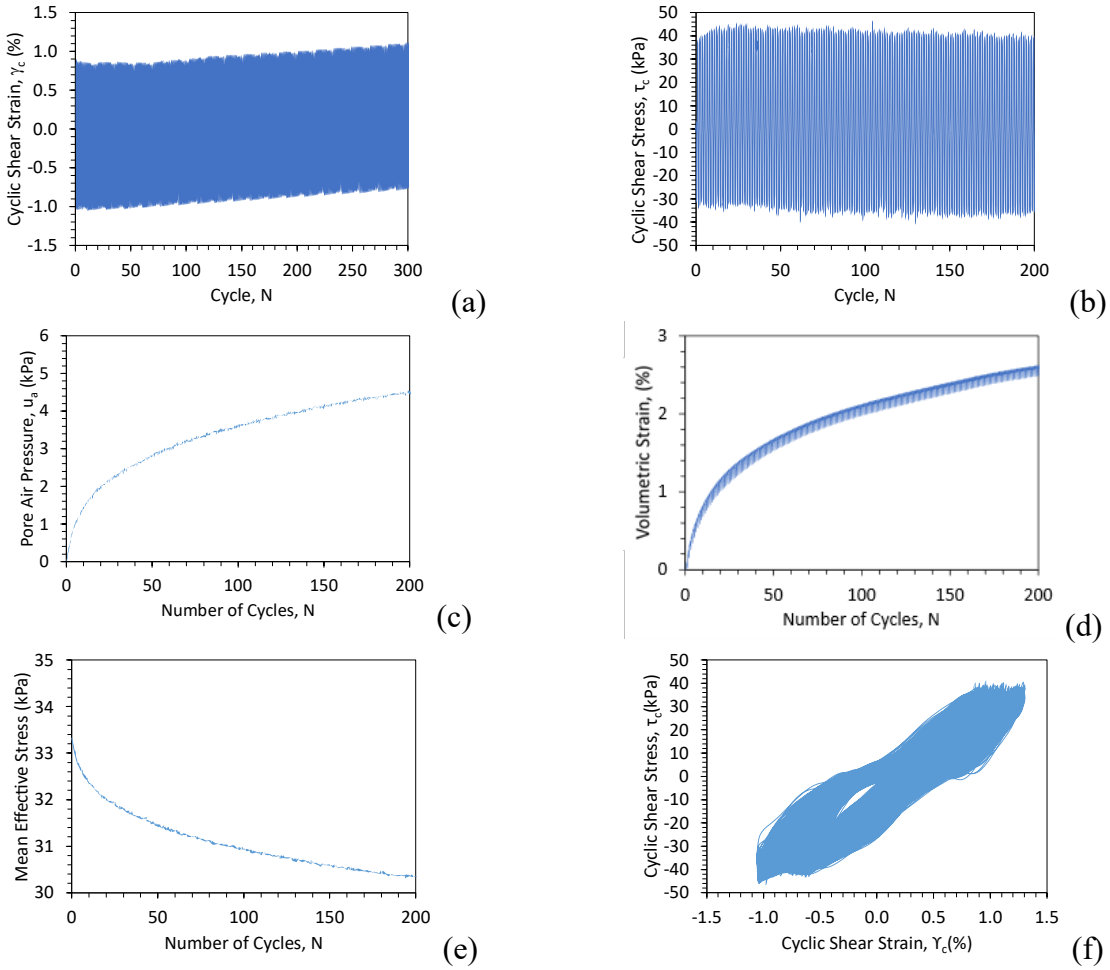

Figure 4.15 Data Set 1* S_0=0 (dry): (a) Shear strain time series; (b) Shear stress time series; (c) Volume change time series; (d) Pore air pressure change time series; (e) Mean effective stress change time series; (f) Cyclic shear stress and cyclic shear strain loops.

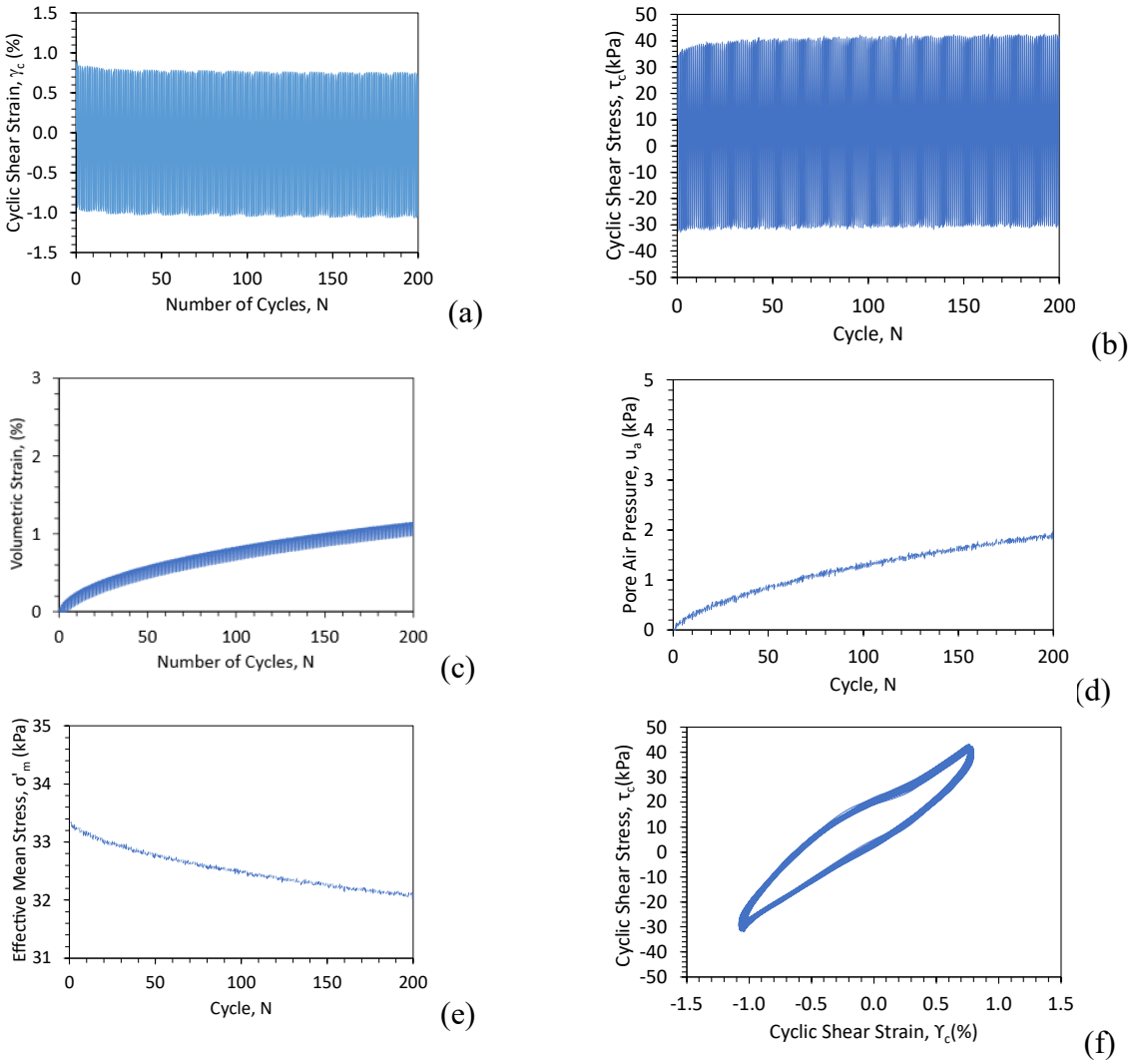

Figure 4.16 Data Set 2* S_0=0 (dry): (a) Shear strain time series; (b) Shear stress time series; (c) Volume change time series; (d) Pore air pressure change time series; (e) Mean effective stress change time series; (f) Cyclic shear stress and cyclic shear strain loops.

5 MODEL CALIBRATION

5.1 CALIBRATION OF BACKBONE CURVE FROM DRAINED SHEARING OF UNSATURATED SAND

While the focus of this report is on the prediction of the seismic compression during undrained cyclic simple shearing, the data available from undrained cyclic simple shear tests performed by Rong and McCartney (2020b) only included tests that were performed to a shear strain of 1%. However, Rong and McCartney (2020a) performed drained cyclic simple shear tests on sands in the same conditions but to higher shear strains. To calibrate the parameters of the backbone shear stress-strain curve, data were used from two drained cyclic simple shear tests on sand at a relative density of 45%, a vertical total stress of 50 kPa, and an initial degree of saturation of 0.3 (corresponding to initial matric suction values of 4 kPa) performed to shear strain amplitudes of approximately 1% and 3%. Two sets of drained shearing data were used to ensure that the calibration provided a good representation of both low and high shear strain ranges. The parameters of the hyperbola were determined by linearizing the hyperbola to determine the slope *a* and intercept *b*, as shown in Figure 5.1. The experimental data for the tests performed to shear strains of 1% and 3% are shown in Figures 5.2 and 5.3 in both natural and transformed scales. The transformed scale was used to identify the slope *a* and intercept *b* that can be used to identify the hyperbolic model parameters G_i and τ_{ult} as described in Appendix A.1.

The calibrated model parameters are summarized in Table 5.1 for the two tests, along with the average value of the parameters used in future model predictions. The shear stresses at failure τ_f in Table 5.1 was determined from the friction angle of this sand of 51.3° reported by Zheng et al. (2019) based on triaxial compression tests on dry sand and the vertical effective stress corresponding to the initial conditions in the specimens. The critical volume friction angle was assumed to be equal to 34°, although further laboratory tests are necessary to better quantify this value. The reduction factors were defined as the ratio of the shear stresses at failure τ_f and the ultimate shear stress from the hyperbolic fitting τ_{ult}, and an average value of $R_f = 0.9$ was used in future predictions. Although only one vertical effective stress was available for calibration of the model in the database developed by Rong and McCartney (2020a, 2020b), the variation in shear modulus with normal stress could not be fully investigated. Accordingly, a value of $n = 0.5$ was used in the calibration (Duncan et al. 1980).

A comparison between the calibrated backbone curve and the hysteretic shear stress-strain curves and the experimental curves from the drained cyclic simple shear tests to shear strains of 1% and 3% is shown in Figure 5.4. A good match was observed between the calibrated and experimental curves. In this figure, the backbone curve is approaching the shear stress at failure at a shear strain of 10%. However, the test at 3% cyclic shear strain has a slightly steeper stress-strain loop upon application of negative shear strains, with maximum shear stresses close to the value at failure. When cyclic shear stress amplitude is close to the value at failure, there is a likelihood for creep or cyclic degradation that could lead to complex behavior. Fortunately, all the undrained cyclic simple shear tests performed by Rong and McCartney (2020b) were performed at a cyclic shear strain amplitude of approximately 1% and are well below the shear stress at failure.

During each cycle of shearing, plastic shear strains will occur during loading and reloading. Accordingly, plastic volumetric strains will also be generated. This means that the model parameters governing the evolution in the plastic shear strain during cyclic shearing are those governing the shape of the hysteretic shear stress-strain curve. Similarly, the degree of saturation can be directly calculated from the volumetric strain using phase relationships without the need for additional model parameters. Similarly, the pore air pressure model developed in Chapter 3 and Appendix A.3 did not include additional parameters beyond the initial conditions of the sand specimen and those necessary to predict the plastic volumetric strain.

5.2 CALIBRATION OF PORE WATER PRESSURE GENERATION MODEL

Different from the model for the pore air pressure generation, the model for the pore water pressure generation depends on the shape of the transient SWRC scanning paths for specimens with different initial degrees of saturation. An interesting aspect from evaluation of the undrained cyclic simple shear results of Rong and McCartney (2020b) indicates that the slope of the transient changes in degree of saturation and matric suction will change during cyclic shearing, with greater changes for specimens with higher initial degrees of saturation, as shown in Figure 5.5.

Since the volumetric strain (seismic compression) data is changing most rapidly at the onset of cycling, the first 1.25 cycles of simple shearing are averaged to see the prediction response of the saturation versus matric suction. The shear modulus model parameters (n^e, $k_G{}^e$) were calibrated from the first cycle of shearing, and therefore it seemed logical to calibrate the transient curve in the same manner for comparison.

Using undrained experimental data from cyclic simple shearing of initial saturations in the funicular regime at 1% strain, the initial 1.25 cycles of the saturation versus matric suction data are fit to the linear equation in excel. Initial parameters are selected for the slope (m). An excel column is created with the transient scanning curve equation for matric suction using a selected slope (m) and the input saturation (S) will be the actual data points from the 1.25 undrained cycling data. Another excel column is created to compute the squared difference between the calculated matric suction (using the selected slope parameter) and the actual matric suction data. A cell is

designated as the residual sum of squares and is used to calculate the sum of the squared differences of the predicted matric suction and data matric suction column. Using Solver in MS Excel, the residual sum of squares is input as the 'target cell' and was selected to be minimized by changing the value of *m* to fit the transient SWRC scanning path slopes. MS Excel was used to compute the values of *m* that best fit the actual matric suction data by reducing the residual sum of squares to 0. The same procedure was used to find the slopes of the transient scanning curve at 200 cycles.

Using the above procedure, the rewetting transient SWRC scanning path of the undrained specimen can be defined as a log-linear equation to track the changes in saturation with the changes in matric suction (the equation is derived in Appendix A3). Undrained cyclic simple shear tests in Data Set 01 from Rong and McCartney (2020b) have initial degrees of saturation ranging in the funicular regime and are presented in Table 4.2 with corresponding initial matric suctions. The calibrations of the undrained data from 1.25 cycles were found to have initial slopes very close to the same value despite the range in initial saturations and is presented in Figure 5.6.

The undrained cyclic simple shear transient SWRC slopes from Data Set 1 for 200 cycles at 1% shear strain is presented in Figure 5.7. It is apparent from the undrained experimental cyclic simple shear data that the slope of the transient curve is higher for specimens with higher initial saturation. The cyclic simple shear data showed the initial transient SWRC slopes at 1.25 cycles for all the funicular regime saturations were approximately the same value of 0.021. The average transient SWRC slope over the entire 200 cycles for each set of unsaturated undrained data is presented in Table 5.2.

The test at the lowest degree of saturation of S = 0.117 had no further evolution in the transient SWRC slope and remained constant at 0.021. The transient SWRC slope increased for initial degrees of saturation in the funicular regime that were larger than S = 0.117. A new variable S_f was defined as an initial degree of saturation higher than test value of 0.117. The increase in transient SWRC slope for each initial degree of saturation in the funicular regime was represented by the variable m_{sf}, which represents the new predicted slope based on the lowest slope value for initial degree of saturation $S = S_{s=0.117}$ = 0.117. The initial transient SWRC slope of the lowest saturation ($m_{s=0.117}$ = 0.021) that had no further change in the transient SWRC slope can be represented as follows:

$$m_{sf} = m_{s=0.117} + S_{s=0.117}S_f \quad (5.4.1a)$$

$$m_{sf} = 0.021 + 0.117S_f \quad (5.4.1b)$$

Using the empirically derived equation in Eq. (5.4.1), the transient SWRC slope at the lowest initial degree of saturation was linked with the transient SWRC slope for higher initial degrees of saturation in the funicular regime. Figure 5.8(a) shows the initial transient slope averages at 1.25 cycles and 200 cycles from the undrained cyclic simple shear tests and Figure 5.8(b) shows the empirically derived equation representing the evolution in the transient slope with continued cycles of shear strain in blue with the data from the undrained cyclic simple shear tests in orange. Using the empirical equation to derive the remaining transient slopes from the lowest initial degree of saturation allows for fewer tests to model the full range of saturations in the funicular regime. The

predicted slope values can be found in Table 5.3 which are similar to those in Table 5.2. It is important to note that the empirical model described in this chapter is only relevant to the funicular regime of the SWRC, and that other mechanisms of pore water pressure change during cyclic shearing are likely in the residual, capillary, and saturated regimes of the SWRC. The empirical model for the parameter m in Equation 5.4.1 was found to have an important impact on the predictions of the elasto-plastic model.

CHAPTER 5: TABLES

Table 5.1 Calibrated hyperbolic model parameters for drained tests at a constant suction of 4 kPa performed to 1% and 3% shear strain.

Strain Amplitude	Initial Shear Modulus	Ultimate Shear Stress	Shear Stress at Failure	Reduction Factor	Shear Modulus Number	Shear Modulus Exponent
	$G_i = 1/a$	$\tau_{ult} = 1/b$	τ_f	R_f	k^e_G	n_e
(%)	(kPa)	(kPa)	(kPa)	(unitless)	(unitless)	(unitless)
1	5950	68.89	63.91	0.9277		
3	5810	72.52	63.91	0.8813		
Average	-	-	-	0.9	100	0.5

Table 5.2 Averaged transient SWRC slopes over entire 200 cycles from undrained cyclic simple shear tests (Data Set 01) for initial degrees of saturation in the funicular regime.

Initial Degree of Funicular Saturation (S_f)	0.117	0.2	0.3	0.4	0.558
Slope (m_{200})	0.021	0.043	0.053	0.076	0.085

Table 5.3 Predicted transient SWRC slopes from the empirical equation for initial degrees of saturation in the funicular regime.

Initial Degree of Funicular Saturation (S_f)	0.117	0.2	0.3	0.4	0.558
Slope (m_{200})	0.021	0.045	0.056	0.070	0.086

CHAPTER 5: FIGURES

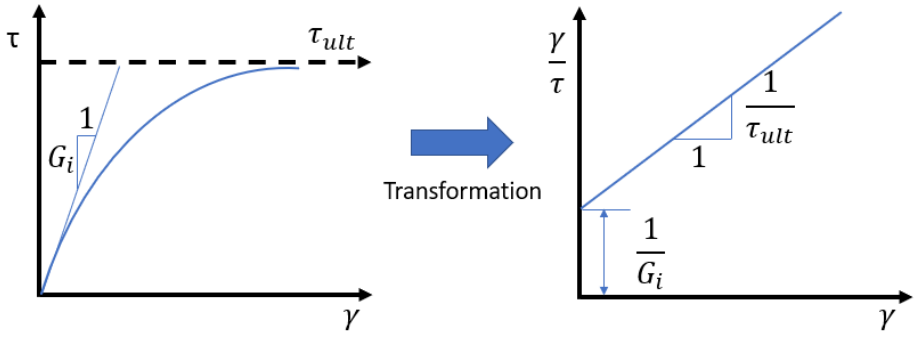

Figure 5.1: Linear transformation of hyperbolic shear stress-strain relationship.

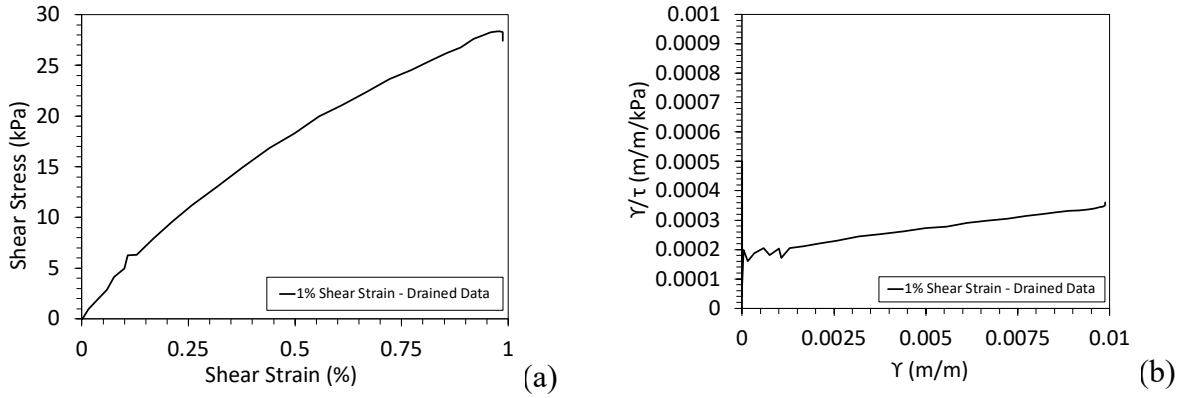

Figure 5.2 Hyperbolic fitting process for the first 0.25 cycles of the drained cyclic simple shear test to 1% shear strain: (a) Monotonic loading to 1% shear strain; (b) Linearization of curve to find hyperbolic parameters.

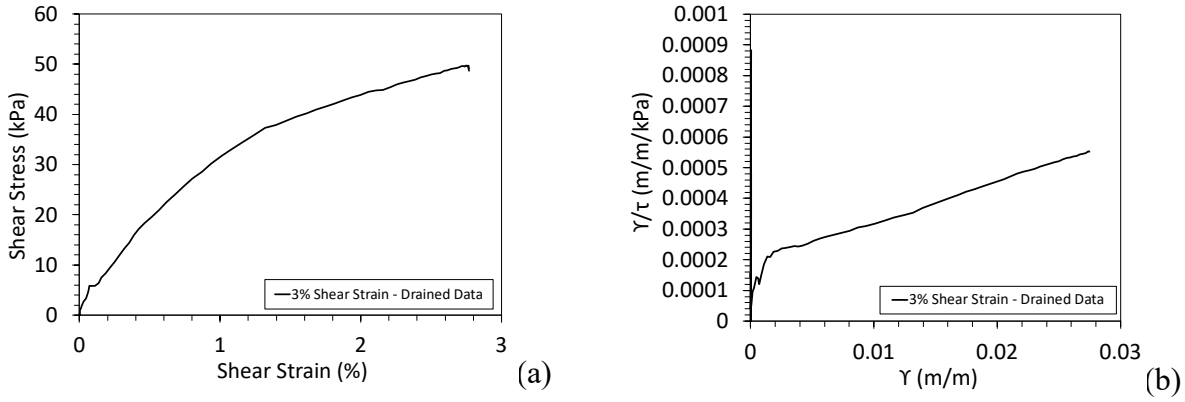

Figure 5.3 Hyperbolic fitting process for the first 0.25 cycles of the drained cyclic simple shear test to 3% shear strain: (a) Monotonic loading at 3% shear strain; (b) Linearization of curve to find hyperbolic parameters.

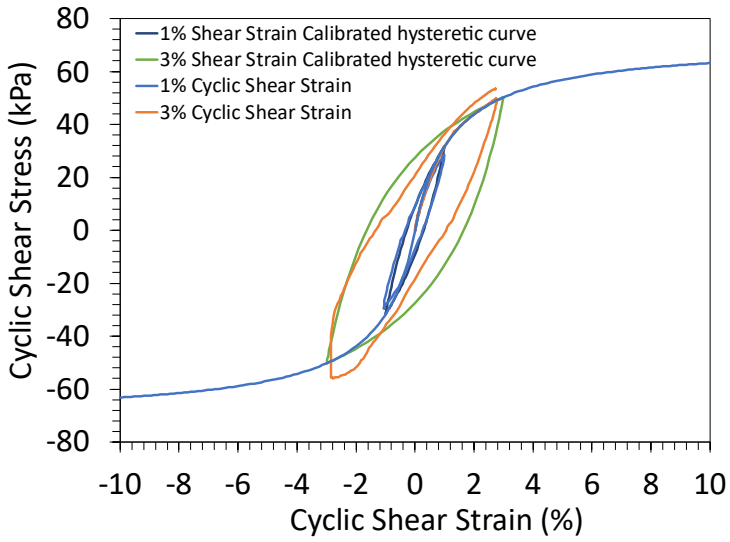

Figure 5.4 Comparison of the calibrated backbone and hysteretic shear stress-strain curves with the experimental data for S_0 = 0.3 and σ_v = 50 kPa from drained cyclic simple shear tests performed by Rong and McCartney (2020a).

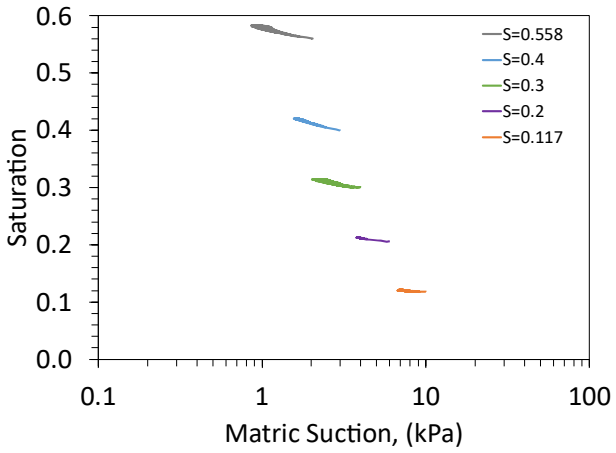

Figure 5.5 Transient SWRC wetting paths of undrained cyclic shear Data Set 1 after 200 cycles.

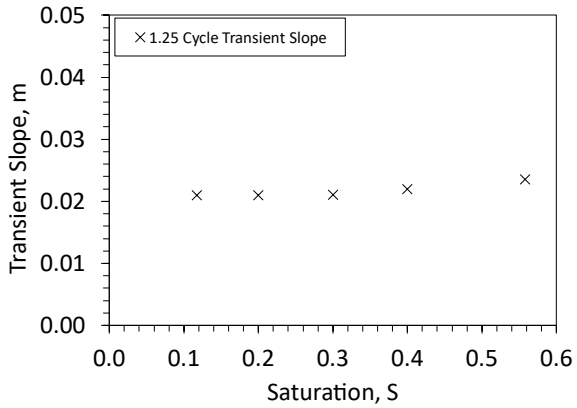

Figure 5.6 Slopes of transient SWRC wetting paths of data after 1.25 cycles of undrained cyclic simple shear.

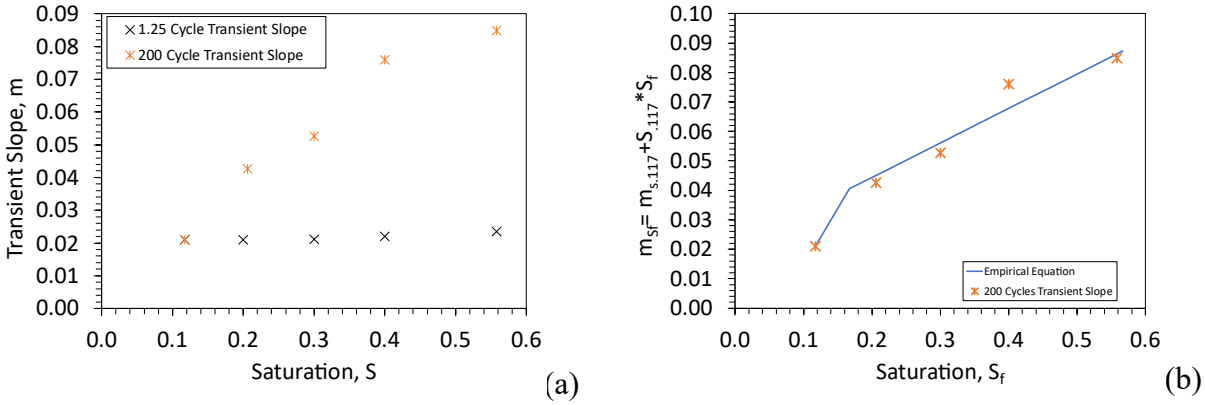

Figure 5.7 (a) Slopes of the transient SWRC scanning curve with averages at 1.25 cycles and 200 cycles; (b) Empirical prediction of the slope of the transient SWRC scanning curve with degree of saturation in the funicular regime for 200 cycles.

6 ANALYSIS

6.1 EVOLUTION IN HYDRO-MECHANICAL VARIABLES DURING UNDRAINED CYCLIC SHEARING

This section presents an example of the evolution in the key hydro-mechanical variables during undrained cyclic shearing up to 200 cycles for one of the tests on a sand specimen having an initial matric suction 4 kPa and an initial saturation of 0.3. Comparisons between the evolution in key hydro-mechanical variables during undrained cyclic shearing for the other tests with different initial conditions summarized in Table 4.2 are presented in Appendix A.6. A comparison between the model prediction and the experimental results is shown in Figure 6.1 for a cyclic shear strain amplitude of 1% (model results in black, data in grey). The results in Figure 6.1(a) indicate that the model captures the evolution in the volumetric strain well for this test, especially at the beginning and end of cyclic shearing. The quality of the model prediction for other degrees of saturation is not always as good as shown in Figure 6.1, as noted in the figures in Appendix A.6, and the quality of prediction is sensitive to the calibration parameters summarized in Chapter 5. The results of the model indicate that the mean effective stress decreases with increasing cycles, which corresponds to a softening in the small strain shear modulus. This observation is consistent with an analysis of changes in the inclination of the experimental hysteretic shear stress-strain loops made by Rong and McCartney (2020b). The predicted volumetric strain (or the seismic compression) increases nonlinearly due to the decrease in mean effective stress, which was also observed in the experimental undrained cyclic simple shear test results. The predicted changes in pore air and water pressures were found to increase at different rates during cyclic simple shearing which results in a decrease in the predicted value of matric suction from the models. Note that this is one of the first models that is capable of independently predicting changes in the pore air and water pressures during compression of unsaturated soils. Most previous elasto-plastic models like Seid-Karbasi and Byrne (2007) assume that the changes in pore air and water pressure are equal during compression.

6.2 EVALUATION OF THE EFFECTS OF INITIAL DEGREE OF SATURATION ON SEISMIC COMPRESSION

A comparison between the evolution in the key hydro-mechanical variables between the different tests in Data Set 1 is shown in Figure 6.2. The dry soil had the highest volumetric strain (seismic compression) in both the model and the experiments. Overall, the model represents the evolution in hydromechanical variables well during many cycles of undrained shearing. However, the model predictions for the volumetric strain (seismic compression) and mean effective stress deviated significantly from the experimental data of the specimen having S_0=0.117 as shown in Figures 6.2(a) and 6.2(b). This may be due to a change in the mechanism of seismic compression at low degrees of saturation that is not well captured by the mechanisms considered by the model, in

particular the slope of the transient SWRC scanning path, as well as the calibration of the model parameters in Chapter 5.

Using the calibrated parameters from the backbone curve and transient SWRC scanning path slope (m_{200}) averaged over 200 cycles of undrained cyclic simple shear data, the pore pressures changes, volume compressions and mean effective stress after 15 cycles are predicted and presented with the experimental results in Figure 6.3. The model prediction of the pore matric suction changes over 15 cycles show a linear decreasing trend with increasing initial saturation, which is similar to the trend in the experimental data. The model prediction of the pore air pressure changes over 15 cycles shows a linear increasing trend with decreasing initial saturation, which is in agreeance with the trend in the experimental data. However, the model prediction of the pore water pressure changes over 15 cycles appears to overpredict the trend in the experimental data. This may be due to changes in the slope of the transient SWRC scanning path during seismic compression that is not fully captured by the empirical model in Equation 5.4.1. The model predictions of volumetric strain (seismic compression) appear to overpredict the experimental results at lower initial degrees of saturation of 0.117, 0.2 and 0.3 but are closer to the experimental results at higher initial saturations of 0.4 and 0.558. Some of the differences in the prediction of the volumetric strains could be due to the assumption that unloading is purely elastic, which may overestimate hysteretic damping in the soil specimen, which is a topic that should be further investigated in future models. The model predictions of mean effective stress show a decreasing trend with increasing initial saturations, which is consistent with the trend in the experimental data at 15 cycles of shearing.

Using the calibrated parameters from the backbone curve and transient SWRC scanning path slope (calibrated to 200 cycles), the changes in matric suction, pore air and water pressures, volumetric strain (seismic compression), and mean effective stress after 200 cycles of shearing are shown in Figure 6.4. The change in matric suction in Figure 6.4 indicates that the model and experimental data generally agree, where lower changes in matric suction are observed at higher initial degrees of saturation. However, comparison of the predicted and experimental changes in pore air pressure and pore water pressure in Figures 6.4(b) and 6.4(c), respectively, indicates that the reason for the decreasing trend in matric suction may not be the same in the model and the experiment. The experimental results show that the changes in pore air and water pressures both increase with increasing initial degree of saturation, but that the pore water pressure changes at a slower rate leading to the decrease in matric suction. The model shows only a slight increase in the change in pore air pressure with increasing initial degree of saturation, but a decreasing trend in the change in pore water pressure, which contributes to the decrease in the change in matric suction with increasing initial degree of saturation. The results in Figure 6.4(d) show that the volumetric strain from the model decreases linearly with increasing initial degree of saturation, while the experiments indicate the greatest volumetric strain for soils having an initial degree of saturation between 0.3 and 0.4. Rong and McCartney (2020b) hypothesized that this was due to the large changes in pore air pressure and pore water pressure in this range. The lowest degree of saturation in the undrained experiments had the lowest volumetric strain (seismic compression), however the model's predictions showed a linear increasing trend with the S=0.117 having the largest compressive volumetric strain aside from the modeled dry case. Despite the inconsistency shown

in the predicted volumetric strains in Figure 6.4(d) with the cyclic simple shear data, the linear decreasing trend in seismic compression is consistent with the predictions from the model of Ghayoomi et al. (2013) for sands in the funicular regime tested using centrifuge shake table tests. The model and the experiment both show an increasing change in mean effective stress (which will lead to hardening of the shear modulus) for soils with increasing initial mean effective stress. However, the experiments show a greater increase in the change in mean effective stress than the model.

The predicted transient SWRC scanning path slopes after 200 cycles for Data Set 1 are shown in Figure 6.5. Overall, a good match between the predicted and experimental transient SWRC scanning paths is observed, with the soils with the highest initial degree of saturation showing the most deviation during the 200 cycles of shearing. A different empirical model that can better capture the nonlinear increase in the transient SWRC scanning path slopes may be a possible way to improve the prediction of the model at higher cycles of shearing.

6.3 EVALUATION OF REASONS BEHIND DISCREPANCY BETWEEN MODEL AND EXPERIMENTS

6.3.1 Pore Air Pressure Generation

The predictions of pore air pressure generation from the model at 15 cycles show an increase with rising levels of initial degree of saturation. Similar results were observed in the undrained cyclic simple shear data showing that higher initial degrees of saturation garnered more pore air compression and volume compression. The results in Figure 6.6 show that the model predicts an increasing trend in pore air pressure as initial degrees of saturation increase. During undrained cyclic simple shear, the air voids are squeezed by the pore water (due to the incompressibility of water) which increases the pore air pressure. A specimen with a higher initial saturation will contain more water exerting pressures on the air-filled voids and therefore will garner more air pressure generation in the voids during undrained cyclic simple shear. The poromechanical coupling effect of the pore water squeezing the air voids to induce volumetric strain (seismic compression) results in an overall increase to the saturation of the pore voids and a reduction in the mean effective stress of the soil skeleton. The predictions of pore air pressure at 15 cycles in Figure 6.6(a) appear to capture the characteristic behavior of a loose granular soil. However, after several cycles the predicted pore air pressures approach similar values with slight increases for higher initial degrees of saturations as observed in Figure 6.6(b). This was an unexpected observation from the model and may be due to the hydro-mechanical coupling effects on the mean effective stress for the different tests.

At 15 cycles, the model predictions of matric suction are captured by the uneven generation of pore water and air pressure. The model's results exhibited a decreasing trend in the matric suction regardless of 15 or 200 cycles, which is consistent with the available undrained cyclic shearing data from the literature. Similar trends were reported in Craciun and Lo (2010) showing a decrease in the matric suction of unsaturated soils during repeated cycles of undrained shearing on

unsaturated soils. As the soil experiences a decrease in matric suction during undrained cyclic simple shearing, the largest air voids become flooded with nearby capillary water due to the shaking and rearrangement of soil particles. Occluded air bubbles can become trapped within water-filled pores due to the wetting process during cyclic shearing and may then damp out changes in pore water pressure during soil particle rearrangement.

6.3.2 Pore Water Pressure Generation

The slope of the transient SWRC scanning curve is highly dependent on the applied shear strain, number of cycles of shearing, initial degree of saturation, and initial matric suction. Although the vertical effective stress does contribute to volumetric strain (seismic compression), it is not as significant as the effect of shear strain as the vertical total stress is maintained constant and changes in suction and degree of saturation have relatively small effects on the vertical effective stress. The pore water has a dual effect, as changes in pore water pressure and changes in degree of saturation (associated with decreases in pore air volume) can affect the effective stress during cyclic shearing depending on the drainage conditions. If the drainage conditions permit water to leave and matric suction increases, this typically correlates to a decrease in pore void water as the water is drawn out of the soil (drying effects) and the effective stress increases. When performing undrained cyclic simple shear tests, the matric suction will inevitably decrease due to the inability of water to flow out of the sample leading to air void compression (causing plastic volumetric strain), an increase in degree of saturation and a decrease in effective stress. The hyperbolic model developed in this study captures the trends in data from cyclic simple shear testing to aid in replicating the seismic compression response of unsaturated sand during an earthquake, but the trends are only reliable at this point for the initial cycles and begin to deviate after 15 cycles.

The hyperbolic model developed in this study was calibrated using data from drained cyclic simple shear experiments conducted by Rong and McCartney (2020a), and the slopes of the transient SWRC scanning path from Rong and McCartney (2020b) for initial cyclic shearing data at 1.25 cycles and 200 cycles to fit and predict the pore pressures and volumetric changes of a sand specimen of approximately 45% density under a vertical stress of 50 kPa and 1% applied cyclic shear strain. The model does not provide insight into how the initial slope of the transient SWRC scanning path changes with higher or lower shear strains. More undrained tests of unsaturated sands at higher or lower shear strains are needed to provide insight on how the transient slopes evolve with increasing or decreasing shear strain. The slopes of the transient SWRC scanning path are a function of the applied cyclic shear strain, initial degree of saturation and initial matric suction, and the model predictions are very sensitive to this slope. Since the model is centralized around the slopes of the transient scanning curve, it can only accurately predict the volumetric strains and pore pressure generation for the sand specimen at D_r=0.45 and 1% cyclic shear strain and suctions in the funicular regime of the SWRC, so further study is needed to generalize this model for other conditions. In the undrained cyclic simple shear tests, the slope of the transient curve increases for initial degrees of saturations higher than 0.117 after initial cycling. Although there is a deviation in the model predictions of pore pressure generation after numerous cycles, the

model still provides a good approximation to the pore air generation and matric suction trends compared to the experimental undrained cyclic simple shear data up to 15 cycles. .

A compilation of the model results using the transient SWRC scanning path slope empirical equation (Equation 5.4.1b) based on the lowest transient SWRC scanning path slope at the initial degree of saturation $S_0 = 0.117$ are summarized in Appendix A.6. The results of the model's predicted volumetric strains (seismic compressions) increase due to the response of the saturation change is more accurately captured given the change from the initial slope. The mean effective stress decreased which corresponds to the increase in volumetric strain (seismic compression). The model prediction of the pore air pressure increased while the pore water pressure predictions decreased slightly. The largest variation is captured in the degree of saturation versus matric suction plots shown in Figures 6.7(a) and 6.7(b). Additional improvements to the model may be necessary to better capture the changes in the slope of the transient SWRC scanning path, as this was found to have a major impact on the model predictions. For example, the effects of using the slopes of the transient SWRC scanning path calibrated from the data after 1.25 cycles and after 200 cycles are shown in Figure 6.8(a) and 6.8(b), respectively. This slope affects not only the prediction of the ultimate change in matric suction after 200 cycles but also the transient changes in matric suction during application of these cycles.

6.4 IMPLEMENTATION OF THE NEW CONSTITUTIVE MODEL INTO SITE-SPECIFIC SEISMIC RESPONSE ANALYSES

The model developed in this study was only evaluated for sinusoidal cyclic shearing due to the goal of comparing predictions with available cyclic simple shear data. Due to the simplicity of the cyclic shear strain time histories input into the model, the model was implemented into MS Excel for simplicity. Further developments in the linkage between the SWRC transient scanning paths may be necessary to simulate other shear strain-controlled time histories. Further, it may be better to implement the model into Matlab[1] or Python[2] for greater flexibility. The model developed in this study can be incorporated into site-specific seismic response analyses using finite element techniques (e.g., OpenSees[3], Plaxis[4]) or finite difference techniques (e.g., FLAC[5]). The UBCSAND model that was used as the basis for the model in this study has already been implemented into FLAC.

[1]MATLAB, 2022. version R2022b, Natick, Massachusetts: The MathWorks Inc.
[2] Van Rossum, G. and Drake Jr, F.L., 1995. Python reference manual, Centrum voor Wiskunde en Informatica Amsterdam.
[3] McKenna, F., Scott, M.H., and Fenves, G.L. 2010. "Nonlinear finite-element analysis software architecture using object composition." Journal of Computing in Civil Engineering, 24(1), 95-107.
[4] Brinkgreve, R.B.J., Swolfs, W.M., and Engin, E. 2011. Reference manual Plaxis. Plaxis.
[5] Itasca Consulting Group, Inc. (2019) FLAC — Fast Lagrangian Analysis of Continua, Ver. 8.1. Minneapolis: Itasca.

CHAPTER 6: FIGURES

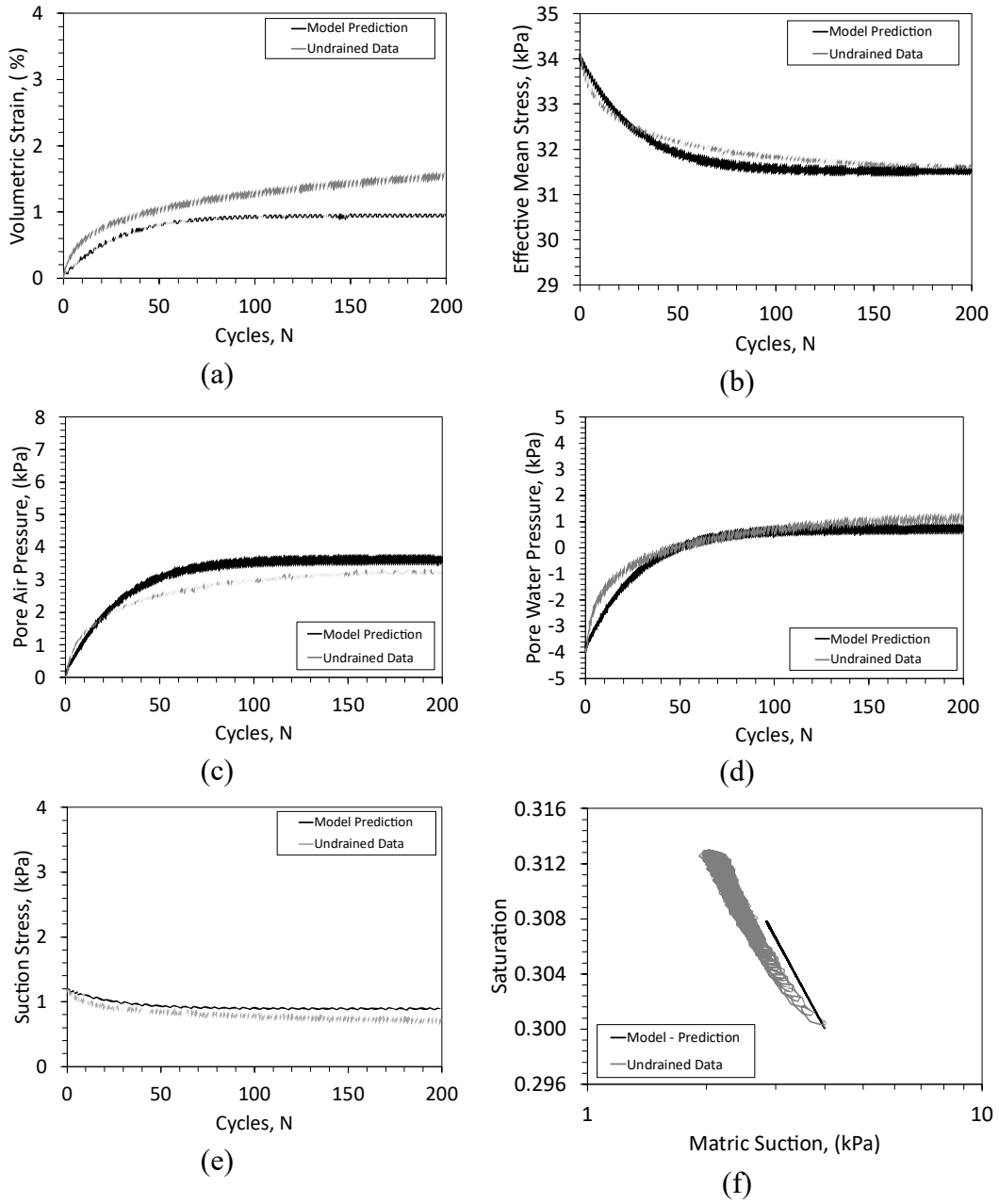

Figure 6.1 Comparison between cyclic simple shear results for a specimen with S_0 = 0.3 and model results: (a) Volume compression after 200 cycles; (b) Mean effective stress changes after 200 cycles; (c) Pore air pressure after 200 cycles; (d) Pore water pressure after 200 cycles; (e) Suction stress after 200 cycles; (f) Transient scanning path after 200 cycles.

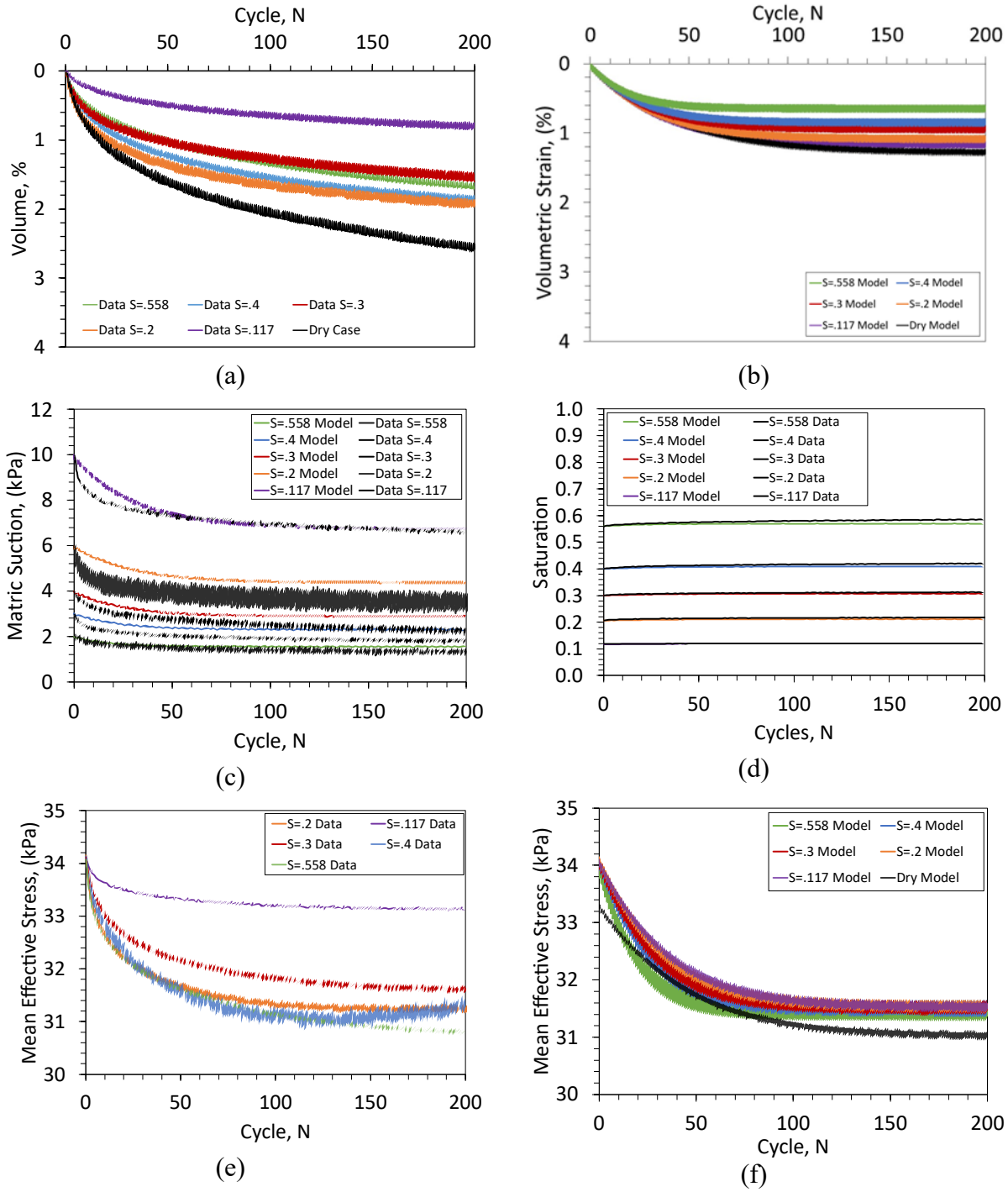

Figure 6.2. Data Set 1 vs. model predictions: (a) Volumetric strain vs. cycles; (b) Model: Volumetric strain vs. cycles; (c) Matric suction vs. cycles; (d) Saturation vs. cycles; (e) Data: Mean stress vs. cycles; (f) Model: Mean stress vs. cycles.

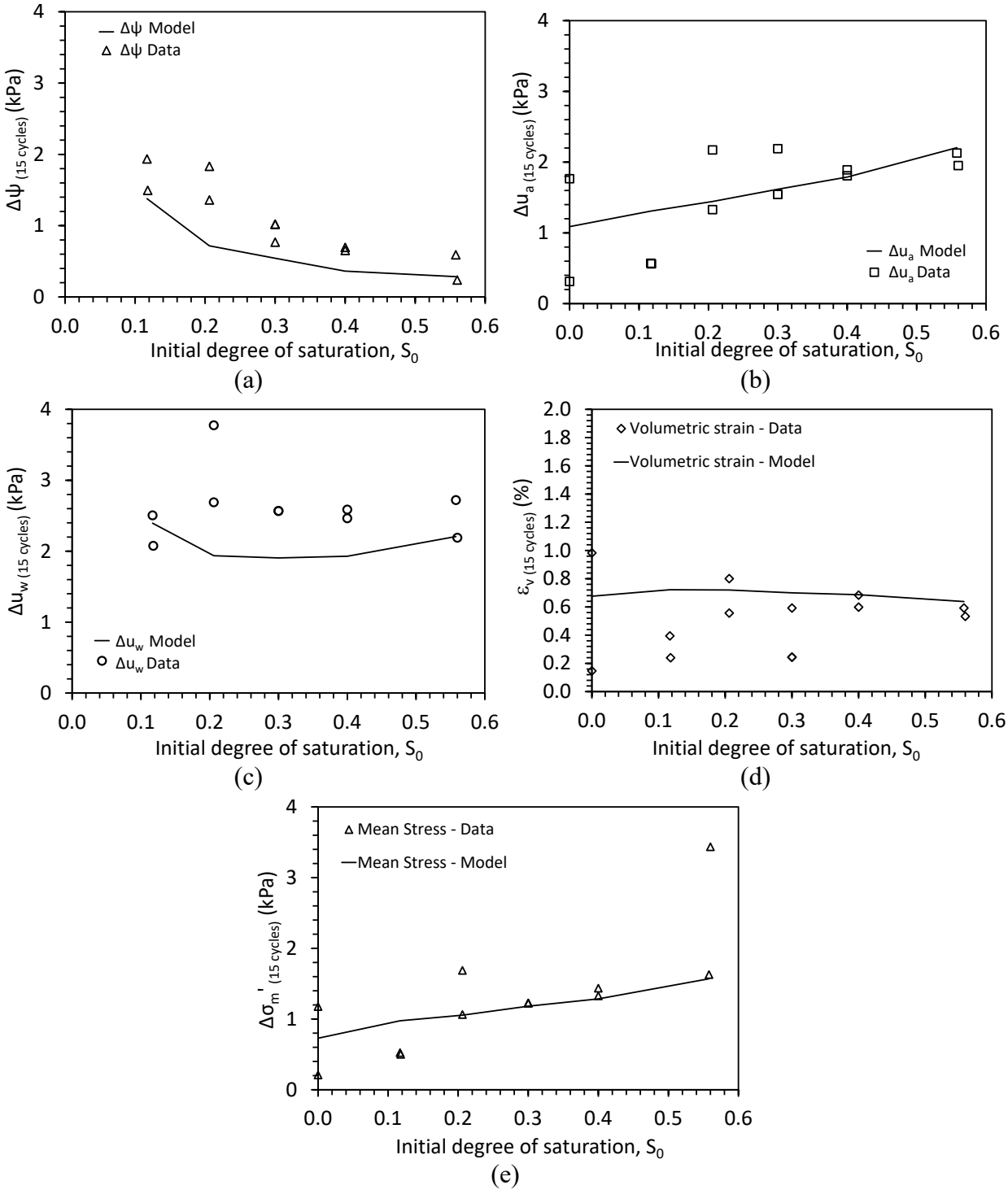

Figure 6.3 Comparison of trends between cumulative changes in key hydro-mechanical variables after 15 cycles of undrained cyclic shearing and the initial degree of saturation obtained from the experiments of Rong and McCartney (2020b) and the model: (a) $\Delta\psi$ vs. S_0; (b) Δu_a vs. S_0; (c) Δu_w vs. S_0; (d) ΔV vs. S_0; (e) $\Delta\sigma'_m$ vs. S_0.

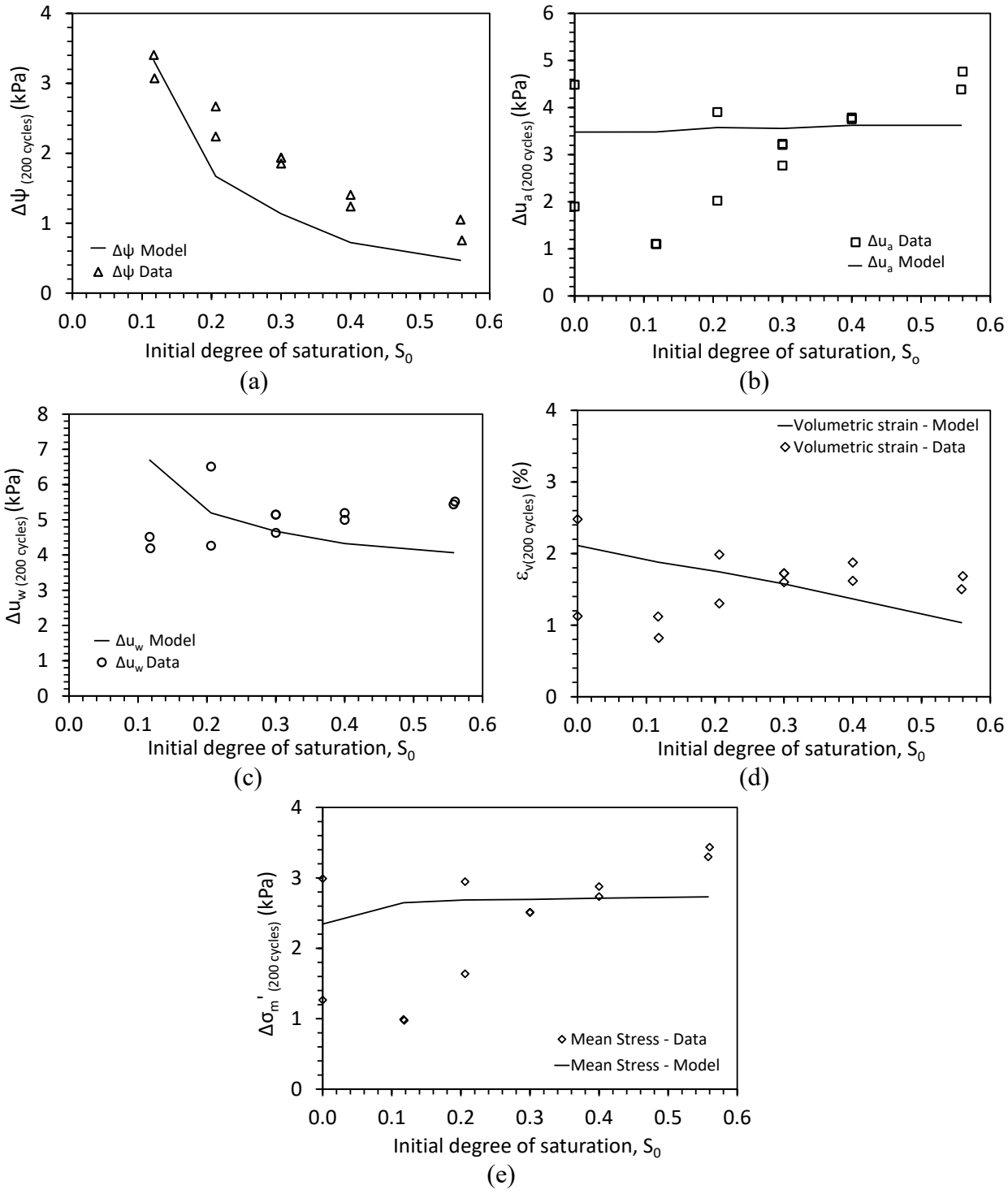

Figure 6.4 Comparison between model predictions and experimental results of cumulative changes in different variables after 200 cycles of undrained shearing: (a) $\Delta\psi$ vs. S_0; (b) Δu_a vs. S_0; (c) Δu_w vs. S_0; (d) ΔV vs. S_0; (e) $\Delta\sigma'_m$ vs. S_0.

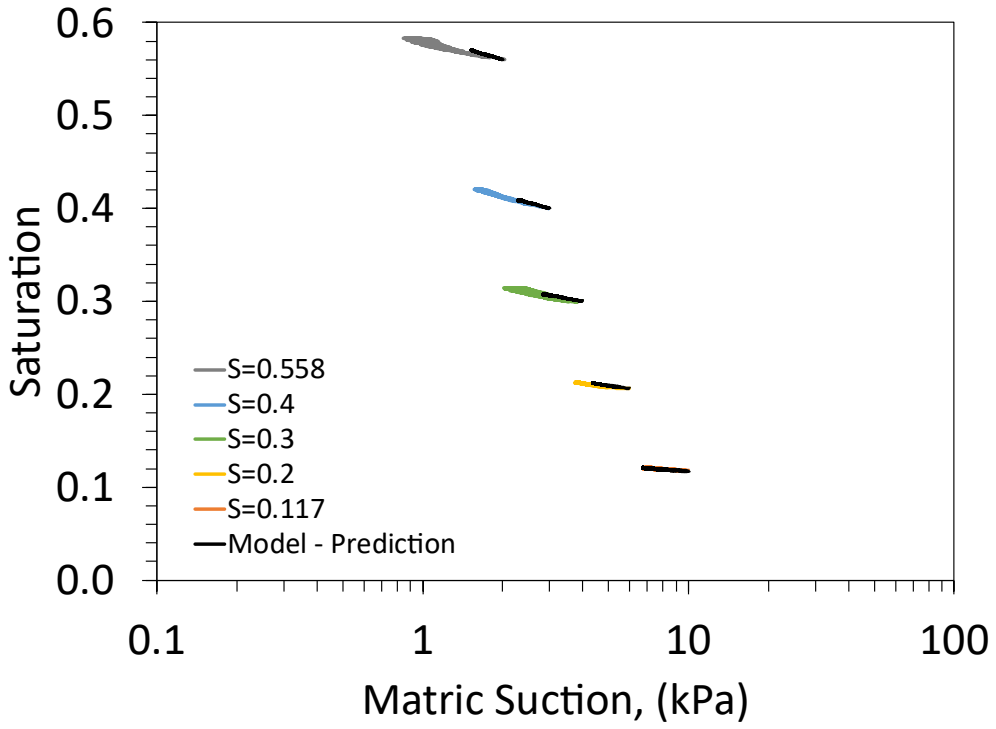

Figure 6.5 Transient SWRC scanning paths and predicted transient SWRC paths for Data Set 1.

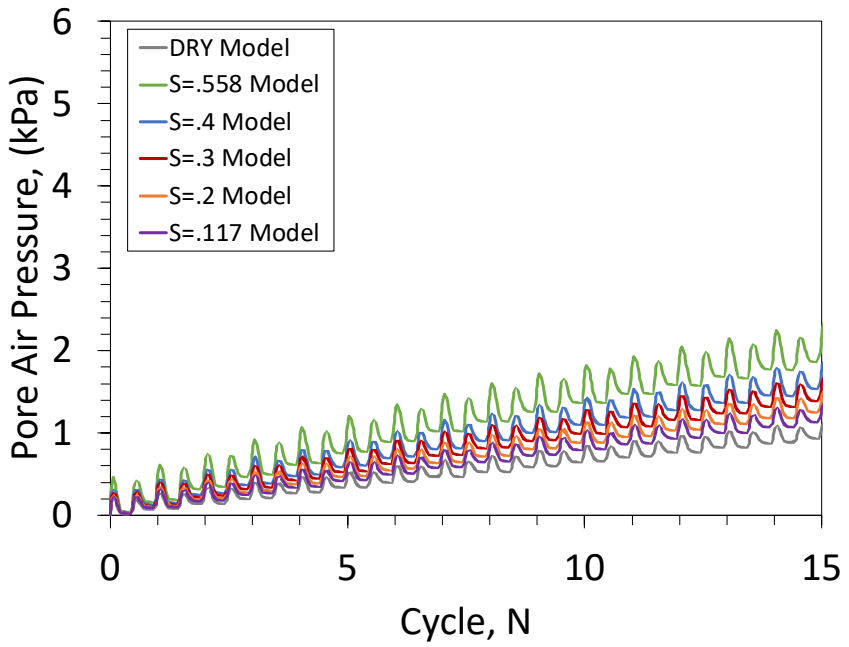

(a)

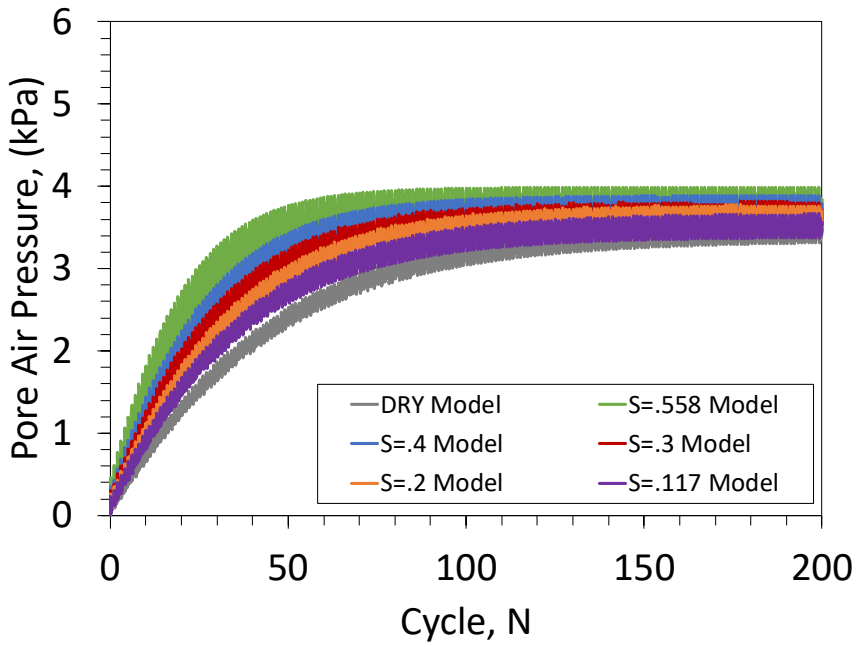

(b)

Figure 6.6 Model predictions of pore air pressure generation by initial saturation after: (a) 15 cycles; (b) 200 cycles.

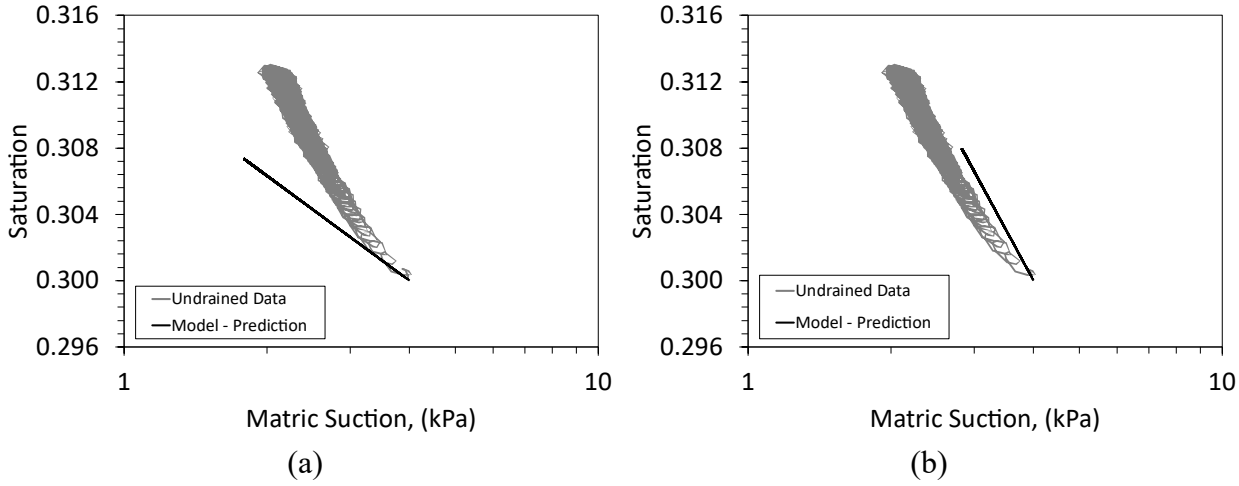

Figure 6.7 Variation in results between Data Set 1 transient SWRC: (a) S_0=0.3, ψ_0=4 kPa model calibrated to 1.25 cycles; (b) S=0.3 ψ=4 kPa model calibrated to 200 cycles.

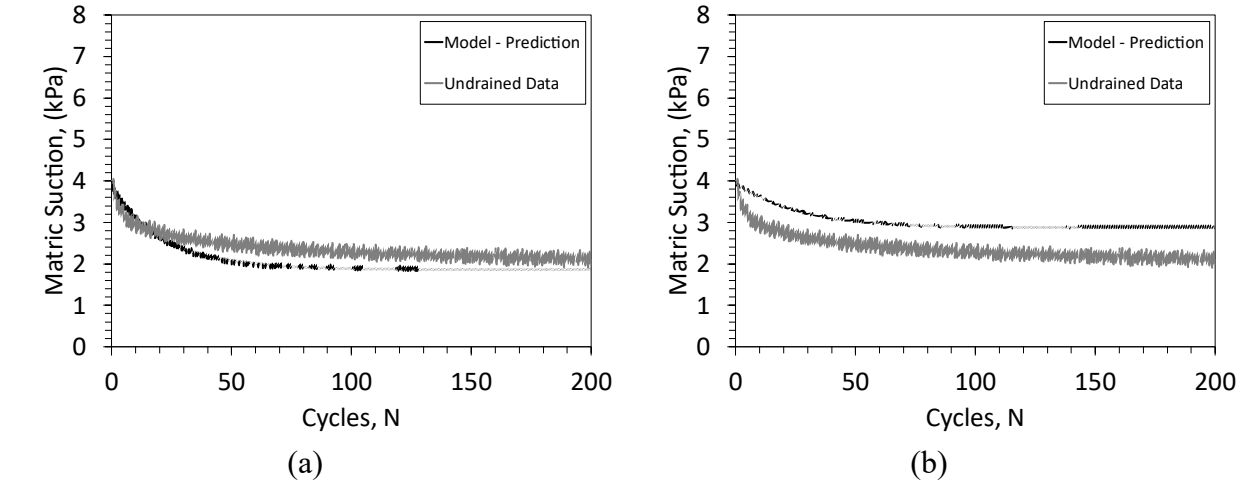

Figure 6.8 Variation in results between Data Set 1 matric suction vs. N cycles: (a) S_0=0.3, ψ_0=4 kPa model calibrated to 1.25 cycles; (b) S_0=0.3, ψ_0=4 kPa model calibrated to 200 cycles.

7 CONCLUSIONS AND FUTURE RESEARCH NEEDS

This study presented the development of a new semi-empirical elasto-plastic constitutive model with a hyperbolic stress-strain curve with the goal of predicting the seismic compression of unsaturated sands in the funicular regime of the soil-water retention curve (SWRC) during undrained cyclic shearing. The model used a flow rule adopted from the UBCSAND model that was derived from energy considerations. The evolution in plastic volumetric strains (seismic compression) were predicted from the plastic shear strains of the hysteretic hyperbolic stress-strain curve. The plastic volumetric strains were then used to predict the changes in degree of saturation from phase relationships and changes in pore air pressure from Boyle's and Henry's laws. A new aspect of this model was that the predicted changes in degree of saturation were used to estimate changes in matric suction from the transient SWRC scanning paths. Changes in small-strain shear modulus estimated from changes in mean effective stress, computed from the constant total stress and changes in pore air pressure, degree of saturation and matric suction, were found to affect the hyperbolic stress-strain curve's shape and the evolution in plastic volumetric strain with cycles of undrained shearing. The model is only intended for unsaturated soils in the funicular regime and a key feature is that it assumes that the pore pressures have different generations due to the presence of air-water menisci with continuous air and water phases. Different mechanisms of seismic compression (i.e., post-liquefaction reconsolidation) are likely for unsaturated soils at higher initial degrees of saturation, which are not considered in this model.

The new model was calibrated using experimental shear stress-strain backbone curves from drained cyclic simple shear tests and transient SWRC scanning path measurements from undrained cyclic simple shear tests. Then the model predictions were validated using experimental data from undrained cyclic simple shear tests on unsaturated sand specimens with different initial degrees of saturation in the funicular regime. The model predictions are only valid when representing soils that have similar conditions to those use in the calibration of the model.

While the new model was found to capture the nonlinear evolution in the coupled hydromechanical variables and volumetric strain (or seismic compression) up to the first 15 cycles of shearing, it underestimated these variables under higher cycles of shearing. After 200 cycles of undrained shearing, a linear decreasing trend between the volumetric strain (or seismic compression) and initial degree of saturation was predicted from the model, which is inconsistent with a nonlinear increasing-decreasing trend observed in the cyclic simple shear experiments used for validation of the model. However, the seismic compressions predicted from the model have a similar trend with the initial degree of saturation to those observed in the model of Ghayoomi et al. (2013) in the funicular regime of the SWRC that was developed based on centrifuge shake table experiments on sand layers during steady-state infiltration. The model also predicted similar changes in pore air pressure for the sands with different initial degrees of saturation, which contradicted the

experimental results. This may be due to the complex coupling between changes in volumetric strain, pore air and water pressures and degree of saturation that may depend on the selection of calibration parameters.

The differences between the model predictions and cyclic simple shear tests may be due to the model not completely capturing all the mechanisms of seismic compression across the range of initial degrees of saturation in the funicular regime. For example, the model did not consider volume change due to drainage of pore water pressures. Another reason for the discrepancy may be because the calibrated model parameters do not completely capture the conditions in the different cyclic simple shear tests. For example, the model predictions were found to be very sensitive to the calibration parameters related to the slope of the transient SWRC scanning paths. This is an important topic for future model development, as it may help refine the evolution in pore water pressure prediction during cyclic shearing. Finally, the difference between the model predictions and experimental results may also be due to experimental issues that could not be captured in the model. For example, the experiments did not always achieve the target shear strain amplitude range (±1%), and a shift in the position of the hysteretic shear stress-strain loops was observed in some tests due to a change in the shear stresses induced by applying the controlled cyclic shear strains.

The model development raised several interesting questions that can be explored in future studies as additional experimental data becomes available. For example, the role of the parameter n_e in the model has not been well explored as Rong and McCartney (2020a, 2020b) performed all tests under the same vertical total stress of 50 kPa. Cyclic simple shear tests performed at different values of mean effective stresses would help to understand the impact of the mean effective stress on the parameters of the hyperbolic curve. Changes in the magnitude of n_e will mean that evolution in the mean effective stress during cyclic shearing will have a greater effect on the evolution in plastic volumetric strain. Cyclic simple shear tests performed at different cyclic shear strain amplitudes may also help to further understand the role of this variable in the amount of seismic compression. Application of actual earthquake records in cyclic simple shear tests may also lead to different results than when using sinusoidal motions as applied by Rong and McCartney (2020a, 2020b). Additional cyclic simple shear tests can be performed to clarify some of the uncertainties in the comparisons between the model predictions and the data. For example, the shift in the center of the shear stress-strain hysteresis loops in the experiments could be better understood, as this may have affected the development of volumetric strains in the experiments. Finally, cyclic simple shear tests performed under the full range of degree of saturation can be performed in the future to help develop, calibrate, and validate a holistic model for seismic compression of unsaturated soils.

REFERENCES

ASTM D6528 (2017). Standard Test Method for Consolidated Undrained Direct Simple Shear Testing of Cohesive Soils. ASTM International. West Conshohocken, PA.

Beaty, M., and Byrne, P.M. (1998). An effective stress model for predicting liquefaction behavior of sand. Geotechnical Earthquake Engineering and Soil Dynamics III. ASCE, Reston, VA. 766-777.

Bishop, A.W. (1959). The principle of effective stress. Teknisk Ukeblad, 106(39), 859-863.

Bishop, A.W. and Blight, G.E. (1963). Some aspects of effective stress in saturated and partly saturated soils. Géotechnique, 13(3), 177-197. DOI: 10.1680/geot.1963.13.3.177.

Bray, J.D. and Olaya, F.R. (2022). Examination of the volumetric strain potential of liquified soil with a database of laboratory tests. GeoCongress 2022, GSP 334, ASCE, Reston, VA, 495-505.

Brooks, R.H., and Corey, A.T. (1966). Properties of porous media affecting fluid flow. Journal of the Irrigation and Drainage Division. ASCE. 92(2), 61-88. DOI: 10.1061/JRCEA4.0000425.

Byrne, P.M., Roy, D., Campanella, R.G., and Hughes, J. (1995). Predicting liquefaction response of granular soils from pressuremeter tests. ASCE National Convention, GSP 56, ASCE, Reston, VA, 122-135.

Byrne, P.M. and Park, S.S. (2003). Seismic liquefaction: centrifuge and numerical modeling. FLAC and Numerical modeling in Geomechanics, Brummer et al. (eds), 320-331. DOI: 10.1201/9781003078531.

Byrne, P.M., Naesgaard, E. and Seid-Karbasi, M., (2006). Analysis and design of earth structures to resist seismic soil liquefaction. 59th Canadian Geotechnical Conference, Canadian Geotechnical Society. 1-24.

Chong, S.H. and Santamarina, J.C. (2016). Sands subjected to repetitive vertical loading under zero lateral strain: accumulation models, terminal densities, and settlement. Canadian Geotechnical Journal, 53(12), 2039-2046. DOI: 10.1139/cgj-2016-0032.

Craciun, O. and Lo, S.C.R. (2010). Matric suction measurement in stress path cyclic triaxial testing of unbound granular base materials. Geotechnical Testing Journal, 33(1), 33-44. DOI: 10.1520/GTJ102390.

Cuomo, S., Moscariello, M., and Foresta, V. (2017). Wetting tests of partially saturated soils under simple shear conditions. Géotechnique Letters, 7(2), 197-203. DOI: 10.1680/jgele.17.00019.

Duncan, J.M. and Chang, C.Y. (1970). Nonlinear analysis of stress and strain in soils. Journal of Soil Mechanics and Foundations Division. 96(5), 1629–1653. DOI: 10.1061/JSFEAQ.0001458.

Duku, P.M., Stewart, J.P., Whang, D.H., and Yee, E. (2008). Volumetric strains of clean sands subject to cyclic loads. J. of Geotech. and Geoenv. Eng., 134(8), 1073-1085. DOI: 10.1061/(ASCE)1090-0241(2008)134:8(1073).

Dong, Y., Lu, N., and McCartney, J.S. (2016). Unified model for small-strain shear modulus of variably saturated soil. J. of Geotech. and Geoenv. Eng., 142(9), 04016039. DOI: 10.1061/(ASCE)GT.1943-5606.0001506.

Dong, Y., Lu, N., and McCartney, J.S. (2017). Scaling shear modulus from small to finite strain for unsaturated soils. J. of Geotech. and Geoenv. Eng., 144(2), 04017110. DOI: 10.1061/(ASCE)GT.1943-5606.0001819.

Finn, W.L., Byrne, P.M., and Martin, G.R. (1976). Seismic response and liquefaction of sands. J. of Geotech. and Geoenv. Eng., 102(8), 841-856. DOI: 10.1061/AJGEB6.0000310.

Finn, W. D. L., and Byrne, P. M. (1976). Estimating settlements in dry sand during earthquakes. Can. Geotech. J., 13(4), 355–363. DOI: 10.1139/t76-037.

Fredlund, D.G. (2016). Variables in saturated-unsaturated soil mechanics. Soils and Rocks, 39(1), 3-17. DOI: 10.28927/SR.391003

Ghayoomi, M., McCartney, J.S., and Ko, H.Y. (2011). Centrifuge test to assess the seismic compression of partially saturated sand layers. Geotechnical Testing Journal, 34(4), 321-331. DOI: 10.1520/GTJ103355.

Ghayoomi, M., McCartney, J.S., and Ko, H.Y. (2013). Empirical methodology to estimate seismically induced settlement of partially saturated sand. J. of Geotech. and Geoenv. Eng., 139(3), 367-376. DOI: 10.1061/(ASCE)GT.1943-5606.0000774.

Ghayoomi, M. and McCartney, J.S. (2016). Procedure to estimate the seismic settlement of partially saturated soils. Indian Geotechnical Journal (Special Issue on Unsaturated Soil Mechanics). 46(3), 272–275. DOI: 10.1007/s40098-015-0176-0.

Hardin, B.O. and Richart, F.E. (1963). Elastic wave velocities in granular soils. Journal of Soil Mechanics and Foundations Divisions, Proc. ASCE, 89, 33-65. DOI: 10.1061/JSFEAQ.0000493.

Hardin, B.O. and Black, W. (1968). Vibration modulus of normally consolidated clay. Journal of Soil Mechanics and Foundations Division. ASCE, 94(2), 353-389. DOI: 10.1061/JSFEAQ.0001100.

Hardin, B.O. and Black, W. (1969). Closure to: Vibration modulus of normally consolidated clay. Journal of Soil Mechanics and Foundations Division. ASCE 95, 1531-1537. DOI: 10.1061/JSFEAQ.0001364.

Hardin, B.O. and Drnevich, V.P. (1972). Shear modulus and damping in soil: design equations and curves. Journal of the Soil Mechanics and Foundations Division, 98(7), 667-692. DOI: 10.1061/JSFEAQ.0001760.

Hoyos, L.R., Suescún-Florez, E.A., and Puppala, A.J. (2015). Stiffness of intermediate unsaturated soil from simultaneous suction-controlled resonant column and bender element testing. Engineering Geology, 188, 10-28. DOI: 10.1016/j.enggeo.2015.01.014.

Ishihara, K., Tatsuoka, F., and Yasuda, S. (1975). Undrained deformation and liquefaction of sand under cyclic stresses. Soils and Foundations, 15(1), 29-44. DOI: 10.3208/sandf1972.15.29.

Ishihara, K. and Yoshimine, M. (1992). Evaluation of settlements in sand deposits following liquefaction during earthquakes. Soils and Foundations, 32(1), 173-188. DOI: 10.3208/sandf1972.32.173.

Ishihara, K. (2001). Recent studies on liquefaction resistance of sand-effect of saturation. In: Proc. 4th International Conference on Recent Advances in Geotechnical Earthquake Engineering and Soil Dynamics, San Diego. 1-7.

Khalili, N., Habte, M.A., and Valliappan, S. (2005). A bounding surface plasticity model for cyclic loading of granular soils. International Journal for Numerical Methods in Engineering. 63, 1939–1960. DOI: 10.1002/nme.1351.

Khosravi, A., Ghayoomi, M., McCartney, J.S., and Ko, H.Y. (2010). Impact of effective stress on the dynamic shear modulus of unsaturated sand. GeoFlorida 2010, ASCE, Reston, VA. 410-419.

Khosravi, A. and McCartney, J.S. (2009). Impact of stress state on the dynamic shear moduli of unsaturated, compacted soils. 4th Asia-Pacific Conf. on Unsat. Soils, Newcastle. 1-6.

Khosravi, A. and McCartney, J.S. (2012). Impact of hydraulic hysteresis on the small-strain shear modulus of low plasticity soils. J. of Geotech. and Geoenv. Eng., 138(11), 1326–1333. DOI: 10.1061/(ASCE)GT.1943-5606.0000713.

Kimoto, S., Oka, F., Fukutani, J., Yabuki, T., and Nakashima, K. (2011). Monotonic and cyclic behavior of unsaturated sandy soil under drained and fully undrained conditions. Soils and Foundations, 51(4), 663-681. DOI: 10.3208/sandf.51.663

Konagai, K., Kiyota, T., Suyama, S., Asakura, T., Shibuya, K., and Eto, C. (2013). Maps of soil subsidence for Tokyo bay shore areas liquefied in the March 11th, 2011 off the Pacific Coast of Tohoku Earthquake. Soil Dynamics and Earthquake Engineering, 53, 240-253. DOI: 10.1016/j.soildyn.2013.06.012.

Lu, N., Godt, J.W., and Wu, D.T. (2010). A closed form equation for effective stress in unsaturated soil. Water Resources Research, 46(5), 55-65. DOI: 10.1029/2009WR008646.

Le, K.N. and Ghayoomi, M. (2017). Cyclic direct simple shear test to measure strain-dependent dynamic properties of unsaturated sand. Geotechnical Testing Journal, 40(3), 381-395. DOI:10.1520/GTJ20160128.

Martin, G.R., Finn, W.L., and Seed, H.B. (1975). Fundamentals of liquefaction under cyclic loading. J. of Geotech. and Geoenv. Eng., 101(5), 423-438. DOI: 10.1061/AJGEB6.0000164.

Menq, F.Y. (2003). Dynamic Properties of Sandy and Gravelly Soils. Doctoral Dissertation. University of Texas at Austin.

Milatz, M. and Grabe, J. (2015). A new simple shear apparatus and testing method for unsaturated sands. Geotechnical Testing Journal, 38(1), 9-22. DOI: 10.1520/GTJ20140035.

Mele, L., Tian, J.T., Lirer, S., Flora, A., and Koseki, J. (2019). Liquefaction resistance of unsaturated sands: experimental evidence and theoretical interpretation. Géotechnique, 69(6), 541-553. DOI: 10.1680/jgeot.18.P.042.

Naesgaard, E., (2011) A Hybrid Effective Stress-Total Stress Procedure for Analyzing Soil Embankment Subjected to Potential Liquefaction and Flooding. Doctoral Dissertation. The University of British Columbia. 1-213.

Ng, C.W.W. and Xu, J. (2012). Effects of current suction ratio and recent suction history on small-strain behavior of an unsaturated soil. Canadian Geotechnical Journal, 49(2), 226-243. DOI: 10.1139/t11-097.

Okamura, M. and Soga, Y. (2006). Effects of pore fluid compressibility on liquefaction resistance of partially saturated sand. Soils and Foundations, 46(5), 695-700. DOI: 10.3208/sandf.46.695.

Okamura, M. and Noguchi, K. (2009). Liquefaction resistances of unsaturated non-plastic silt. Soils and Foundations, 49(2), 221-229. DOI: 10.3208/sandf.49.221.

Oka, F., Kodaka, T., Suzuki, H., Kim, Y.S., Nishimatsu, N., and Kimoto, S. (2010). Experimental study on the behavior of unsaturated compacted silt under triaxial compression. Soils and Foundations, 50(1), 27-44. DOI: 10.3208/sandf.50.27.

Pradel, D. (1998). Procedure to evaluate earthquake-induced settlements in dry sandy soils. J. Geotech. Geoenviron. Eng., 124(4), 364–368. DOI: 10.1061/(ASCE)1090-0241(1998)124:4(364).

Puebla, H., Byrne, P.M., and Phillips, R. (1997). Analysis of CANLEX liquefaction embankments: prototype and centrifuge models. Canadian Geotechnical Journal, 34(5), 641-657. DOI: 10.1139/t97-034.

Rong, W. and McCartney, J.S. (2019). Effect of suction on the drained seismic compression of unsaturated sand. In E3S Web of Conferences. EDP Sciences. Vol. 92, 08004. DOI: 10.1051/e3sconf/20199208004.

Rong, W. and McCartney, J.S. (2020a). Drained seismic compression of unsaturated sand. ASCE Journal of Geotechnical and Geoenvironmental Engineering. DOI: 10.1061/(ASCE)GT.1943-5606.0002251.

Rong, W. and McCartney, J.S. (2020b). Undrained seismic compression of unsaturated sand. ASCE Journal of Geotechnical and Geoenvironmental Engineering. DOI: 10.1061/(ASCE)GT.1943-5606.0002420.

Rong, W. and McCartney, J.S. (2020c). Seismic compression of unsaturated sand under undrained conditions. In Geo-Congress 2020: Geo-Systems, Sustainability, Geoenvironmental Engineering, and Unsaturated Soil Mechanics. ASCE, Reston, VA. 299-308. DOI: 10.1061/9780784482827.034.

Rong, W. and McCartney, J.S. (2021a). Methodology to characterize the seismic compression of unsaturated sands under different drainage conditions. ASTM Geotechnical Testing Journal. 44(2), 440-461. DOI: 10.1520/GTJ20190340.

Rong, W. and McCartney, J.S. (2021b). "Effect of relative density on the drained seismic compression of unsaturated backfills." 4th International Conference on Transportation Geotechnics. Chicago, IL. May 24-27. pp. 277-288. DOI: 10.1007/978-3-030-77238-3_21.

Seed, H.B. and Idriss, I.M. (1971). Simplified procedure for evaluating soil liquefaction potential. Journal of Soil Mechanics and Foundations Div. 97(9), 1249-1273. DOI: 10.1061/JSFEAQ.0001662.

Seed, H. B., and Silver, M. L. (1972). Settlement of dry sands during earthquakes. J. Geotech. Eng., 98(4), 381–397. DOI: 10.1061/JSFEAQ.0001745.

Seid-Karbasi M. and Byrne, P.M. (2006). Seismic liquefaction, lateral spreading and flow slides: a numerical investigation into void redistribution. Can. Geotech. J. 44, 873-890. DOI: 10.1139/t07-027.

Seid-Karbasi M. and Byrne, P.M. (2007). Effects of partial saturation on liquefiable ground response. GeoCongress 2007. ASCE, Reston, VA. 1-6.

Sheng, D., and Zhou, A.N. (2011). Coupling hydraulic with mechanical models for unsaturated soils. Can. Geotech. J. 48(5), 826-840. DOI: 10.1139/t10-109.

Silver, M.L. and Seed, H.B. (1971). Deformation characteristics of sands under cyclic loading. Journal of Soil Mechanics and Foundations Division, 97(8), 1081-1098. DOI: 10.1061/JSFEAQ.0001648.

Stewart, J.P., Chang, S.W., Bray, J.D., Seed, R.B., Sitar, N., and Riemer, M.F. (1995). A report on geotechnical aspects of the January 17, 1994 Northridge earthquake. Seismological Research Letters. 66(3), 7-19. DOI: 10.1785/gssrl.66.3.7.

Stewart, J.P., Bray, J.D., McMahon, D.J., Smith, P.M., and Kropp, A.L. (2001). Seismic performance of hillside fills. J. of Geotech. and Geoenv. Eng., 127(11), 905-919. DOI: 10.1061/(ASCE)1090-0241(2001)127:11(905).

Stewart, J.P., Smith, P.M., Whang, D.H., and Bray, J.D. (2004). Seismic compression of two compacted earth fills shaken by the 1994 Northridge earthquake. J. of Geotech. and Geoenv. Eng., 130(5), 461-476. DOI: 10.1061/(ASCE)1090-0241(2004)130:5(461).

Sawada, S., Tsukamoto, Y., and Ishihara, K. (2006). Residual deformation characteristics of partially saturated sandy soils subjected to seismic excitation. Soil Dynamics and Earthquake Engineering, 26(2-4), 175-182. DOI: 10.1016/j.soildyn.2004.11.024.

Tatsuoka, F. and Ishihara, K. (1974). Drained deformation of sand under cyclic stresses reversing direction. Soils and Foundations, 14(3), 51-65. DOI: 10.3208/sandf1972.14.3_51.

Tatsuoka, F., Iwasaki, T., Yoshida, S., Fukushima, S., and Sudo, H. (1979). Shear modulus and damping by drained tests on clean sand specimens reconstituted by various methods. Soils and Foundations, 19(1), 39-54. DOI: 10.3208/sandf1972.19.39.

Tokimatsu, K. and Seed, H.B. (1987). Evaluation of settlements in sands due to earthquake shaking. Journal of Geotechnical Engineering, 113(8), 861-878. DOI: 10.1061/(ASCE)0733-9410(1987)113:8(861).

Tsukamoto, Y., Ishihara, K., Nakazawa, H., Kamada, K., and Huang, Y. (2002). Resistance of partly saturated sand to liquefaction with reference to longitudinal and shear wave velocities. Soils and Foundations, 42(6), 93-104. DOI: 10.3208/sandf.42.6_93.

Unno, T., Kazama, M., Uzuoka, R., and Sento, N. (2008). Liquefaction of unsaturated sand considering the pore air pressure and volume compressibility of the soil particle skeleton. Soils and Foundations, 48(1), 87-99. DOI: 10.3208/sandf.48.87.

van Genuchten, M.T. (1980). A closed-form equation for predicting the hydraulic conductivity of unsaturated soils. Soil Science Society of America Journal, 44(5), 892-898. DOI. 10.2136/sssaj1980.03615995004400050002x.

Vucetic, M., Lanzo, G., and Doroudian, M. (1998). Damping at small strains in cyclic simple shear test. J. of Geotech. and Geoenv. Eng., 124(7), 585-594. DOI: 10.1061/(ASCE)1090-0241(1998)124:7(585).

Whang, D., Riemer, M.F., Bray, J.D., Stewart, J.P., and Smith, P.M. (2000). Characterization of seismic compression of some compacted fills. In Advances in Unsaturated Geotechnics. 180-194.

Whang, D.H., Stewart, J.P., and Bray, J.D. (2004). Effect of compaction conditions on the seismic compression of compacted fill soils. Geotechnical Testing Journal, 27(4), 1-9. DOI: 10.1520/GTJ11810.

Whang, D.H., Moyneur, M.S., Duku, P., and Stewart, J.P. (2005). Seismic compression behavior of non-plastic silty sands. In Advanced Experimental Unsaturated Soil Mechanics: Proceedings of the International Symposium on Advanced Experimental Unsaturated Soil Mechanics. Eds. A. Tarantino, E. Romero, Y.J. Cui. CRC Press, Boca Raton. 257-263.

Wheeler, S. J., Sharma, R. S., and Buisson, M. S. R. (2003). Coupling of hysteresis and stress–strain behavior in unsaturated soil. Géotechnique, 53(1), 41–54. DOI: 10.1680/geot.2003.53.1.41.

Wu, J., and Seed, R. B. (2004). Estimating of liquefaction-induced ground settlement (case studies). Proc., 5th Int. Conf. on Case Histories in Geotechnical Engineering, New York.

Youd, T.L. (1972). Compaction of sands by repeated shear straining. Journal of Soil Mechanics and Foundations Division, 98(SM7), 709-725. DOI: 10.1061/JSFEAQ.0001762.

Yee, E. and Stewart, J.P. (2011). Nonlinear Site Response and Seismic Compression at Vertical Array Strongly Shaken by 2007 Niigata-ken Chuetsu-oki Earthquake. Peer Report 2011/107.

Yee, E., Stewart, J.P., and Tokimatsu, K. (2011). Nonlinear site response and seismic compression at vertical array strongly shaken by 2007 Niigata-ken Chuetsu-oki Earthquake. Report PEER 2011/107. Pacific Earthquake Engineering Research Center. Berkeley, USA.

Yee, E., Duku, P.M., and Stewart, J.P. (2014). Cyclic volumetric strain behavior of sands with fines of low plasticity. Journal of Geotechnical and Geoenvironmental Engineering, 140(4), 04013042. DOI: 10.1061/(ASCE)GT.1943-5606.0001041.

Yoshimi, Y., Tanaka, K., and Tokimatsu, K. (1989). Liquefaction resistance of a partially saturated sand. Soils and Foundations, 29(3), 157-162. DOI: 10.3208/sandf1972.29.3_157.

Zheng, Y., Sander, A.C., Rong, W., Fox, P.J., Benson Shing, P., and McCartney, J.S. (2018). Shaking table test of a half-scale geosynthetic-reinforced soil bridge abutment. Geotechnical Testing Journal, 41(1), 171-192. DOI: 10.1520/GTJ20160268.

APPENDIX A

A.1 HYPERBOLIC FITTING FOR CYCLIC SHEARING

Using the small strain shear modulus and the ultimate shear stress, a hyperbolic model can be defined from initial loading data of the soil and is referred to as the backbone curve as shown in Figure A.1. The backbone curve shown in Figure A.1 was defined by fitting a hyperbola to the results from a monotonic set of shear stress versus shear strain data. Using hyperbolic fitting, the shear modulus is converted to a strain dependent parameter by linearizing the initial loading data of the stress strain curve. Specifically, by linearizing the relationship between $(\frac{\gamma}{\tau})$ and (γ), the slope and intercept can be interpreted as $(\frac{1}{\tau_{ult}})$, the inverse of the ultimate shear stress, and $(\frac{1}{Gi})$, the inverse of the initial shear modulus, respectively:

$$\tau = \frac{\gamma}{\frac{1}{G_i} + \frac{\gamma}{\tau_{ult}}} \tag{A.1.1}$$

$$\frac{\gamma}{\tau} = \frac{1}{G_i} + \frac{\gamma}{\tau_{ult}} \tag{A.1.2}$$

The empirically based mathematical model can be seen in Figure A.2. The ultimate shear stress is considered a dummy parameter because the value is never reached and is used in calculating the reduction factor to truncate the hyperbolic curve from linear elastic shearing to nonlinear plastic shearing. Using the ultimate shear stress from the best fit hyperbola and the shear stress at failure, (τ_f), the failure ratio (R_f) can be defined:

$$R_f = \frac{\tau_f}{\tau_{ult}} \tag{A.1.3}$$

The failure ratio aids in governing the overall shape of the shear stress strain curve. The ultimate shear stress will always be larger than the shear stress at failure and therefore (R_f) will be smaller than unity. An (R_f) value close to 1 signifies that the hyperbolic curve is very ductile, (R_f) values approaching 0 signify a very brittle curve. Since the actual data does not match a hyperbola perfectly, a certain stress level range is needed when fitting the slope and intercept. The stress level (SL) is defined as follows:

$$SL = \frac{\tau}{\tau_f} \tag{A.1.4}$$

If multiple data sets are available for the same soil sample at varying mean stresses, linearizing the data as shown in Figure A.3**,** the shear modulus number, (K_G^e) and exponent, (n_e), can be interpreted as the slope and intercept, respectively.

$$G_i = K_G^e P_a \left(\frac{\sigma'_m}{P_a}\right)^{ne} \tag{A.1.5}$$

$$\log\left[\frac{G_i}{P_a}\right] = \log(K_G^e) + n_e \log\left(\frac{\sigma'_m}{P_a}\right) \tag{A.1.6}$$

A.2 VOLUME COMPRESSION EQUATIONS

The equations used to predict the volumetric strain (seismic compression) are derived using a hyperbolic model similar to the Duncan-Chang model (Duncan et al. 1980) and are based on the UBCSAND model described by Puebla et al. (1997). The developed stress ratio is defined as the maximum shear stress divided by the mean stress. The developed stress ratio plotted against the plastic shear strains has a hyperbolic function with the plastic tangential shear modulus as the slope. Taking the derivative, the developed stress ratio is defined as follows:

$$\Delta\eta_d = \left[\frac{\Delta\tau}{\sigma'_m} - \left(\frac{\tau}{(\sigma'_m)^2}\right)\Delta\sigma'_m\right] \tag{A.2.1}$$

The increment of the mean stress is defined as the final mean stress minus initial mean stress:

$$\Delta\sigma'_m = \sigma'_m - \sigma'_{m0} \tag{A.2.2}$$

The increment of the shear stress is defined similarly as the final shear stress minus the initial mean stress:

$$\Delta\tau = \tau - \tau_0 \tag{A.2.3}$$

Using the energy considerations for plane strain conditions: $d\varepsilon_2^e = d\varepsilon_2^p = 0$, the dissipated energy can be defined as:

$$dE^D = \sigma'_1 d\varepsilon_1^p + \sigma'_3 d\varepsilon_3^p \tag{A.2.4}$$

The equation can be expressed as follows:

$$\sigma'_1 d\varepsilon_1^p + \sigma'_3 d\varepsilon_3^p = \frac{\sigma'_1 + \sigma'_3}{2}\left(d\varepsilon_1^p + d\varepsilon_3^p\right) + \frac{\sigma_1 - \sigma_3}{2}\left(d\varepsilon_1^p - d\varepsilon_3^p\right) \tag{A.2.5}$$

Now the equation for energy can be defined in terms of mean stress and shear stress:

$$dE^D = \sigma'_m d\varepsilon_v^p + \tau d\gamma^p \tag{A.2.6}$$

For constant volume assumptions, the energy dissipation can be defined as:

$$dE^D = \tau d\gamma^p = \sigma'_m \sin \emptyset_{cv}\, d\gamma^p \quad \text{(A.2.7)}$$

The Cam Clay model for plastic energy dissipation is defined as:

$$dE^P = \sigma'_m \sin \emptyset_{cv}\, d\gamma^p \quad \text{(A.2.8)}$$

Combining equations A2.6 and A2.8:

$$\sigma'_m d\varepsilon_v^p + \tau d\gamma^p = \sigma'_m \sin \emptyset_{cv}\, d\gamma^p \quad \text{(A.2.9)}$$

Now the plastic volumetric strain can be defined as:

$$d\varepsilon_v^p = \left(\sin \emptyset_{cv} - \frac{\tau}{\sigma'_m}\right) d\gamma^p \quad \text{(A.2.10a)}$$

In incremental form, the plastic volumetric strain increment can now be obtained:

$$\Delta\varepsilon_v^p = \left(\sin \emptyset_{cv} - \frac{\tau}{\sigma'_m}\right) \Delta\gamma^p \quad \text{(A.2.10b)}$$

The plastic shear strain increment is found using the derivative of the developed stress ratio and the tangential plastic shear modulus:

$$\Delta\gamma^p = \left(\frac{1}{G^p}\right)\left[\frac{\Delta\tau}{\sigma'_m} - \left(\frac{\tau}{(\sigma'_m)^2}\right)\Delta\sigma'_m\right] \quad \text{(A.2.11)}$$

Figure A.4 shows the hyperbolic relationship between the plastic shear strain, tangential plastic shear modulus and the developed stress ratio (where $\eta_d = \frac{\tau}{\sigma'_m}$).

A.3 PORE AIR PRESSURE DERIVATION

During undrained cyclic shearing, the phase relationship for a soil is expected to change as the particles rearrange and the air-filled pores are compressed, as shown schematically in Figure A.5. It should be noted that any theoretical derivations of changes in volume may be complex due to variability in the distribution and continuity of the different phases, as shown in the drawing in Figure A.6. Nonetheless, theoretical predictions can be useful to provide estimates of the changes in pore fluid pressures during shearing-induced volume changes. Specifically, using Boyle's Law and isothermal fluid elasticity, a relationship for the bulk modulus of air can be defined for seismic compression. It is assumed that all volumetric strain (seismic compression) occurs due to compression of the air voids. The initial and final volume of water and soils does not change during undrained cycling. The image in Figure A.6 shows the soil before and after cycling as it pertains to the air in the pores. Boyle's Law for the undrained compression of air is given by:

$$u_{ao}V_{ao} = u_{af}V_{af} \quad \text{(A.3.1)}$$

The change in volume of air can be defined as:

$$\Delta V_a = V_{ao} - V_{af} \tag{A.3.3}$$

which can be rearranged to find the V_{ao} and V_{af}:

$$V_{ao} = \Delta V_a + V_{af} \tag{A.3.4}$$

$$V_{af} = V_{ao} - \Delta V_a \tag{A.3.5}$$

Using these relationships, the volumetric strain of the air can be defined:

$$\varepsilon_a = \Delta V_a / V_{ao} = \frac{V_{ao} - V_{af}}{V_{ao}} \tag{A.3.6}$$

Rearranging Eq. (A.3.6) to simplify to strain in terms of V_{af}:

$$V_{af} = V_{ao} - \varepsilon_a V_{ao} = V_{ao}(1 - \varepsilon_a) \tag{A.3.7}$$

Substituting Eq. (A.3.6) into Boyle's Law in Eq. (A.3.1):

$$u_{ao} V_{ao} = u_{af} V_{ao}(1 - \varepsilon_a) \tag{A.3.8}$$

$$u_{ao} = u_{af}(1 - \varepsilon_a) = u_{af} - u_{af}\varepsilon_a \tag{A.3.9}$$

$$u_{af}\varepsilon_a = u_{af} - u_{ao} = \Delta u_a \tag{A.3.10}$$

$$u_{af} = \Delta u_a / \varepsilon_a \tag{A.3.11}$$

The isothermal pressurization for air can be represented can be represented by fluid elasticity:

$$\varepsilon_a = \Delta u_a / K_a \tag{A.3.12}$$

Combining Eq (A.3.11) and Eq (A.3.2), the bulk modulus of air can be defined as:

$$K_a = u_{af} \tag{A.3.13}$$

Assuming that the initial pore air pressure is at atmospheric pressure and under isothermal conditions:

$$\Delta u_a = u_{af} - u_{ao} = u_{af} - P_{atm} \tag{A.3.14}$$

$$u_{af} = \Delta u_a + P_{atm} \tag{A.3.15}$$

$$K_a = \Delta u_a + P_{atm} \tag{A.3.16}$$

This equation implies that when cycling initiates, the bulk modulus of air will evolve with the change in pore air pressure. To define the change in pore air pressure, a model needs to be defined in terms of the three-phase system (air, water, solids). To represent the properties of the three-phase system, it is advantageous to define each phase in terms of their individual volumes. The sums of the volumes of the 3-phase system need to be defined in terms of saturation and void ratio. The phase relationships can be used to define the equations:

$$V_T = V_{so} + V_{wo} + V_{ao} \tag{A.3.17}$$

$$V_{Vo} = V_{wo} + V_{ao} \tag{A.3.18}$$

$$V_T = V_{so} + V_{vo} \tag{A.3.19}$$

$$S_o = \frac{V_{wo}}{V_{Vo}} = \frac{V_{wo}}{V_{ao} + V_{wo}} \tag{A.3.20}$$

$$e_o = \frac{V_{vo}}{V_{so}} = \frac{V_{ao} + V_{wo}}{V_{so}} \tag{A.3.21}$$

If the volume of the solids is equal to one, which is the case when finding relationships between different phase variables, the following relationships can be defined:

$$V_{so} = V_{sf} = 1 \tag{A.3.22}$$

$$e_o = \frac{V_v}{V_s} = \frac{V_v}{1} \rightarrow e_o = V_{vo} \tag{A.3.23}$$

$$S_o = \frac{V_w}{V_V} = \frac{V_w}{e_o} \rightarrow S_o e_o = V_{wo} \tag{A.3.24}$$

If the previous relationships are true, then the three-phase system can be redefined as Figure A.7. Using these relationships, the volume of air can be redefined in terms of void ratio and saturation:

$$V_{ao} = V_T - V_{wo} - V_{so} \tag{A.3.25}$$

$$V_T = 1 + e_o \tag{A.3.26}$$

$$V_{ao} = 1 + e_o - S_o e_o - 1 = e_o - S_o e_o \tag{A.3.27}$$

$$V_{ao} = e_o(1 - S_o) \tag{A.3.28}$$

The three-phase system can now be defined as shown in Figures A.8 or A.9. Cyclic shearing will cause compression of the three-phase system over time. The compression of the water volume is considered very small in comparison to the compression of the air volume. The volume of air will be the largest contributor to compression of the three-phase system. Some air may dissolve into the capillary water due to Henry's law and the remainder of air (free air) may change in density as the air volume compresses. Assuming the Ideal Gas Law is valid for pore air, the free air in the system can be defined as:

$$u_{ao}V_{ao} = n_{ao(FA)}RT = \text{constant} \tag{A.3.29}$$

$$u_{af}V_{af} = n_{af(FA)}RT = \text{constant} \tag{A.3.30}$$

Eq. (A.3.29) and Eq. (A.3.30) can be set equal following Boyle's Law in Eq. (A.3.1). Since our system is in an undrained state, the amount of air particles is constant and can exist as free air in the voids or as dissolved air particles (Henry's Law) in the capillary water. The following equations are valid and true:

$$n_{ao(FA)} = \frac{u_{ao}V_{ao}}{RT} \tag{A.3.31}$$

$$n_{af(FA)} = \frac{u_{af}V_{af}}{RT} \tag{A.3.32}$$

$$n_{ao} = n_{af} \tag{A.3.33}$$

$$n_{ao} = n_{ao(FA)} + n_{ao(DA)} \tag{A.3.34}$$

$$n_{af} = n_{af(FA)} + n_{af(DA)} \tag{A.3.35}$$

Henry's law can be written as follows assuming that volume of water is constant ($V_{wo} = V_{wf} = V_w$) during cycling:

$$n_{ao(DA)} = hu_{ao}V_w \tag{A.3.36}$$

$$n_{af(DA)} = hu_{af}V_w \tag{A.3.37}$$

Inserting Eq. (A.3.37) into Eq. (A.3.35) yields:

$$n_{af} = n_{af(FA)} + hu_{af}V_w \tag{A.3.38}$$

Rearranging Eq. (A.3.38) and inserting into Eq. (A.3.32) yields:

$$n_{af} - hu_{af}V_w = \frac{u_{af}V_{af}}{RT} \tag{A.3.39}$$

Inserting Eq. (A.3.33) into Eq. (A.3.39):

$$n_{ao} - hu_{af}V_w = \frac{u_{af}V_{af}}{RT} \tag{A.3.40}$$

Inserting Eq. (A.3.34) into Eq. (A.3.40):

$$n_{ao(FA)} + n_{ao(DA)} - hu_{af}V_w = \frac{u_{af}V_{af}}{RT} \tag{A.3.41}$$

Inserting Eq. (A.3.31) and Eq. (A.3.36) into Eq. (A.3.41):

$$\frac{u_{ao}V_{ao}}{RT} + hu_{ao}V_w - hu_{af}V_w = \frac{u_{af}V_{af}}{RT} \tag{A.3.42}$$

Inserting Eq. (A.3.31), Eq. (A.3.13) and Eq. (A.3.5) into Eq. (42):

$$\frac{u_{ao}V_{ao}}{RT} + hu_{ao}V_w - h(\Delta u_a + P_{atm})V_w = \frac{(\Delta u_a + P_{atm})(V_{ao} - \Delta V_a)}{RT} \tag{A.3.43}$$

Inserting $P_{atm} = u_{ao}$:

$$\frac{P_{atm}V_{ao}}{RT} + hP_{atm}V_w - h(\Delta u_a + P_{atm})V_w = \frac{(\Delta u_a + P_{atm})(V_{ao} - \Delta V_a)}{RT} \tag{A.3.44}$$

Expanding the terms within the parentheses on the left-hand side:

$$\frac{P_{atm}V_{ao}}{RT} + hP_{atm}V_w - h\Delta u_a V_w - hP_{atm}V_w = \frac{(\Delta u_a + P_{atm})(V_{ao} - \Delta V_a)}{RT} \tag{A.3.45}$$

Reduce:

$$\frac{P_{atm}V_{ao}}{RT} - h\Delta u_a V_w = \frac{(\Delta u_a + P_{atm})(V_{ao} - \Delta V_a)}{RT} \tag{A.3.46}$$

Expanding the terms on the right-hand side:

$$\frac{P_{atm}V_{ao}}{RT} - h\Delta u_a V_w = \frac{(\Delta u_a V_{ao})}{RT} - \frac{(\Delta u_a \Delta V_a)}{RT} + \frac{(P_{atm}V_{ao})}{RT} - \frac{(P_{atm}\Delta V_a)}{RT} \quad \text{(A.3.47)}$$

Reduce:

$$-h\Delta u_a V_w = \frac{(\Delta u_a V_{ao})}{RT} - \frac{(\Delta u_a \Delta V_a)}{RT} - \frac{(P_{atm}\Delta V_a)}{RT} \quad \text{(A.3.48)}$$

Multiply both sides by RT and rearrange to put all Δu_a on one side:

$$(P_{atm}\Delta V_a) = h\Delta u_a V_w RT + (\Delta u_a V_{ao}) - (\Delta u_a \Delta V_a) \quad \text{(A.3.49)}$$

$$(P_{atm}\Delta V_a) = (hV_w RT + V_{ao} - \Delta V_a)\Delta u_a \quad \text{(A.3.50)}$$

The change in pore air pressure is equivalent to:

$$\frac{(P_{atm}\Delta V_a)}{(hV_w RT + V_{ao} - \Delta V_a)} = \Delta u_a \quad \text{(A.3.51)}$$

Using saturation and void ratio definitions from Eq. (A.3.24) and Eq. (A.3.23) to replace V_w and V_{ao} respectively:

$$\frac{(P_{atm}\Delta V_a)}{(hS_o e_o RT + e_o(1 - S_o) - \Delta V_a)} = \Delta u_a \quad \text{(A.3.52)}$$

The pore air pressure can be calculated from the cumulative volumetric strain derived as follows:

$$V_t = 1 + e_o \quad \text{(A.3.53)}$$

$$\frac{\Delta V_a}{V_t} = \Delta\varepsilon_v^p \quad \text{(A.3.54)}$$

$$\Delta V_a = \Delta\varepsilon_v^p (1 + e_o) \quad \text{(A.3.55)}$$

$$\varepsilon_v^p = \Delta\varepsilon_v^p + \varepsilon_{vo}^p \quad \text{(A.3.56)}$$

$$cumulative\ volumetric\ strain = \varepsilon_v^p (1 + e_o)$$

$$u_a = \frac{\left(P_{atm}\varepsilon_v^p (1 + e_o)\right)}{\left(hS_o e_o RT + e_o(1 - S_o) - \varepsilon_v^p (1 + e_o)\right)} \quad \text{(A.3.57)}$$

The solubility constant in Henry's equation is defined follows, where $h_a = 0.187 \frac{mol}{(L*bar)}$:

$$h = \frac{\rho_a}{\rho_w} h_a \tag{A.3.58}$$

Inserting the equation for pore pressure change into bulk modulus of air in Eq. (A.3.16):

$$K_a = \left[\frac{\left(P_{atm} \varepsilon_v^p (1 + e_o) \right)}{\left(h S_o e_o RT + e_o (1 - S_o) - \varepsilon_v^p (1 + e_o) \right)} + P_{atm} \right] \tag{A.3.59}$$

Rearranging Eq. (46) the relationship for the bulk modulus of the pore air is equal to:

$$K_a = \left[\frac{\varepsilon_v^p (1 + e_o)}{\left(h S_o e_o \times RT + e_o (1 - S_o) - \varepsilon_v^p (1 + e_o) \right)} + 1 \right] P_{atm} \tag{A.3.60}$$

A.4 RELATIONSHIP BETWEEN DEGREE OF SATURATION AND VOLUMETRIC STRAIN

Incremental change in saturation can be found using the initial conditions and assuming the change in pore air volume is responsible for the change in total volume of the specimen:

$$S = \frac{V_w}{V_v} \tag{A.4.1}$$

$$S = \frac{V_{wo}}{V_{af} + V_{wo}} \tag{A.4.2}$$

Using the equations defined in Appendix A.1, the following relationship exists for the initial volume of water:

$$V_{so} = V_{sf} = 1 \tag{A.4.3}$$

$$e_o = \frac{V_v}{V_s} = \frac{V_v}{1} \rightarrow e_o V_s = V_{vo} \tag{A.4.4}$$

$$S_o = \frac{V_{wo}}{V_V} = \frac{V_{wo}}{e_o V_s} \rightarrow S_o e_o V_s = V_{wo} \tag{A.4.5}$$

$$S = \frac{V_s e_o S_o}{V_{ao} - \Delta V_a + V_s e_o S_o} \quad \text{(A.4.6)}$$

$$S = \frac{V_s e_o S_o}{\left(V_s e_o (1 - S_o)\right) - \Delta V_a + V_s e_o S_o} \quad \text{(A.4.7)}$$

$$S = \frac{V_s e_o S_o}{e_o - \Delta V_a} \quad \text{(A.4.8)}$$

where $\Delta\varepsilon_v^p = \frac{\Delta V_a}{V_t}$ and $V_t = (V_s + e_o)$. Accordingly, degree of saturation can be calculated as follows:

$$S = \frac{V_s e_o S_o}{e_o - V_t \Delta\varepsilon_v^p} \quad \text{(A.4.9)}$$

$$S = \frac{V_s e_o S_o}{e_o - (V_s + e_o)\Delta\varepsilon_v^p} \quad \text{(A.4.10)}$$

$$S = \frac{V_s e_o S_o}{e_o - (V_s + e_o)\Delta\varepsilon_v^p} \quad \text{(A.4.11)}$$

For cumulative saturation change, the cumulative volumetric strain can be defined as follows:

$$\varepsilon_v^p = \Delta\varepsilon_v^p + \varepsilon_{vo}^p \quad \text{(A.4.12)}$$

The cumulative change in volume can be calculated as follows:

$$\Delta V_{cumulative} = \varepsilon_v^p (V_s + e_o) \quad \text{(A.4.13)}$$

A.5 TRANSIENT SCANNING CURVE EQUATION

To capture the poromechanical evolutions, the model uses empirical transient SWRC paths to calculate the changes in matric suction as the degree of saturation increases during rewetting. The data from Rong and McCartney (2020b) showed that the transient rewetting slopes increased with initial degree of saturation. The equation was derived using a simple linear path transformed for a semi-log plot. Using the rewetting path to create a linear equation to track the change in saturation with the change in matric suction would provide a way to model the pore water pressure generation. If initial cycling data is available, the slopes (m) can be interpreted and used to predict the trend of matric suction if the saturation changes are known:

$$S = -m \log_{10} \psi + b \tag{A.5.1}$$

$$S - b = -m \log_{10} \psi \tag{A.5.2}$$

$$10^{\frac{S-b}{-m}} = 10^{\log_{10} \psi} \tag{A.5.3}$$

$$10^{\frac{S-b}{-m}} = \psi \tag{A.5.4}$$

$$S_0 + m \log_{10} \psi_0 = b \tag{A.5.5}$$

$$\psi = 10^{\frac{S-(S_0+m \log_{10} \psi_0)}{-m}} \tag{A.5.6}$$

A.6 ADDITIONAL COMPARISONS BETWEEN EXPERIMENTAL RESULTS AND MODEL PREDICTIONS

Comparisons between experimental results from Rong and McCartney (2020a, 2020c) and the model predictions are presented in Figures A.10 to A.13. These results were used to determine the general trends shown in Chapter 6.

APPENDIX A: FIGURES

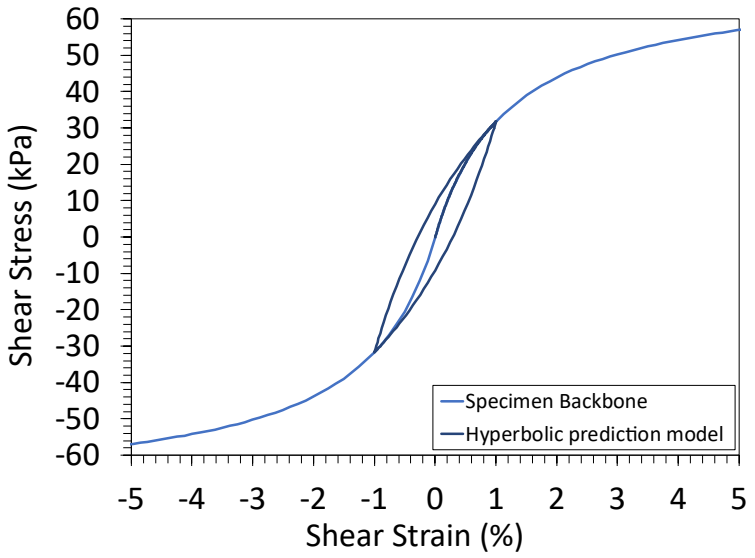

Figure A.1: Depiction of backbone curve with a hysteretic loop depicting shear strain range of 1% representing 1.25 cycles of shear strain.

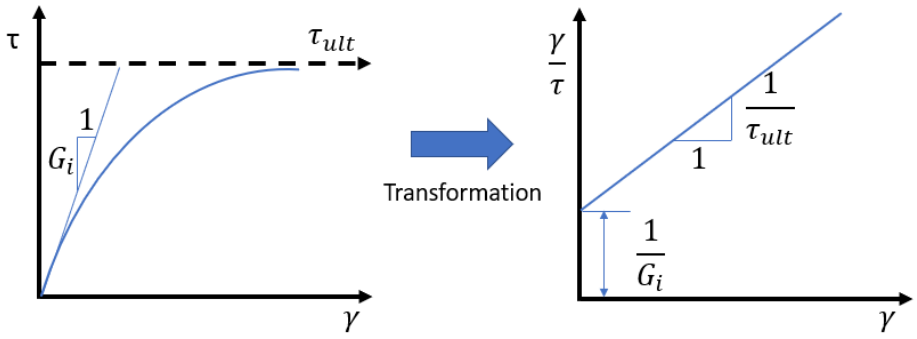

Figure A.2: Linear transformation of hyperbolic shear stress-strain relationship.

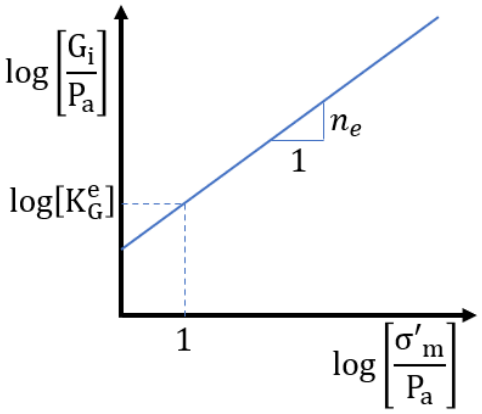

Figure A.3: Variation of initial shear modulus with changing mean stress.

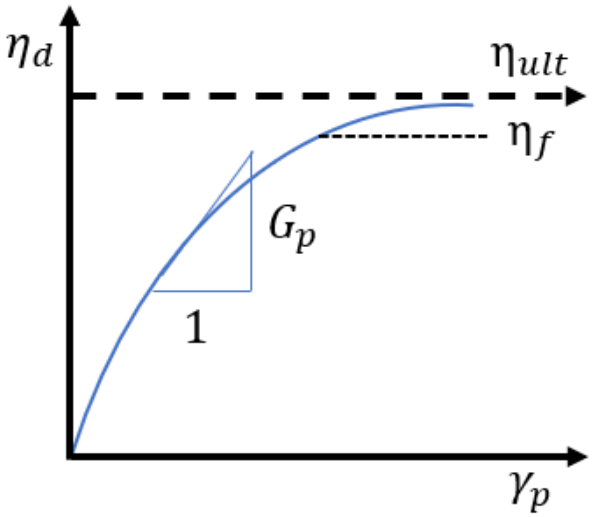

Figure A.4. Normalized shear stress-shear strain curve.

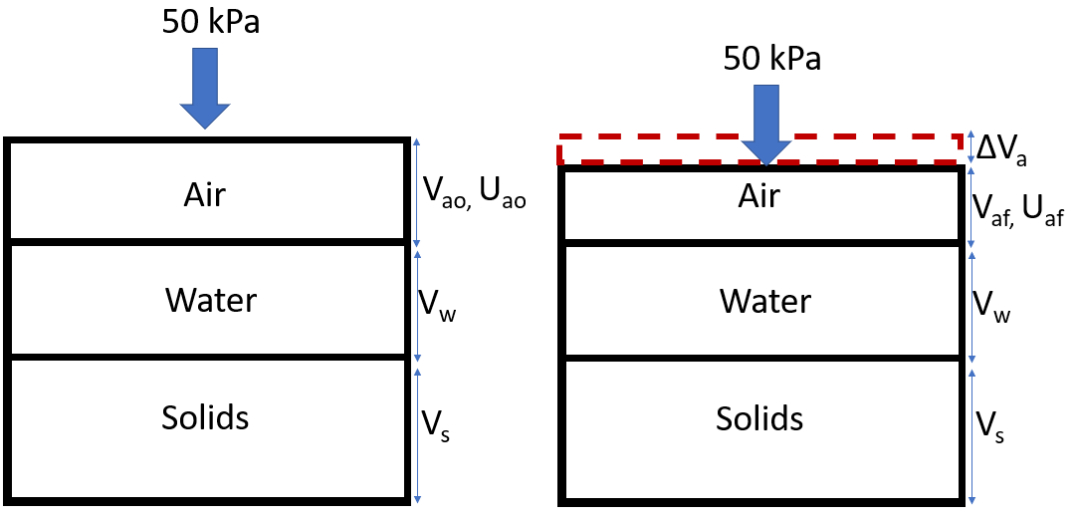

Figure A.5: (a) Before cycling air pressure and volume (b) After cycling air pressure and volume.

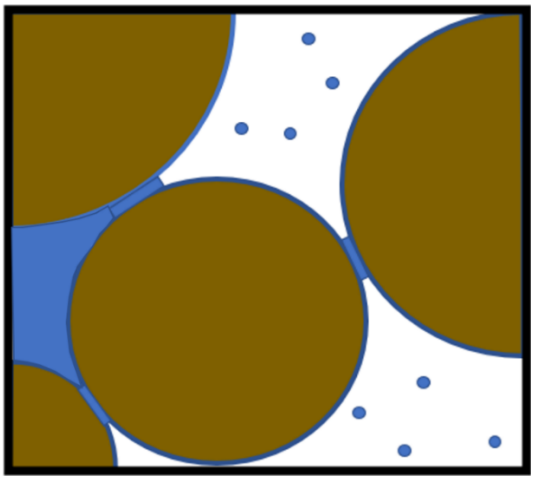

Figure A.6: Three phase system of air (white), water (blue), and solids (brown) in the funicular region of SWRC.

Figure A.7. Idealized image of volumes of a 3-phase system.

Figure A.8. Three-phase system new relationship.

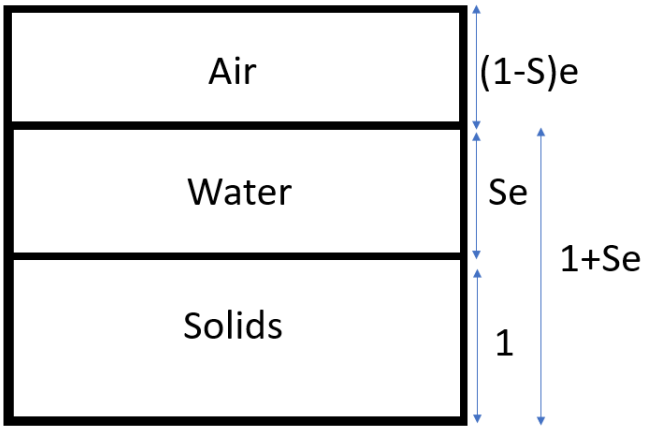

Figure A.9. Three-phase system defined in terms of saturation and void ratio.

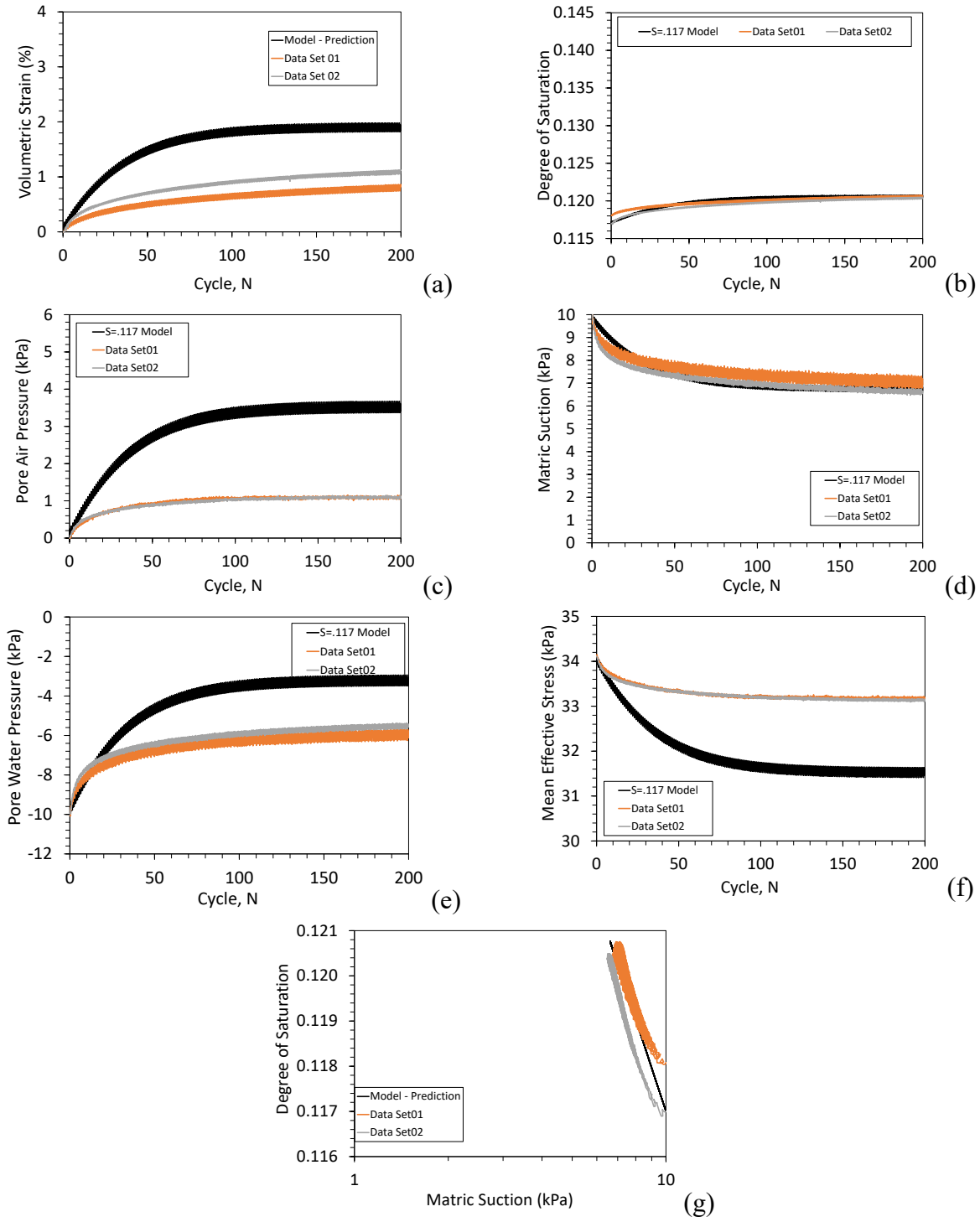

Figure A.10 Comparison between experimental results and model predictions for a sand specimen with S_o=0.117, ψ_o=10 kPa: (a) Volume change; (b) Degree of Saturation; (c) Pore air pressure; (d) Matric suction; (e) Pore water pressure; (f) Mean effective stress; (g) Degree of saturation vs. matric suction.

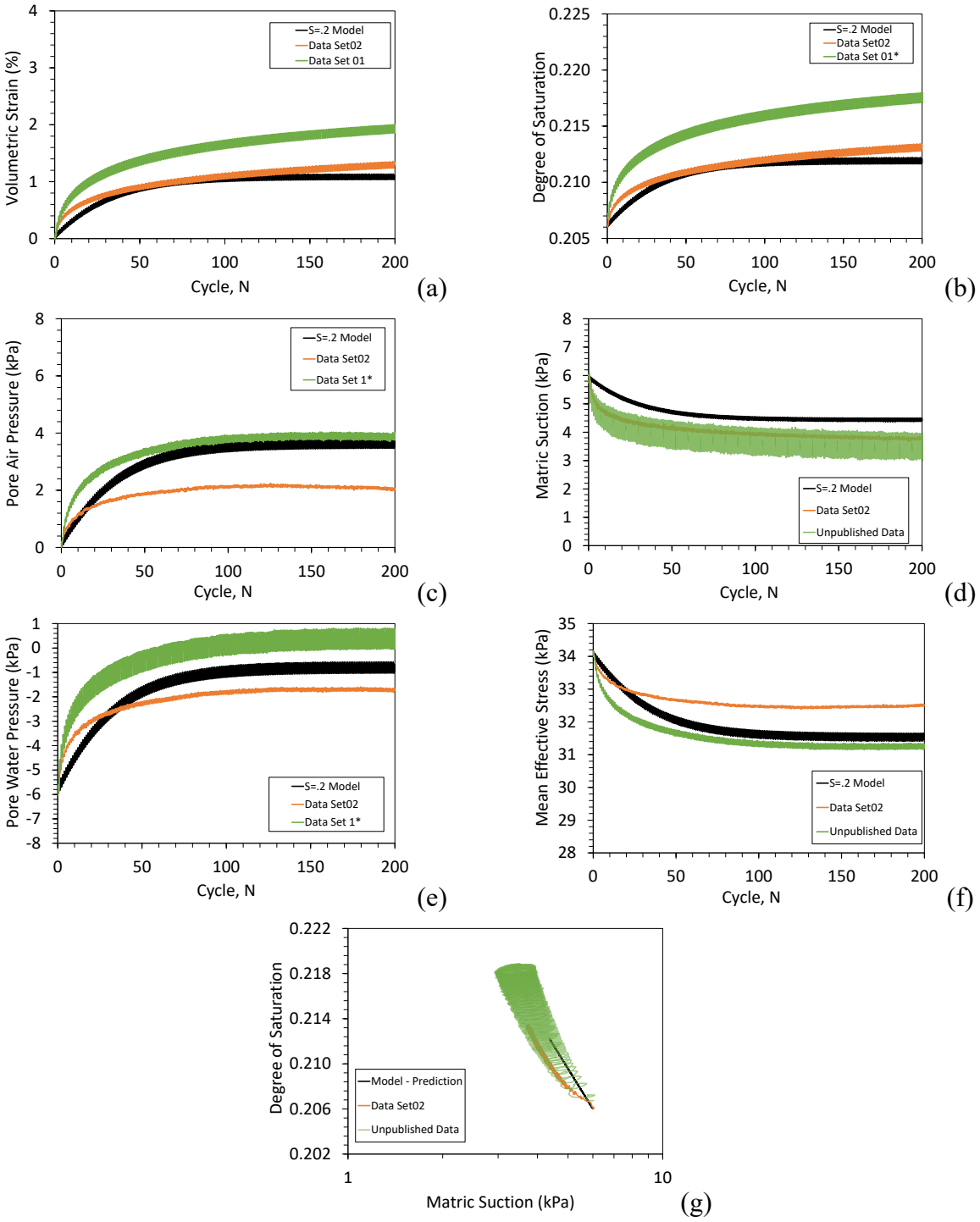

Figure A.11 Comparison between experimental results and model predictions for a sand specimen with S_o=0.2, ψ_o=6 kPa for SWRC fit to low cycles: (a) Volume change; (b) Degree of Saturation; (c) Pore air pressure; (d) Matric suction; (e) Pore water pressure; (f) Mean effective stress; (g) Degree of saturation vs. matric suction.

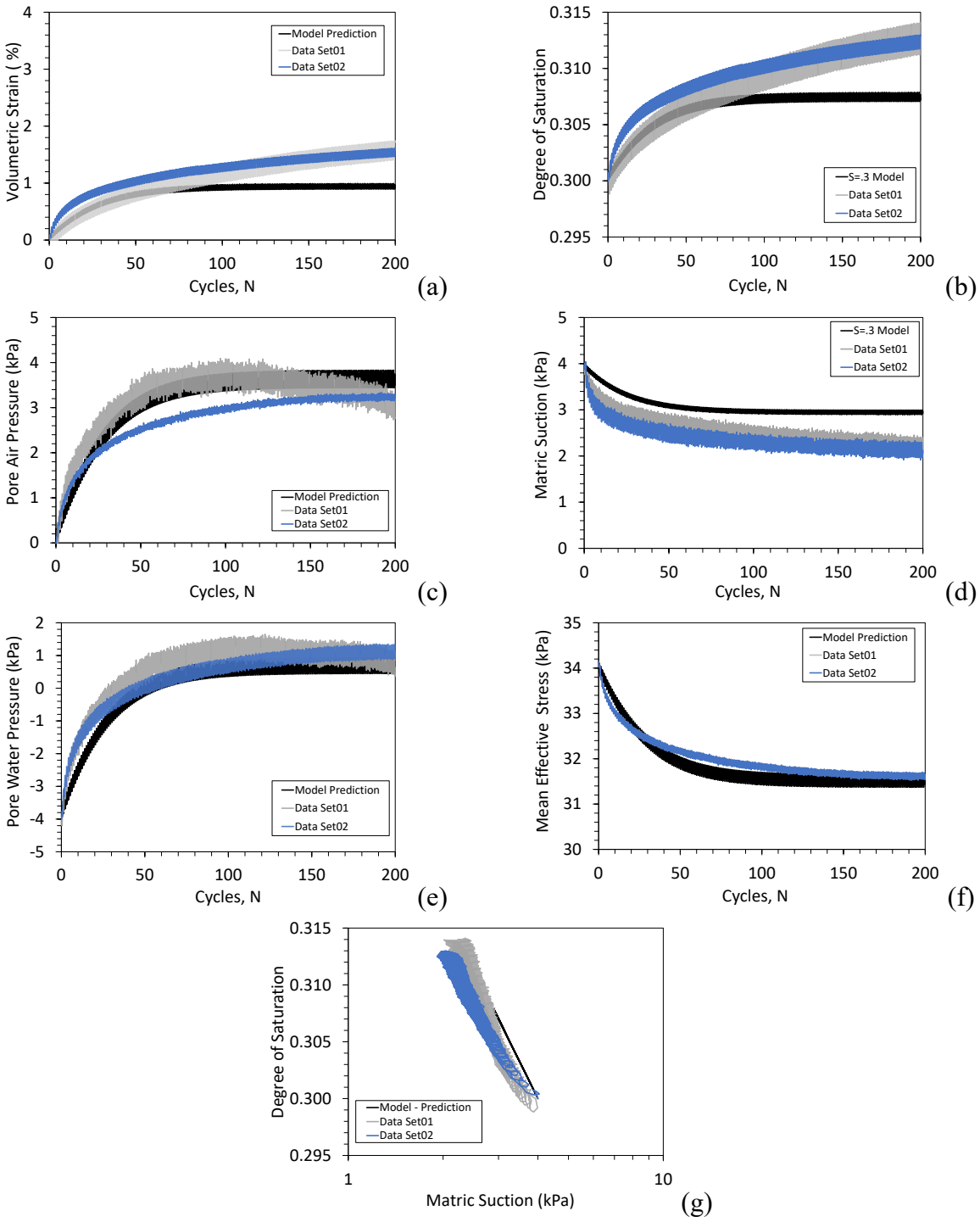

Figure A.12 Comparison between experimental results and model predictions for a sand specimen with S_o=0.3, ψ_o=4 kPa for SWRC fit to low cycles: (a) Volume change; (b) Degree of Saturation; (c) Pore air pressure; (d) Matric suction; (e) Pore water pressure; (f) Mean effective stress; (g) Degree of saturation vs. matric suction.

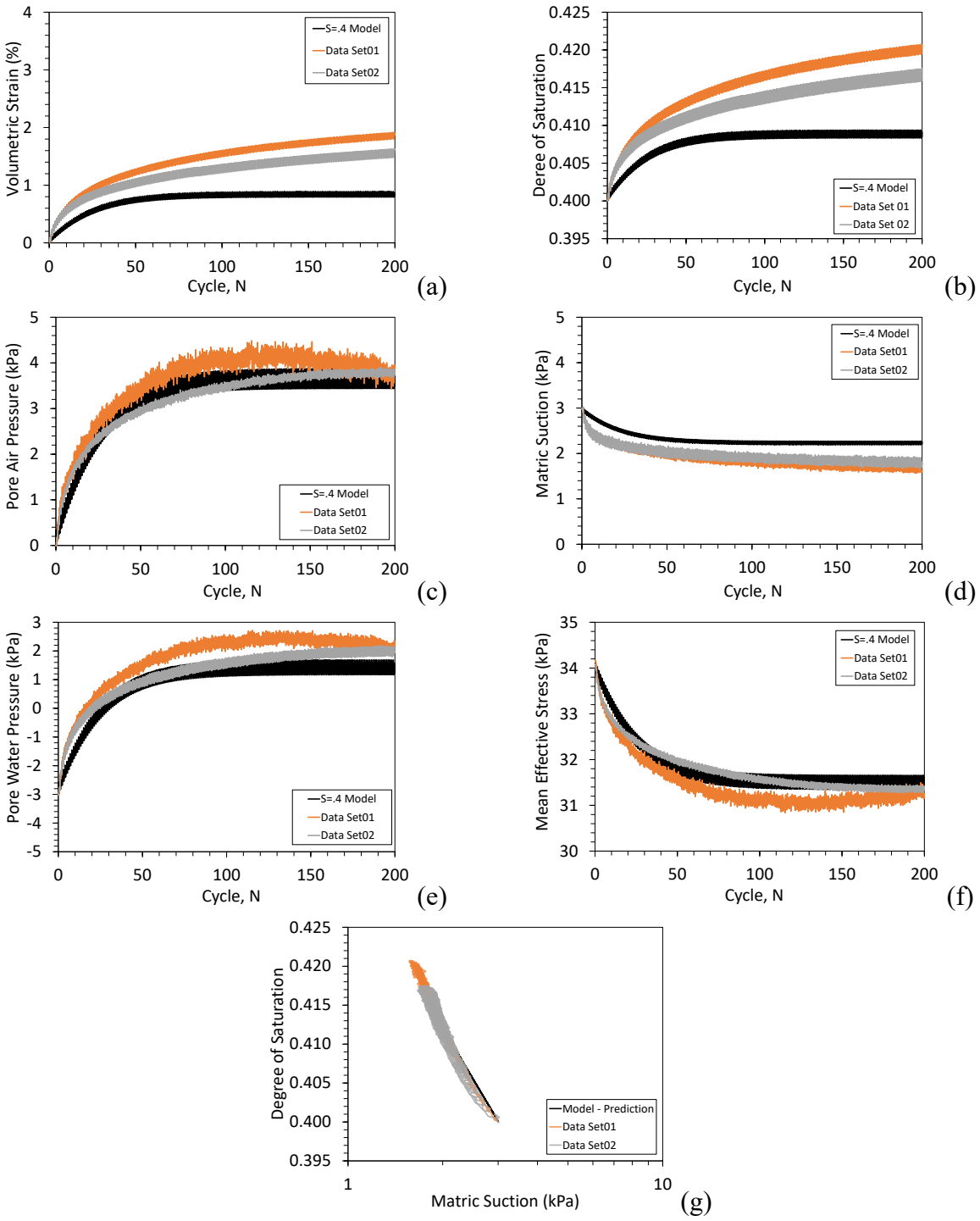

Figure A.13 Comparison between experimental results and model predictions for a sand specimen with S_o=0.4, ψ_o=3 kPa for SWRC fit to low cycles: (a) Volume change; (b) Degree of Saturation; (c) Pore air pressure; (d) Matric suction; (e) Pore water pressure; (f) Mean effective stress; (g) Degree of saturation vs. matric suction.

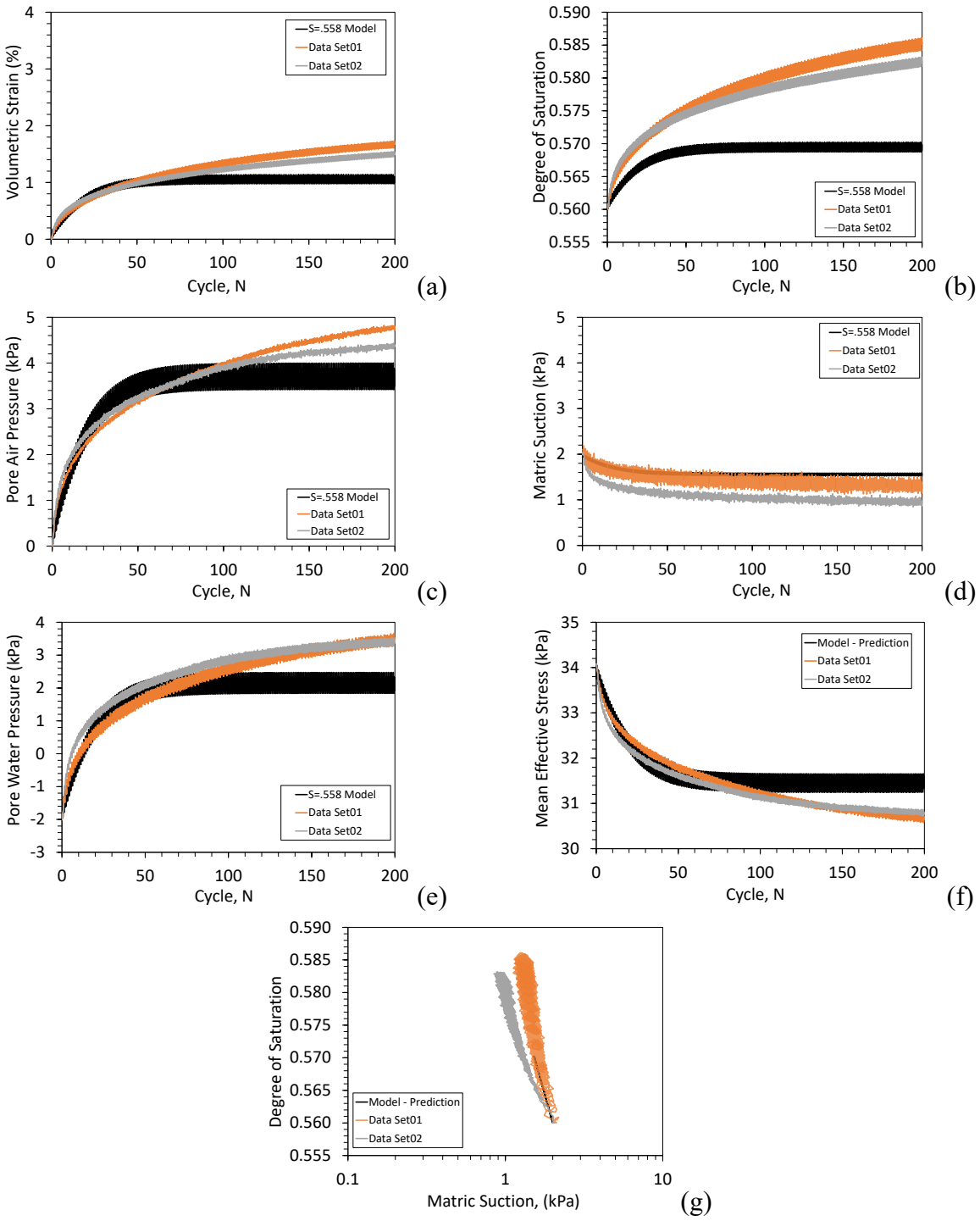

Figure A.14 Comparison between experimental results and model predictions for a sand specimen with S_o=0.56, ψ_o=2 kPa for SWRC fit to low cycles: (a) Volume change; (b) Degree of Saturation; (c) Pore air pressure; (d) Matric suction; (e) Pore water pressure; (f) Mean effective stress; (g) Degree of saturation vs. matric suction.

The Pacific Earthquake Engineering Research Center (PEER) is a multi-institutional research and education center with headquarters at the University of California, Berkeley. Investigators from over 20 universities, several consulting companies, and researchers at various state and federal government agencies contribute to research programs focused on performance-based earthquake engineering.

These research programs aim to identify and reduce the risks from major earthquakes to life safety and to the economy by including research in a wide variety of disciplines including structural and geotechnical engineering, geology/seismology, lifelines, transportation, architecture, economics, risk management, and public policy.

PEER is supported by federal, state, local, and regional agencies, together with industry partners.

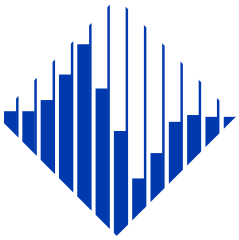

PEER Core Institutions

University of California, Berkeley (Lead Institution)
California Institute of Technology
Oregon State University
Stanford University
University of California, Davis
University of California, Irvine
University of California, Los Angeles
University of California, San Diego
University of Nevada, Reno
University of Southern California
University of Washington

Pacific Earthquake Engineering Research Center
University of California, Berkeley
325 Davis Hall, Mail Code 1792
Berkeley, CA 94720-1792
Tel: 510-642-3437
Email: peer_center@berkeley.edu

ISSN 2770-8314
https://doi.org/10.55461/YUNW7668